Improved SED-fitting Assumptions Result in Inside-out Quenching at $z \sim 0.5$ and Quenching at All Radii Simultaneously at $z \sim 1$

Alexander de la Vega[1,7] , Susan A. Kassin[1,2] , Camilla Pacifici[2] , Stéphane Charlot[3] , Emma Curtis-Lake[4] ,
Jacopo Chevallard[5] , Timothy M. Heckman[1] , Anton M. Koekemoer[2] , and Weichen Wang[1,6]

[1] Department of Physics & Astronomy, Johns Hopkins University, 3400 N. Charles Street, Baltimore, MD 21218, USA; alexandd@ucr.edu
[2] Space Telescope Science Institute, 3700 San Martin Drive, Baltimore, MD 21218, USA
[3] Sorbonne Université, CNRS, UMR7095, Institut d'Astrophysique de Paris, 98 bis bd Arago, 75014 Paris, France
[4] Centre for Astrophysics Research, Department of Physics, Astronomy and Mathematics, University of Hertfordshire, Hatfield AL10 9AB, UK
[5] Sub-department of Astrophysics, Department of Physics, University of Oxford, Denys Wilkinson Building, Keble Road, Oxford OX1 3RH, UK
[6] Department of Physics, University of Milan Bicocca, Piazza della Scienza 3, I-20126 Milan, Italy

Abstract

Many studies conclude that galaxies quench from the inside-out by examining profiles of specific star formation rate (sSFR). These are usually measured by fitting spectral energy distributions (SEDs) assuming a fixed dust law and uniform priors on all parameters. Here, we examine the effects of more physically motivated priors: a flexible dust law, an exponential prior on the dust attenuation A_V, and Gaussian priors that favor extended star formation histories. This results in model colors that better trace observations. We then perform radial SED fits to multiband flux profiles measured from Hubble Space Telescope images for 1440 galaxies at $0.4 < z < 1.5$ of stellar masses 10^{10}–$10^{11.5} M_\odot$ using both the traditional and the more physically motivated assumptions. The latter results in star formation rate and A_V profiles that agree with measurements from spectroscopy and A_V profiles that behave correctly as a function of inclination. Since green valley galaxies at $z \sim 1.3$ are expected to evolve into quiescent galaxies at $z \sim 0.9$, we compare their sSFR profiles using the more physically motivated assumptions. Their slopes are similar at all masses (0.06–0.08 dex kpc^{-1}), and the normalizations for the quiescent galaxies are lower. Therefore, the sSFR profiles decline with time as quenching occurs at all radii simultaneously. We compare profiles of green valley galaxies at $z \sim 0.9$ and quiescent galaxies at $z \sim 0.5$. The former are shallower at all masses by ~0.1 dex kpc^{-1}. The sSFR profiles steepen with time as galaxies quench from the inside-out. In summary, galaxies at $z \sim 1$ quench at all radii simultaneously while galaxies at $z \sim 0.7$ quench from the inside-out.

Unified Astronomy Thesaurus concepts: Galaxy evolution (594); Spectral energy distribution (2129); Galaxy quenching (2040)

1. Introduction

A major unsolved question in galaxy evolution concerns the end of star formation in galaxies (e.g., E. F. Bell et al. 2004; S. M. Faber et al. 2007; Y. J. Peng et al. 2010). While numerous mechanisms to terminate star formation, or "quench" have been proposed, conclusive evidence for the frequency with which galaxies quench under each mechanism has proven difficult to determine (see, e.g., A. Man & S. Belli 2018).

One way to learn about the quenching of galaxies is to study their spatially resolved spectra. Such data permit the study of the dust-corrected specific star formation rate (sSFR; SFR/stellar mass) as a function of radius and indicate which regions within galaxies were the first to quench. For nearby galaxies, studies that have examined these spectra generally find that galaxies have the lowest sSFRs in their centers and the highest sSFRs in their outskirts (e.g., F. Belfiore et al. 2018; S. L. Ellison et al. 2018; L. Lin et al. 2019). In other words, nearby galaxies quench from the inside-out.

An alternative approach to understanding quenching is to examine galaxies at low and high redshifts. Determining how galaxies evolve with time can be done by connecting galaxy populations at different redshifts. At $z \sim 1$, quiescent galaxies are rarer than at $z \sim 0$, but they begin to become more common with time (E. F. Bell et al. 2004; S. M. Faber et al. 2007; G. B. Brammer et al. 2011). At these intermediate redshifts, many studies have examined how galaxies quench. Most have done this by performing radial or spatially resolved spectral energy distribution (SED) fitting of galaxies using Hubble Space Telescope (HST) images (e.g., T. Morishita et al. 2015; E. J. Nelson et al. 2016, 2021; Abdurro'uf & M. Akiyama 2018; F. S. Liu et al. 2018; L. Morselli et al. 2019; S. Hemmati et al. 2020). Nearly all of these studies find that galaxies quenched from the inside-out at $z \sim 1$, in qualitative agreement with results for nearby galaxies, though these results are obtained in different ways. The rest of this Section will summarize studies that have examined galaxies at similar redshifts to this work. The studies below make similar SED-fitting assumptions, namely assuming uniform priors on all SED-fitting parameters and a single attenuation curve.

T. Morishita et al. (2015) examined the radial distribution of stellar mass and rest-frame colors of 3785 massive galaxies $(\log (M_\star/M_\odot) \gtrsim 10)$ at $0.5 < z < 3.0$ by performing SED fits to HST images from the Cosmic Assembly Near-infrared Deep Extragalactic Legacy Survey (CANDELS; N. A. Grogin et al. 2011; A. M. Koekemoer et al. 2011). This paper finds that

---

[7] Current address: Department of Physics & Astronomy, University of California, 900 University Avenue, Riverside, CA 92521, USA.

massive galaxies at these redshifts build up dense centers and sufficiently red rest-frame $U - V$ colors to quench from the inside-out at $z \sim 2$.

E. J. Nelson et al. (2016) used spatially resolved grism spectra from the 3D-HST survey (R. E. Skelton et al. 2014; I. G. Momcheva et al. 2016) to construct maps of the Hα emission line by stacking spectra of 3200 individual galaxies at $0.7 < z < 1.5$. This work constructs these maps as a function of stellar mass and location relative to the relation between stellar mass and SFR, known as the star formation main sequence (SFMS; K. G. Noeske et al. 2007; K. E. Whitaker et al. 2014; N. Lee et al. 2015; C. Schreiber et al. 2015; A. R. Tomczak et al. 2016). They obtain stellar mass surface density profiles by measuring surface brightness profiles in F140W and multiplying by spatially integrated mass-to-light ratios. For SFR surface density profiles, Hα surface brightness profiles are multiplied by the ratio of SFR to Hα luminosity (e.g., R. C. Kennicutt 1998). The Hα luminosities were not corrected for dust. This work finds that star formation is enhanced at all radii for galaxies above the SFMS and suppressed at all radii for galaxies below the SFMS. For high-mass galaxies $(10.5 < \log(M_\star/M_\odot) < 11)$, the largest difference in sSFR between galaxies on the SFMS and below it is found in the centers of galaxies, which, they write, suggests inside-out quenching (see also S. Tacchella et al. 2018).

E. J. Nelson et al. (2021) performed dust corrections to the grism data presented by E. J. Nelson et al. (2016) and compared their corrected sSFR profiles with those from the Illustris-TNG50 simulation (D. Nelson et al. 2018; A. Pillepich et al. 2018). Dust attenuation is measured via spatially resolved SED fitting of images from CANDELS. This paper finds that observed and simulated sSFR profiles are similar in both normalization and shape. It is found that galaxies at stellar masses $\log M_\star > 10.5$ have centrally suppressed sSFR profiles, indicative of inside-out quenching, which is attributed to feedback from central supermassive black holes. At lower stellar masses, it is found that galaxies on, above, and below the SFMS have approximately flat sSFR profiles.

Abdurro'uf & M. Akiyama (2018), F. S. Liu et al. (2018), L. Morselli et al. (2019), and S. Hemmati et al. (2020) all performed spatially resolved or radial SED fitting on CANDELS images for galaxies at intermediate redshifts $(0.2 < z < 1.8)$ and concluded that galaxies quench from the inside-out at high mass $(\log(M_\star/M_\odot) > 10.5)$ and potentially from the outside-in at lower mass $(\log(M_\star/M_\odot) < 10.5)$. Abdurro'uf & M. Akiyama (2018) examined sSFR profiles for 152 galaxies at $0.8 < z < 1.8$ and stellar masses $\log(M_\star/M_\odot) > 10.5$ by constructing maps of stellar mass and SFR surface densities. F. S. Liu et al. (2018) inferred sSFR profiles for 4377 galaxies at stellar masses $9 < \log(M_\star/M_\odot) < 11$ and at redshifts $0.5 < z < 1.0$ using radial profiles of the rest-frame UVI colors. L. Morselli et al. (2019) constructed maps of stellar mass and surface densities for 712 galaxies at $0.2 < z < 1.2$ and stellar masses $\log M_\star \geqslant 9.5$. They measured sSFR profiles using these maps and found that galaxies below the SFMS show the greatest suppression in sSFR in their centers at all masses considered. Lastly, S. Hemmati et al. (2020) also measured maps of stellar mass and SFR surface densities for 545 galaxies at $0.8 < z < 1.0$. For each galaxy in their sample, they fit Schechter functions to the distributions of SFR surface density and stellar mass surface density. They found that the knees of these Schechter functions lie at larger radii for

galaxies that lie farther below the SFMS, which, they write, suggests that galaxies quench from the inside-out.

Many studies have shown that results from SED fits are sensitive to modeling assumptions, and particular attention has been paid to the treatment of dust attenuation and star formation histories (SFHs; e.g., C. Pacifici et al. 2012, 2015; J. Pforr et al. 2012; B. Salmon et al. 2016; K. Iyer & E. Gawiser 2017; B. Lo Faro et al. 2017; A. C. Carnall et al. 2018; J. Leja et al. 2019; S. Lower et al. 2020; B. Wang et al. 2023). Recent work has built upon earlier studies that make conventional SED-fitting assumptions. For example, C. Pacifici et al. (2015) demonstrated that using a single dust law and uniform priors results in stellar masses that are systematically overestimated by ~0.1 dex and SFRs that are underestimated by ~0.6 dex, when compared to a more sophisticated approach wherein a flexible attenuation curve and nonparametric SFHs are adopted (SFHs in this work are derived from a post-treatment of cosmological simulations). J. Leja et al. (2019) showed that using a flexible attenuation curve and nonparametric SFHs yields stellar masses that are ~0.1–0.3 dex higher and SFRs that are ~0.1–1.0 dex lower than those obtained by SED fits that assume a single attenuation curve and parametric SFHs (their nonparametric SFHs assign weights to specified bins in lookback time).

In this paper, we examine the effects of varying SED-fitting assumptions on the radial properties of a large sample of massive galaxies at intermediate redshift $(0.4 < z < 1.5)$. The paper is laid out as follows. In Section 2, we describe the HST imaging and other data sets used in this paper. In Section 3, we select our sample. We measure radial flux profiles and their uncertainties in Section 4 and describe how SED fitting is performed in Section 5. We construct five sets of assumptions to understand which changes to which priors affect the profiles. These are introduced in Section 6, where model colors are compared against observed colors. We find that changes to the dust law and star formation histories have the most significant effects. In Section 7, we describe how we define star-forming, green valley, and quiescent galaxies. We then create radial profiles of the stellar mass surface density, SFR surface density, sSFR, A_V, and mass-weighted age in Section 8. In the same Section, we also examine how these profiles change as a result of changing the SED-fitting assumptions. This is done by examining how the models behave in color–color space with respect to observations. In Section 9, we compare our radial profiles with those measured from spectroscopy and determine that the fifth set of assumptions is most appropriate for our sample. We also compare our profiles with expected behavior as a function of inclination. In Section 10, we examine sSFR profiles under the fifth set of assumptions and provide a physical interpretation of these profiles in Section 11. We summarize and conclude in Section 12.

All magnitudes in this paper are in the AB system (J. B. Oke & J. E. Gunn 1983), and we adopt the cosmological parameters measured by Planck Collaboration et al. (2016).

2. Data and Data Products

2.1. Hubble Images and Photometry

Publicly available multiband imaging and integrated photometry from the CANDELS (N. A. Grogin et al. 2011; A. M. Koekemoer et al. 2011) in the Great Observatories Origins Deep Survey (M. Giavalisco et al. 2004) North and

South fields, hereafter GOODS-N and GOODS-S, are used. The images were taken with the HST Advanced Camera for Surveys (ACS) in the F435W, F606W, F775W, and F850LP bandpasses, and the Wide Field Camera 3 (WFC3) in the F125W, F140W, and F160W bandpasses. Images in the F140W bandpass were taken as part of the 3D-HST survey (R. E. Skelton et al. 2014).

Mosaicked images of each bandpass are from A. M. Koekemoer et al. (2011). All are aligned to the same reference frame and drizzled to a common pixel scale of $0\overset{''}{.}06$ pixel^{-1}. We refer to these as images in the rest of the paper. The point-spread function (PSF) of each mosaic is then degraded to the resolution of the F160W bandpass using PSF-matching kernels from R. E. Skelton et al. (2014). The PSF of the F160W mosaic has an FWHM of $0\overset{''}{.}18$.

Integrated photometry is adopted for all bandpasses from Y. Guo et al. (2013) for GOODS-S and G. Barro et al. (2019) for GOODS-N. These measurements use HST images that are PSF-matched to the resolution of the F160W image. Sources are selected in the F160W bandpass.

We use Galactic reddening maps measured by D. J. Schlegel et al. (1998), later recalibrated by E. F. Schlafly & D. P. Finkbeiner (2011), to correct for Galactic extinction for all filters. The $E(B-V)$ values measured in GOODS-N and GOODS-S are converted to A_{V} assuming $R_{\mathrm{V}} = 3.1$. Then, the extinction curve from E. L. Fitzpatrick (1999) is used to derive an extinction for each filter. These corrections are small and are as follows: 0.0419, 0.0276, 0.0183, 0.0138, 0.0081, 0.0070, and 0.0063 magnitude in GOODS-N and 0.0288, 0.0190, 0.0125, 0.0094, 0.0055, 0.0049, and 0.0043 magnitude in GOODS-S in the F435W, F606W, F775W, F850LP, F125W, F140W, and F160W filters, respectively.

2.2. Axis Ratios and Position Angles

From these images, axis ratios of galaxies, defined as the ratio of the minor to major axes, and position angles of the major axes were measured by Y. Guo et al. (2013) and G. Barro et al. (2019) for GOODS-S and GOODS-N, respectively. We adopt these measurements for our analysis. These parameters are measured by applying the Source Extractor software (E. Bertin & S. Arnouts 1996) to the F160W images. Y. Guo et al. (2013) and G. Barro et al. (2019) used the same SExtractor parameters to detect sources in each field. Typical fractional errors in the axis ratio are 2%, and typical errors in the position angle are $<5°$.

2.3. Redshifts

Redshifts are adopted from a collection of spectroscopic and photometric redshifts compiled by D. Kodra et al. (2023). To measure photometric redshifts, they used five different codes, each of which uses different techniques to estimate the probability distribution function (PDF) of a galaxy's redshift. Each photometric redshift we adopt for this paper is the probability-weighted expectation value of the combined redshift PDF from the five codes for a given galaxy. Cuts on the photometric redshift uncertainties are discussed in detail in Section 3.

2.4. X-Ray Data

Active galactic nuclei (AGNs) are identified and removed using Chandra X-ray catalogs in GOODS-N (Y. Q. Xue et al. 2016) and GOODS-S (B. Luo et al. 2017). These surveys have

exposure times of ~2 Ms and ~7 Ms, and reach flux limits of 3.5×10^{-17} erg cm^{-2} s^{-1} and 1.9×10^{-17} erg cm^{-2} s^{-1} in the full band (0.5–7 keV) in GOODS-N and GOODS-S, respectively.

3. Sample Selection

3.1. The Full Sample

We begin with all sources in the integrated flux catalogs for GOODS-N and GOODS-S. These sources are then cross-matched with catalogs of spectroscopic and photometric redshifts. A maximum separation of $0\overset{''}{.}2$ was used in the cross-matching. All sources are matched. There are a total of 70,375 sources: 35,445 in GOODS-N and 34,930 in GOODS-S. Of these, 64,117 have photometric redshifts and 6258 have spectroscopic redshifts.

We remove galaxies contaminated by bright foreground stars and the foreground stars themselves. We require the SExtractor stellarity index CLASS_STAR to be <0.78 (S. Boada et al. 2015). To remove galaxies that fall on diffraction spikes or are on the edges of the images, we require the flag PhotFlag to be zero. These cuts remove 3348 sources, leaving 67,027.

Galaxies are selected to span redshifts $0.4 < z < 1.5$, so that the HST bandpasses span the rest-frame ultraviolet to near-infrared (NIR). This wavelength range is optimal for measuring stellar masses and star formation rates (C. Pacifici et al. 2012; J. Pforr et al. 2012; V. Buat et al. 2014). At $z = 0.4$, the rest-frame wavelength range is $\lambda \sim 3100$–11,000 Å, and at $z = 1.5$ it is $\lambda \sim 1750$–6200 Å. This redshift cut removes 40,134 galaxies and leaves 26,893.

For our analysis, galaxies are selected to have an F160W magnitude brighter than 25 to ensure high signal-to-noise ratios (S/Ns) in the photometry. This cut removes low-mass galaxies (often $<10^9 M_{\odot}$) and decreases the sample by 15,119, with 11,774 galaxies left.

We require galaxies to be in the following images: F435W, F606W, F775W, F850LP, and F125W. We do not require galaxies to be in the F140W mosaic, because it is not necessary for our analysis: it has significant wavelength overlap with F125W and F160W, and it is the shallowest of all of the images. This restriction reduces the sample by 1034, leaving 10,740 galaxies. Of these 10,740 galaxies, 8889 are observed in F140W.

To remove X-ray AGNs, we then remove all galaxies detected in the X-ray catalogs (Section 2.4). This removes 185 galaxies and leaves 10,555.

We remove galaxies that are not resolved in the F160W bandpass, i.e., those with half-light radii smaller than the FWHM of the PSF, which is $0\overset{''}{.}18$ (A. M. Koekemoer et al. 2011; S. Wuyts et al. 2012). The galaxies that are excluded are mostly low-mass blue galaxies at low redshift (i.e., stellar mass $<10^9 M_{\odot}$, redshift $z < 1$, and rest-frame $U - V < 1.0$ mag). The cut is achieved by selecting galaxies with half-light radii in F160W (column name FLUX_RADIUS_2_F160W in the catalogs) to be >3 pixels. This removes 225 galaxies and leaves 10,330.

Galaxies are further selected to have spectroscopic redshifts or photometric redshifts with small uncertainties. Of the 10,330 galaxies that remain, 3804 have spectroscopic redshifts (543 are measured using the HST grism) and 6526 have photometric redshifts. Here we discuss the photometric redshifts. D. Kodra et al. (2023) measured Bayesian photometric redshift posterior
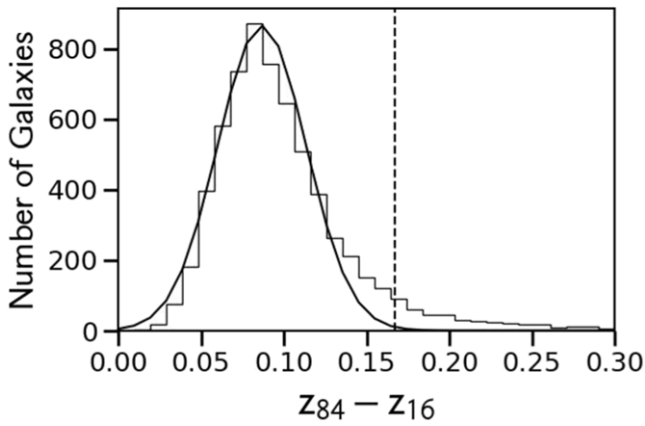
Figure 1. Only photometric redshifts with reasonable uncertainties are used in this work. The distribution of the widths of the posteriors of the photometric redshifts of D. Kodra et al. (2023) are shown. The width of the posterior is the difference between the 84th percentile of the posterior, z_{84}, and the 16th percentile, z_{16}. The solid line is a Gaussian fit to the histogram, and the dashed line is three standard deviations above the mean. Galaxies with photometric redshift posterior widths beyond the dashed line at $z_{84} - z_{16} = 0.168$ are considered outliers and are excluded.

distributions following T. Dahlen et al. (2013). Figure 1 shows the distribution of the photometric redshift posterior widths, defined as the difference between the 16th and 84th percentiles of each photometric redshift posterior. The distribution peaks at a width of ∼0.08 and has a long tail toward higher widths. We fit a Gaussian to the bulk of the distribution, where the widths are <0.15. The fit is shown as the solid line in Figure 1 and has a mean of $\mu = 0.087$ and standard deviation of $\sigma = 0.027$. We exclude galaxies with widths $>3\sigma$ above the mean, 0.168, indicated by the dashed line in Figure 1. This cut removes 634 galaxies and leaves 9696. Galaxies that are removed by this cut have similar distributions in stellar mass and SFR (which come from the physical parameter catalogs by P. Santini et al. 2015) compared to the galaxies that are retained. Therefore, removing them does not bias our sample.

The remaining 9696 galaxies are referred to in this paper as the "full sample." Their distributions in redshift and color–color space are shown in the top row of Figure 2.

3.2. The Mass-selected Sample: $log(M_\star/M_\odot) \geqslant 10$

This work relies on measurements of radial profiles of galaxies. To ensure a high S/N in the radial profiles, we select galaxies with stellar masses greater than $log(M_\star/M_\odot) \geqslant 10$. The stellar masses are measured using SED-fitting (see Section 5).

In this paper, we examine five sets of SED-fitting assumptions. We select galaxies with stellar masses greater than or equal to $10^{10}M_\odot$ under any set of assumptions. These galaxies encompass the "mass-selected sample." Of the 9696 galaxies in the full sample, 1909 are in the mass-selected sample. Its distributions in redshift and color–color space are shown in the bottom row of Figure 2. The mass-selected sample makes up the reddest galaxies in the full sample. This is because galaxies are more likely to be older, dustier, more metal-rich, and quiescent at higher mass (e.g., A. Gallazzi et al. 2005; T. Garn & P. N. Best 2010; C. Y. Peng et al. 2010).

3.2.1. Visual Inspection to Remove Contaminated and Merging Galaxies

Lead author A.dlV. visually inspected the galaxies in the mass-selected sample to remove major mergers, galaxies contaminated by neighbors, and galaxies whose images are affected by artifacts and diffraction spikes from bright stars. A total of 32 major mergers and 426 galaxies that are too close to neighbors are removed. The 32 major mergers and 426 contaminated galaxies are evenly spread out in stellar mass and redshift; removing them does not affect our results. Artifacts affect 11 galaxies, which are removed. A total of 1440 galaxies remain.

Only galaxies that are obviously undergoing mergers (those that display features such as, e.g., multiple nuclei, off-center nuclei, or disturbed morphologies in close proximity to projected neighbors) or are close enough to neighboring galaxies such that their light profiles become difficult to distinguish, are removed. This is done because of the following. Merging and contaminated galaxies contain multiple generations of stellar populations whose SFHs are likely complex and cannot be modeled under the SED-fitting assumptions used in this work (Section 6). Consequently, inferences from fitting their SEDs are unreliable.

4. Construction of Flux Profiles

4.1. Measuring Radial Flux Profiles

Radial flux profiles are created for the 1440 galaxies in the mass-selected sample (Section 3.2) in each of the HST bandpasses. In Figure 3, these radial flux profiles are shown for four example galaxies. Flux profiles are created in elliptical annuli starting in the center of each galaxy using the `photutils` (L. Bradley et al. 2020) task `EllipticalAnnulus`, the shapes of which do not change with radius. For the four example galaxies in Figure 3, they are shown as white ellipses. The galaxy centers and ellipse shapes are adopted from Y. Guo et al. (2013) and G. Barro et al. (2019), for GOODS-S and GOODS-N, respectively, for the F160W images. We choose to use annuli widths of 2 pixels because it is greater than the PSF half-width at half maximum (1.5 pixels) and small enough to provide high spatial resolution. Over the redshift range studied, 2 pixels span 0.65–1.03 kpc. The radius of each annulus is defined to be the middle of each annulus. The flux profile of each galaxy is measured out to a radius where the S/N in an annulus is ≥3 in two bandpasses. We restrict the profiles to even higher S/Ns in the reddest bandpass, as we explain below. This restriction is indicated by red circles and red vertical lines in Figure 3.

Given the radial flux profiles that reach an S/N of 3, we apply an additional restriction on the S/N of the reddest rest-frame bandpass. We chose to do this in the reddest bands to ensure the mass-to-light ratio is constrained at all radii, as it is most easily measured using the reddest bands (E. F. Bell & R. S. de Jong 2001; E. N. Taylor et al. 2011; J. Ge et al. 2021). Specifically, we require an S/N of at least 5 in an annulus in F125W for $z \leqslant 0.8$ and F160W for $z > 0.8$. These wave bands correspond to the rest-frame R and I wave bands. Examples of these cuts are shown as red ellipses and red vertical lines in the bottom row of each panel in Figure 3.

For galaxies whose light profiles are contaminated by neighbors, we visually inspect the surface brightness profiles in F125W and F160W for galaxies at $z \leqslant 0.8$ and $z > 0.8$,
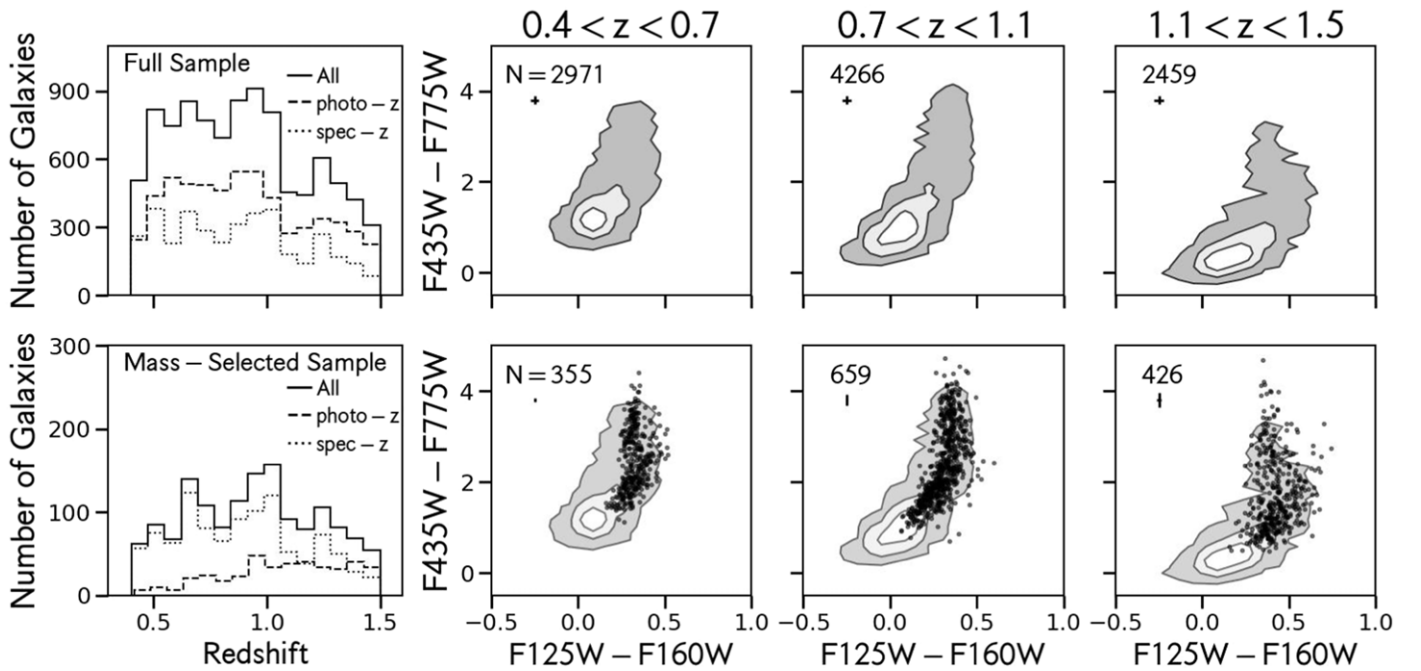
Figure 2. The distributions of redshifts and integrated optical-to-near-infrared (NIR) colors are shown for the full sample in the top row, and for the mass-selected sample in the bottom row. The mass-selected sample consists of the reddest galaxies in the full sample, as expected. Higher-mass galaxies are observed to be older, dustier, more metal-rich, and more likely to be quiescent than lower-mass ones. Radial profiles are measured for galaxies in the mass-selected sample. Distributions of all, photometric, and spectroscopic redshifts are shown as solid, dashed, and dotted lines, respectively. In the color–color plots for three redshift bins that we will use throughout the paper, contours represent the distributions of the full sample. White, light-gray, and dark-gray contours enclose 50%, 16%, and 2%, respectively, of the maximum number density of the color–color distribution. Colors of the mass-selected sample are shown as black dots. The number of galaxies in each redshift bin and median uncertainty in each color are indicated in each panel.

respectively. The presence of the neighbor is indicated by a "bump" in the profiles, and the flux profile is cut at the first local minimum we find before the bump.

4.2. Uncertainties on the Flux Profiles

We account for three sources of uncertainty in the radial flux profiles: the uncertainty due to background subtraction, the uncertainty from the inverse variance weight images, and the Poisson noise from galaxies. The uncertainties on the flux profiles are dominated by those due to background subtraction (30%–90% of the uncertainty in each annulus) at most radii beyond the centers of galaxies, especially in the outer parts. Below we describe how these are calculated as they play an important role in determining how far out in radius we can accurately measure galaxy flux profiles. Another contribution to the uncertainty is from the HST inverse variance weight images (30%–60% of the uncertainty). These take into account noise from flat-fielding, dark current, and readout, as well as the sky background Poisson noise (S. Casertano et al. 2000; A. M. Koekemoer et al. 2011). Finally, although dominant (20%–60% of the uncertainty) only in the centers of galaxies and nearly negligible ($\lesssim$10%) at larger radii, Poisson noise from the galaxies is taken into account.

Each of these sources of uncertainty is added in quadrature to yield the total uncertainty in flux for a given aperture. In Figure 3, the shading around each radial flux profile indicates the total flux uncertainty. In general, the uncertainty in any bandpass is small wherever the galaxy is bright. In the centers, where the S/N is the highest, the Poisson noise is $\lesssim$0.01 mag arcsec^{-2}, and other sources of uncertainty are of similar size or smaller. At radii where the galaxy is faint, the uncertainty grows. The uncertainty is largest at the farthest

distances from the centers of galaxies because the surface brightness there is the lowest. At these distances, the errors due to sky subtraction and those quantified in the weight images dominate. In these regions, errors due to sky subtraction are often ~0.2–0.3 mag arcsec^{-2}, and those quantified in the weight images are ~0.1–0.2 mag arcsec^{-2}.

To obtain the uncertainty from the weight image, first the weight image is inverted to get a variance image. Then, for a given annulus, the square of each pixel value is summed for all pixels in the annulus. The error from the weight image is taken as the square root of this sum.

The Poisson noise is measured as follows. The science image is first multiplied by the exposure time image to get a Poisson variance image. Then, the square root of this image is divided by the exposure time image. For a given annulus, the square of each pixel value is summed. The Poisson noise is taken as the square root of this sum.

A final uncertainty is added to all fluxes (for each bandpass and radial bin) to account for zero-point errors and mismatches between the template SEDs and observed SEDs. This additional uncertainty is set to be 5% of the flux (see, e.g., Table 4 of T. Dahlen et al. 2013 and Table 11 of R. E. Skelton et al. 2014).

4.2.1. Uncertainties due to Background Subtraction

Uncertainties due to background subtraction are measured using the empty aperture technique (I. Labbé et al. 2003; S. Wuyts et al. 2008; K. E. Whitaker 2011; R. E. Skelton et al. 2014). In this technique, the normalized median absolute deviation (NMAD) of the background is measured for a range of aperture sizes. In practice, apertures are randomly placed in empty regions of the images such that they do not overlap each
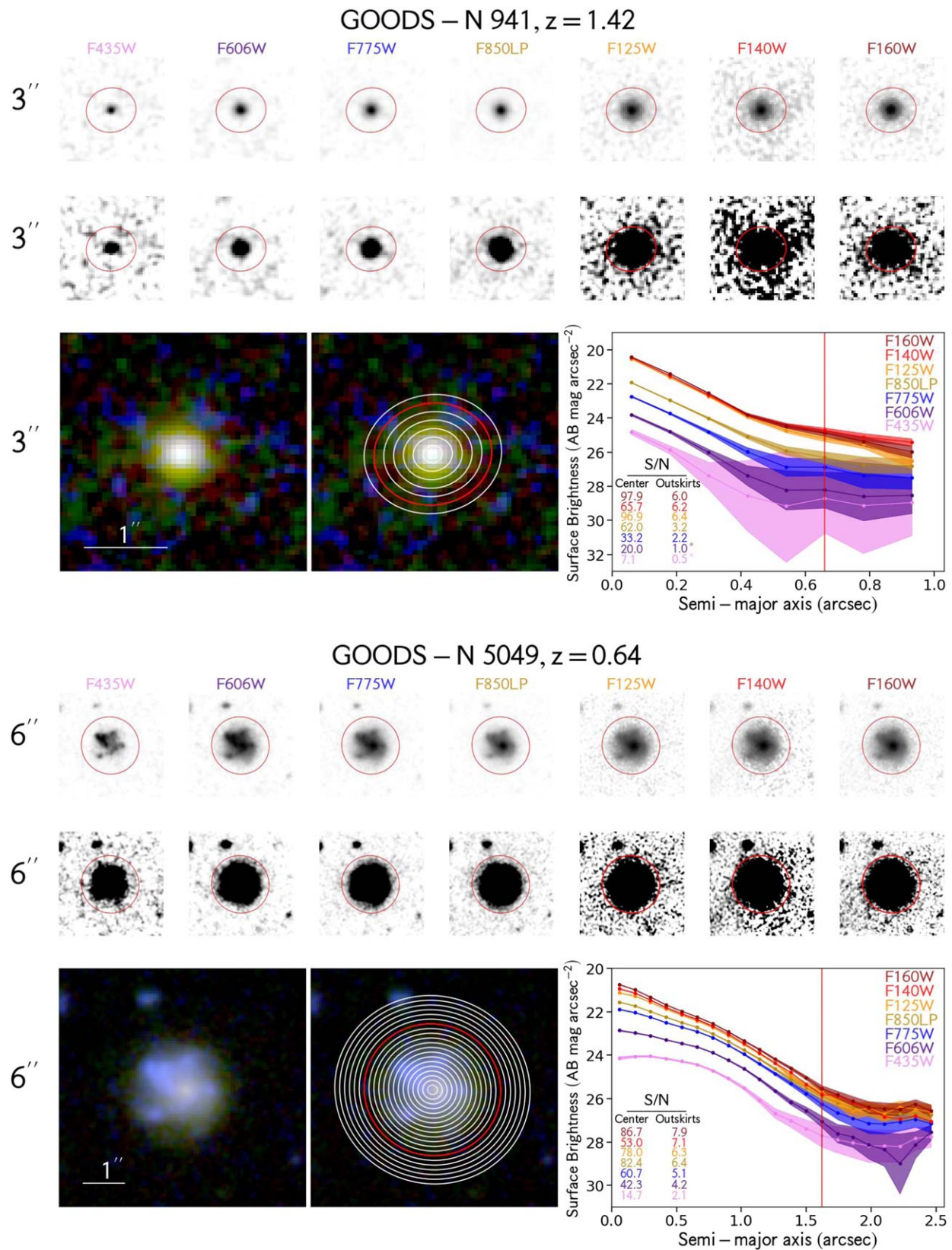
Figure 3. HST postage stamps, RGB images, and radial flux profiles of four example galaxies in our sample. The top and middle rows show postage stamps for all seven HST bandpasses in a low- and high-contrast stretch, respectively. The bottom row shows RGB images with and without annuli used to create the profiles drawn on top in white, and the resulting surface brightness profiles of the galaxies in all seven HST bandpasses. For GOODS-S 17058, we plot every other annulus for clarity. The RGB image is made from the F435W, F850LP, and F160W bandpasses. The red annuli in all images, and the red vertical lines in the surface brightness profile plots indicate the cuts in radius based on the S/N in F125W or F160W, depending on the redshift (Section 4.1). For each galaxy, in the lower-left corner of the surface brightness profile plots, we list the S/N in the center and at the cut in radius above in all bandpasses. These share the same colors as the profiles. S/N values with asterisks indicate fluxes that are treated as upper limits in the SED fits (see Section 5.2).

GOODS − N 5752, z = 1.14

GOODS − S 17058, z = 0.62
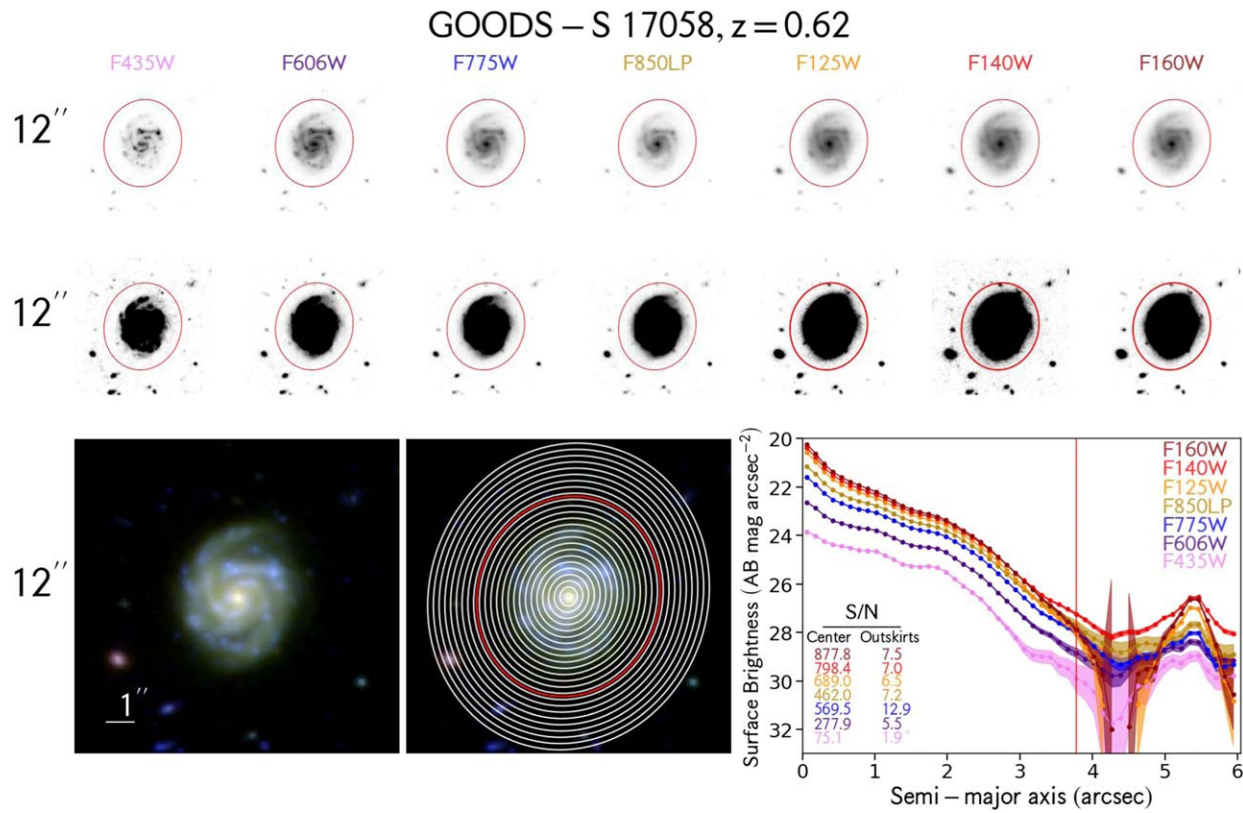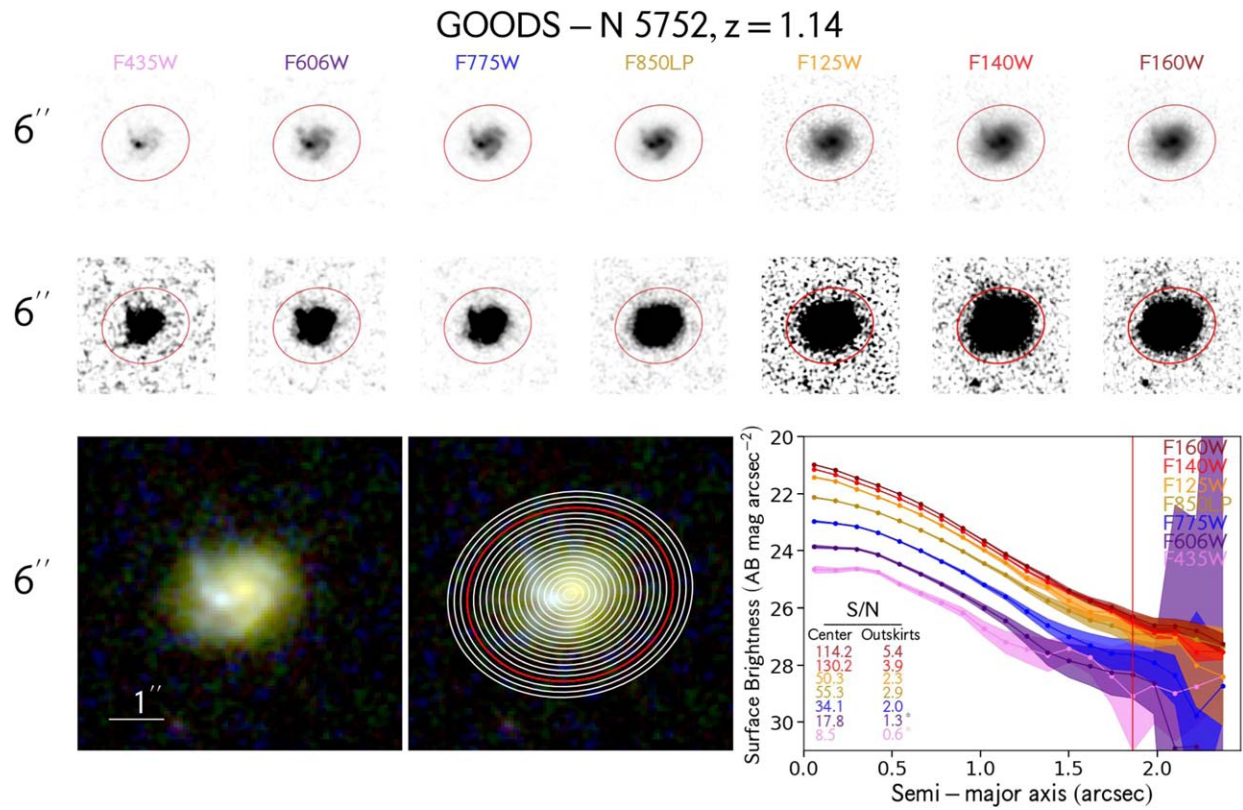
Figure 3. (Continued.)

other, any galaxies, or the edges of the images. A power law is then fit to the relation between NMAD and aperture size. In Figure 4, the NMAD of the background is shown as a function

of aperture diameter in all bandpasses as dots. Power-law fits to the NMAD as a function of aperture diameter are shown as lines. Full details are as follows.

Table 1
Power-law Parameters for Uncertainties due to Background Subtraction for Each Parameter and Bandpass Combination

Parameter	F435W	F606W	F775W	F850LP	F125W	F140W	F160W
α	0.31	0.33	0.36	0.40	0.56	0.27	0.65
	0.42	0.36	0.39	0.35	0.48	0.52	0.50
β	1.51	1.42	1.45	1.45	1.23	1.22	1.20
	1.34	1.48	1.35	1.52	1.36	1.17	1.34

The first line gives the value for GOODS-N, and the second line gives the value for GOODS-S.
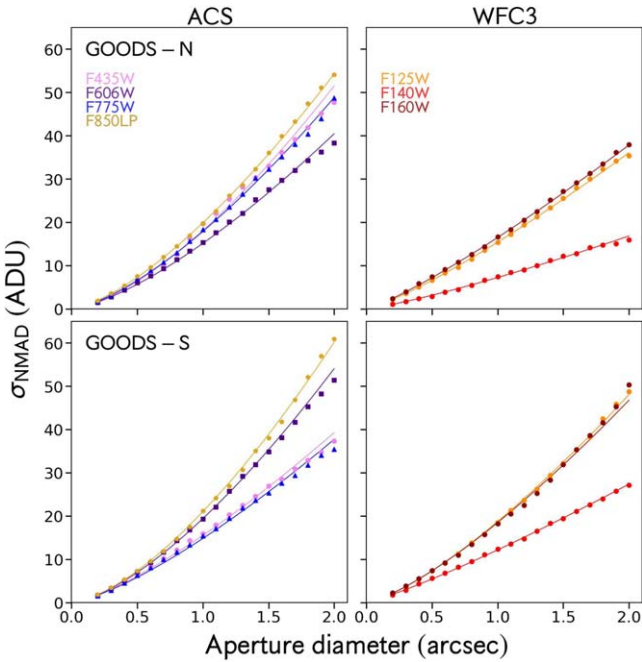
Figure 4. The uncertainty due to background subtraction is calculated by first performing aperture photometry on noise-equalized images in empty regions and in circular apertures of various radii. Then, the normalized median absolute deviation (σ_{NMAD}) of the flux distribution for apertures of a given radius is measured, and a power law is fit to σ_{NMAD} as a function of aperture area in pixels. Lastly, σ_{NMAD} is divided by the average of the square root of the weight map within an aperture. For an aperture of radius equal to $0\rlap{.}''25$, the uncertainty due to background subtraction in F160W is ~1 nJy in the Hubble Ultra Deep Field and ~10 nJy in the Wide portion of GOODS-S. Here, we show σ_{NMAD} as a function of the aperture diameter in the four ACS bands (left) and the three WFC3 bands (right) for GOODS-N in the top row and GOODS-S in the bottom row. The σ_{NMAD} measured in the F435W, F606W, F775W, and F850LP bandpasses is plotted as dots, squares, triangles, and pentagons, respectively. The power-law fits to each set of σ_{NMAD} values in each bandpass are shown as thin lines. Colors indicate the bandpass and are the same as in Figure 3. The uncertainty due to background subtraction rises quickly with increasing aperture size and is steeper for the ACS bands than for the WFC3 bands, corresponding to differences such as PSF, detector pixel scale, readnoise, and background level, which combine to produce somewhat different scalings in each case. This uncertainty is taken into account in the radial profiles.

First, the science image is multiplied by the square root of the weight image to produce a noise-equalized image. Noise equalization is crucial, as the HST images in certain bandpasses vary widely in depth. Next, 2000 circular apertures of radius $1''$ are randomly placed on the noise-equalized image. The apertures are placed such that no aperture overlaps with another aperture, a segmentation map of a galaxy as identified by SExtractor (from Y. Guo et al. 2013 and G. Barro et al. 2019), or with the edge of the image. Aperture photometry is performed in the noise-equalized image, and the NMAD of the

resulting flux distribution is computed. This process is repeated for various aperture sizes, ranging in radius from $0\rlap{.}''1$ to $1\rlap{.}''0$, as shown by the points in Figure 4 and is performed for all HST bands using the same apertures.

To calculate the error due to background subtraction for any aperture size, we fit a power law of the form $\sigma_{\mathrm{NMAD}} = \alpha(\sqrt{A})^{\beta}$, indicated by the lines in Figure 4, where σ_{NMAD} indicates the NMAD values measured in various aperture sizes, and A is the area of the aperture in pixels. The fit parameters for the GOODS-N and GOODS-S fields are listed separately in Table 1. The uncertainty due to background subtraction in an aperture is computed by calculating σ_{NMAD} using the power-law fits to σ_{NMAD} as a function of aperture area and dividing by the average value of the square root of the weight mosaic within the aperture. This last step ensures the uncertainty has the same units as the science mosaic. For a galaxy of brightness ~10 μJy in F160W with outskirts that have a surface brightness of ~26 mag arcsec^{-2}, the uncertainty due to background subtraction in an annulus of area ~1 square arcsec is ~0.1 mag arcsec^{-2}.

Less than half a percent of galaxies in the mass-selected sample (six out of 1440) possess apertures with areas larger than the largest aperture used to measure the uncertainty due to sky subtraction. For these galaxies, σ_{NMAD} is extrapolated from the power-law fits. The largest annulus has an area that is 39% larger and an error that is 29% larger than the largest aperture used to measure the error due to background subtraction.

5. SED Modeling

In this Section, we fit the SED at each radius in the flux profiles with the BEAGLE SED-fitting tool to obtain profiles of star formation rate, stellar mass, age, and dust (J. Chevallard & S. Charlot 2016, version 0.20.2). Additionally, we fit the integrated fluxes of the galaxies to obtain integrated stellar masses and star formation rates.

5.1. The BEAGLE SED-fitting Tool and Treatment of Its Output

BEAGLE has multiple options for star formation and chemical enrichment histories and dust attenuation. We assume delayed-τ star formation histories and that metallicity is the same for all stars at a given radius. We use the empirical starburst attenuation curve measured by D. Calzetti et al. (1994) and the attenuation curve relations derived by J. Chevallard et al. (2013). BEAGLE can fit SEDs using stellar and nebular emission templates simultaneously, and we use this option. For stellar emission, it uses the updated version of the G. Bruzual & S. Charlot (2003) stellar population synthesis (SPS) models described by J. Gutkin et al. (2016; see also S. Charlot et al. 2017). For nebular emission, it adopts the photoionization models developed by J. Gutkin et al. (2016), which combined the updated G. Bruzual & S. Charlot (2003)

models with models of photoionized interstellar gas from CLOUDY (G. J. Ferland et al. 2013). BEAGLE adopts a Bayesian framework. It uses the MULTINEST tool (F. Feroz et al. 2009) to efficiently explore parameter space and accurately quantify uncertainties on fit parameters.

For each physical property of interest (e.g., stellar mass, SFR, A_V, and mass-weighted age), BEAGLE returns a posterior distribution. We use the median of the posterior as the most representative value of the physical property. The majority of the sample shows little to no difference between the median and the maximum a posteriori, the peak value of the posterior PDFs, suggesting that the distributions are not heavily skewed or multimodal. We use SFRs averaged over the last 100 Myr in this work. Stellar mass and SFR surface densities are measured by taking the median stellar mass and SFR from their respective posteriors and dividing by the area of the annulus that these properties were measured in. We measure sSFRs by dividing the SFR surface density by the stellar mass surface density. With this process, we obtain radial profiles of physical properties (hereafter "science profiles") for the physical parameters.

5.2. Upper Limits on Flux Profiles

When fitting the SED at each galaxy radius, if the flux in a given bandpass has $S/N \leqslant 2$, it is customary to remove it from the SED fit. However, we choose to treat it as an upper limit. In practice, this is done by replacing the flux value with a number that is close to zero and its uncertainty with the value of the flux. This was done in a similar manner by T. Shanks et al. (2021). The flux is replaced with an arbitrarily low value, 10^{-20} Jy, which is well below the sensitivity limits of the images. When these replacements are made, in the SED fits, the model fluxes are forced to be lower than the observed ones. This functions as an upper limit.

5.3. Priors in SED Fitting

One of the main aspects of this paper is an examination of five different sets of priors in our BEAGLE SED fits, which we detail in the following Section. Priors, or existing knowledge about the expected distributions of parameters being fit for (e.g., stellar mass, star formation rate) should be appropriate for the data being fit. For example, star-forming galaxies generally contain dust, so priors on the amount of dust should allow for high attenuation values. Whether priors are appropriate for the galaxies being fit can be tested by comparing the colors of models with those of the galaxies, as we do in Figure 5. The models should trace the data—the empty contours in Figure 5 should trace filled contours. If the models are too narrow for the data, as in the leftmost panels in the figure, the SED fits will lead to artificially narrow posterior distributions (e.g., E. Curtis-Lake et al. 2013; C. Pacifici et al. 2015). On the other hand, if the models are distributed too broadly relative to the data, degeneracies between model parameters and uncertainties in the data may lead to unrealistic fits (e.g., P. Li et al. 2021). Furthermore, models that are overly complex (e.g., too many parameters relative to the constraining power of the data or model parameters that are highly degenerate with each other) may result in poorly constrained results or overfitting (e.g., S. Lower et al. 2020; E. Curtis-Lake et al. 2021).

6. Five Sets of Assumptions in SED Fitting

We examine the effects of adopting five different sets of SED-fitting assumptions on the output radial properties of galaxies.

These sets of assumptions incorporate different dust laws in addition to different priors on the parameters that we fit. They are described in Table 2. We find that the most important priors are those on dust attenuation and star formation histories, as discussed in Section 8.2. From left to right in Table 2, for each set of assumptions, we list the priors assumed for each parameter. We refer to these sets as first to fifth. They start with commonly used assumptions in the first set, and progressively incorporate modifications until we reach the fifth set, whereby all SED-fitting parameters have been modified. In the second and third sets, changes are in the priors for the treatment of dust in the models. Specifically, the priors on the attenuation curve and the amount of dust in the models are varied. For the fourth set, the prior on τ, the star formation history timescale, is varied. Finally, for the fifth set, we additionally change the priors on the stellar ages and metallicity. The effects of changing the priors on the star formation histories are discussed in Appendix A.

We note that the priors on the stellar mass and the initial mass function are kept the same for all assumptions. The prior on the log of the stellar mass (units of solar masses) is uniform over the range [5, 13], and we adopt the initial mass function developed by G. Chabrier (2003). Also, for all sets of assumptions, the priors on the nebular emission are the same. We assume that the nebular and stellar metallicities are equal, the dust-to-metal mass ratio is fixed to 0.3 (e.g., J. Brinchmann et al. 2013), and the ionization parameter behaves according to Equation (25) in J. Chevallard & S. Charlot (2016).

6.1. The First Set: Fixed Dust Law and Uniform Priors

The main features of the first set of assumptions are a fixed attenuation curve and uniform priors on all SED-fitting parameters. These features are informed by the priors commonly adopted in SED fitting (e.g., S. Wuyts et al. 2012; S. Hemmati et al. 2014, 2020; A. Cibinel et al. 2015; T. Morishita et al. 2015; M. Mosleh et al. 2017, 2020; Abdurro'uf & M. Akiyama 2018; Y. Guo et al. 2018; R. Sorba & M. Sawicki 2018; L. Morselli et al. 2019; K. A. Suess et al. 2019). The attenuation curve adopted is that of D. Calzetti et al. (1994), and the optical depth of dust in the rest-frame V band, $\hat{\tau}_V$, spans the range 0–4.

Model colors under this set of assumptions do not trace observed colors, as shown by the poorly overlapping sets of contours in Figure 5. The overlap is quantified by measuring the fraction of model galaxies that lie within a rectangular region in color–color space that encompasses 90% of the observations: $-0.25 < (\text{F125W} - \text{F160W}) < 0.5$ for $z \sim 0.5$ and $z \sim 0.9$ and $0 < \text{F435W} - \text{F775W} < 2.7$ for $z \sim 1.3$. Only 51%, 65%, and 29% of the model colors in the first set lie in the same region in color–color space in the lowest, middle, and highest redshift bin, respectively. We conclude from this that the first set of assumptions may not be the best choice for this data set.

This mismatch between data and models can be attributed mainly to the priors on dust attenuation and stellar age. As only one attenuation curve is assumed, the reddening due to dust in color–color space only varies along one direction; hence, the models concentrate in a swath. A uniform prior on the attenuation means that dust-free and very dusty models are equally likely, so a large fraction of the models lie at colors much redder than the data (see also T. Harvey et al. 2025). Uniform priors on the log maximum age and log SFH timescale yield star formation histories that are rising or roughly constant, producing an abundance of blue colors.
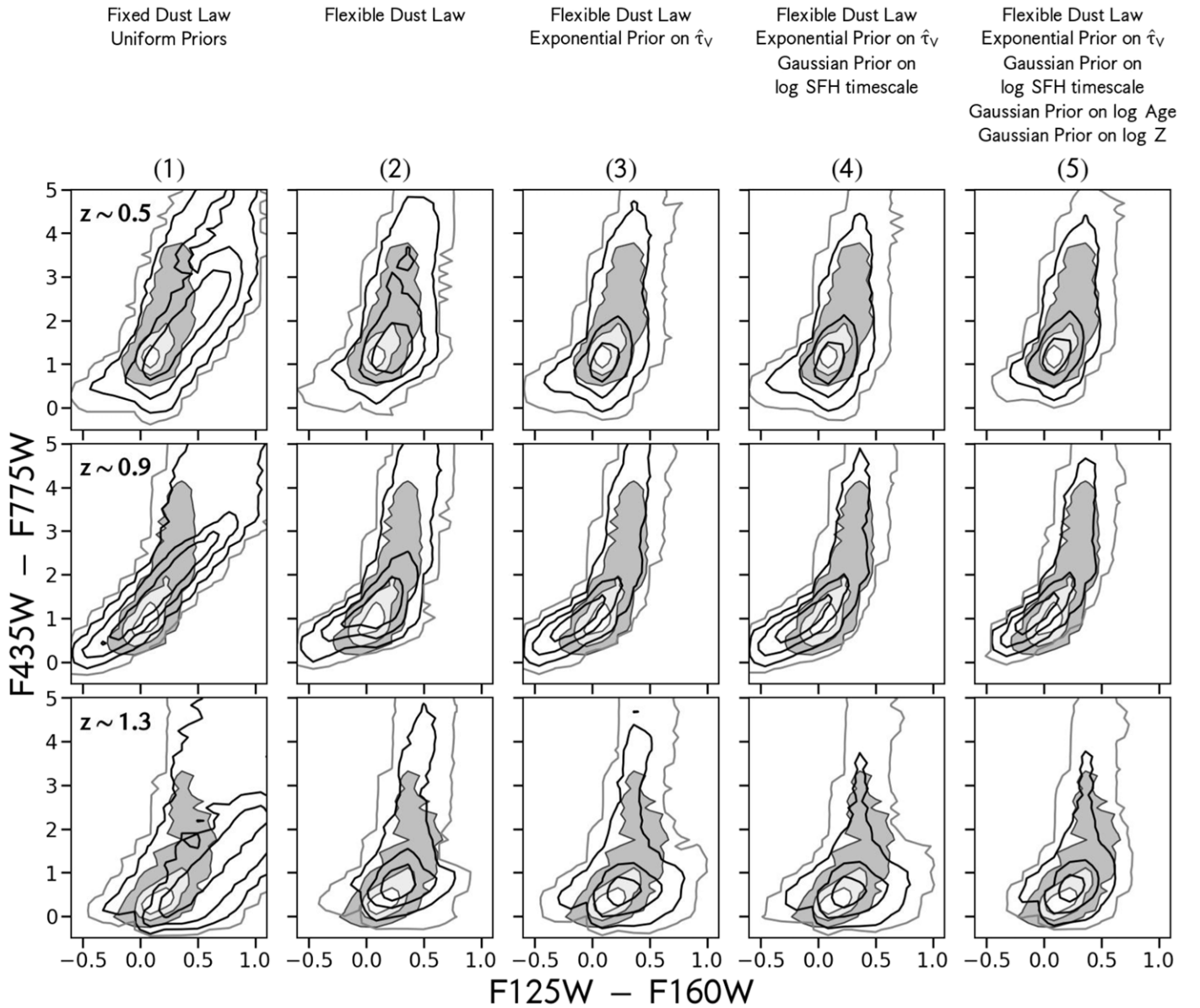
Figure 5. Observed and model color–color distributions for the full galaxy sample for the five sets of assumptions are shown as open and filled contours, respectively. Models under the first set of assumptions do not trace the observations. As assumptions are modified, there is progressively greater overlap until the fifth set is reached, where the overlap is highest. A different set of model assumptions is shown in each column. Three redshift bins are shown from top to bottom. Contour levels are 50%, 16%, and 2% of the maximum number density of models or data. For the models, an additional contour at 0.1% is shown. Note that the offset in the bulk colors of the models at $z \sim 0.9$ relative to the observations results from emission lines contaminating the WFC3 colors and the inclusion of extreme values in the priors on the nebular emission (Section 6.6).

6.2. The Second Set: Flexible Dust Law

For the second set of assumptions, the relation between the slope of the attenuation curve and the rest-frame V-band optical depth in the interstellar medium (ISM) developed by J. Chevallard et al. (2013) is adopted. This is because multiple theoretical and observational studies have found that galaxies possess diverse attenuation curves (see S. Salim & D. Narayanan 2020 for a review on the diversity of attenuation curves).

The J. Chevallard et al. (2013) relation we adopt is (their Equation (10)):

$$n_V^{ISM}(\hat{\tau}_V^{ISM}) = \frac{2.8}{1 + 3\sqrt{\hat{\tau}_V^{ISM}}},$$

where n_V^{ISM} is the power-law slope of the attenuation curve in the rest-frame V band ($\hat{\tau}(\lambda) \propto \lambda^{-n}$), $\hat{\tau}_V^{ISM} = \mu\,\hat{\tau}_V$ is the optical depth in the rest-frame V band due to dust in the ISM, and

$$\mu = \frac{\hat{\tau}_V^{ISM}}{\hat{\tau}_V^{BC} + \hat{\tau}_V^{ISM}},$$

where $\hat{\tau}_V^{BC}$ is the optical depth of the dust originating in the birth clouds surrounding young stars (see S. Charlot & S. M. Fall 2000). Taken together, these equations imply that myriad attenuation curves can be fit under this set of assumptions with varying contributions from young stars and the diffuse ISM. Qualitatively, the resulting attenuation curves are steep at low optical depths and shallow at high optical depths. Because dust

Table 2
Priors Used in SED-fitting

Parameter	Fixed Dust Law Uniform Priors (1) Functional form Range	Flexible Dust Law (2) Functional form Range	Flexible Dust Law Exponential Prior on $\hat{\tau}_V$ (3) Functional form Range	Flexible Dust Law Exponential Prior on $\hat{\tau}_V$ Gaussian Prior on log SFH Timescale (4) Functional form Range	Flexible Dust Law Exponential Prior on $\hat{\tau}_V$ Gaussian Prior on log SFH Timescale Gaussian Prior on log Z (5) Functional form Range
SFH	delayed-tau …	— …	— …	— …	— …
log Age[a]	uniform [8.0, age of Universe]	— —	— —	— —	$\mathcal{N}(9.0, 1.0)$[b] [8.5, age of Universe]
log τ[c]	uniform [8.0, 10.0]	— —	— —	$\mathcal{N}(9.0, 1.0)$[d] [8.3, 10.0]	— —
log $(Z_\star/Z_\odot)$[e]	uniform [−1.0, 0.3]	— —	— —	— —	$\mathcal{N}(-0.6, 0.8)$[b] —
$\hat{\tau}_V$[f]	uniform [0.0, 4.0]	— [0.0, 6.0]	exponential[g] —	— —	— —
Attenuation Curve	Equation (25) C94	Equations (7)–(11) CCWW13	— —	— —	— —
μ[h]	… …	uniform [0.1, 0.7]	— [0.1, 1.0][i]	— —	— —

Notes. Em dashes (—) indicate that priors are the same as the last column to the left containing text. $\mathcal{N}(x, y)$ denotes a Gaussian distribution with mean x and standard deviation y.
[a] Log of the maximum stellar age in years.
[b] The broad Gaussian prior on log age is assumed, as massive galaxies at $z \sim 1$ have light-weighted ages of ~1 Gyr (N. P. Hathi et al. 2009; M. Onodera et al. 2015; V. Estrada-Carpenter et al. 2019; L. Costantin et al. 2022). A broad Gaussian prior on log $Z_\star$ is assumed to account for the range in metallicity typically found for massive galaxies at $z \sim 1$ (R. Maiolino et al. 2008; A. Henry et al. 2013; Y. Guo et al. 2016a; R. Maiolino & F. Mannucci 2019).
[c] Log of the SFH timescale in years, assuming a delayed-tau star formation history (SFR$(t) \propto te^{-t/\tau}$).
[d] A broad Gaussian prior on log τ is assumed, as massive quiescent galaxies at $z \sim 1$ have SFHs that peak ~1–2 Gyr after they begin forming stars (C. Pacifici et al. 2016).
[e] Log of the stellar metallicity in solar units. We assume $Z_\odot = 0.0152$ (E. Caffau et al. 2011; A. Bressan et al. 2012).
[f] Effective V-band optical depth; see S. Charlot & S. M. Fall (2000), E. da Cunha et al. (2008), and J. Chevallard et al. (2013).
[g] The exponential prior is $P(\hat{\tau}_V) = e^{-\hat{\tau}_V}$. This prior is assumed because the distribution of A_V of nearby galaxies in the Sloan Digital Sky Survey (SDSS) is approximately exponential (J. Brinchmann et al. 2004). We expect that the distribution of A_V is similar to that in SDSS at higher redshifts.
[h] Fraction of optical depth arising from the interstellar medium (ISM); see S. Charlot & S. M. Fall (2000), E. da Cunha et al. (2008), and J. Chevallard et al. (2013).
[i] We adjust the prior on μ as well in this set as expanding the range of μ is a small effect.
References. D. Calzetti et al. (1994, hereafter C94); J. Chevallard et al. (2013, hereafter CCWW13).

from young stars and the diffuse ISM can contribute to $\hat{\tau}_V$ in varying amounts, which does not occur under the first set of assumptions, the range on $\hat{\tau}_V$ is expanded to 0–6, and a uniform prior is assumed. We adopt this range from C. J. Walcher et al. (2008). We set priors on both parameters of the J. Chevallard et al. (2013) model, $\hat{\tau}_V$ and μ. The slope of the attenuation curve, n_V^{ISM}, is analytically linked to the optical depth and is not an independent parameter.

The J. Chevallard et al. (2013) relation is based on the results of radiative transfer studies by L. Silva et al. (1998), D. Pierini et al. (2004), R. J. Tuffs et al. (2004), and P. Jonsson et al. (2010). Observationally, several studies find qualitative agreement between observed variations in attenuation curves and what is predicted by the J. Chevallard et al. (2013) attenuation curve relation at low redshift (V. Wild et al. 2011; A. J. Battisti et al. 2017; J. Leja et al. 2017; S. Salim et al. 2018; though see J. Qin et al. 2022) and high redshift (M. Kriek & C. Conroy 2013; B. Salmon et al. 2016; M. Tress et al. 2018, 2019; I. Barišić et al. 2020; G. Nagaraj et al. 2022).

Under the second set of assumptions, in the column second-from-the-left in Figure 5, the model colors trace the data much better than under the first set of assumptions. In the lowest, middle, and highest redshift bins, 83%, 83%, and 84% of the models in the second set lie in the color–color box defined in Section 6.1, respectively. The improved overlap between observations and models is a consequence of the attenuation curve being allowed to vary. The model colors do not extend to colors as red as those under the first set of assumptions because the prior on μ does not permit many models to be dominated by dust from the ISM. However, in Figure 5, the innermost empty contours, i.e., the bulk of the model colors, are redder than the observations. This is due to the uniform prior on $\hat{\tau}_V$. The median ISM optical depth for this prior is 1.2. Therefore, many models have optically thick ISM dust and therefore redder colors than observed.

6.3. The Third Set: Flexible Dust Law and Exponential Prior on $\hat{\tau}_V$

For the third set of assumptions, we adopt an exponentially declining (referred to as "exponential") prior on $\hat{\tau}_V$ instead of a

uniform prior, and the upper limit on μ is extended from 0.7 to 1.0. The exponential prior is based on spectroscopic observations of nearby galaxies, which find that the distribution of attenuations is approximately exponential (Figure 21 in J. Brinchmann et al. 2004). This finding also applies at the higher redshifts studied here because, just as in the local Universe, galaxies with little dust are more common than those with a lot. This is because both the correlation between mass and dust and the shape of the mass function do not significantly change over the redshifts studied here (see T. Garn & P. N. Best 2010; C. Ly et al. 2012; A. Domìnguez et al. 2013; D. Kashino et al. 2013; I. G. Momcheva et al. 2013; S. H. Price et al. 2014; A. Puglisi et al. 2016; R. Ramraj et al. 2017; A. E. Shapley et al. 2022, 2023 and J. Moustakas et al. 2013; A. Muzzin et al. 2013; I. Davidzon et al. 2017; J. Leja et al. 2020, respectively). The upper bound on μ is increased because quiescent galaxies lack young stars, so their dust will mostly arise from the diffuse ISM, implying $\mu \approx 1$ (E. da Cunha et al. 2008).

Under the third set of assumptions, in Figure 5, model colors trace the observed colors to a similar degree as under the second: 87%, 74%, and 82% of the models lie in the same region as 90% of the observations at $z \sim 0.5$, $z \sim 0.9$, and $z \sim 1.3$, respectively. This is because under the exponential prior, there are more models with little attenuation than there are models with high attenuation. This yields bluer model colors that align better with the observed colors. However, in the lowest-redshift bin, model colors extend too blue in F435W − F775W, and at both $z \sim 0.5$ and $z \sim 1.3$, they are too blue and too red in F125W − F160W.

6.4. The Fourth Set: Flexible Dust Law, Exponential Prior on $\hat{\tau}_V$, and Gaussian Prior on log SFH Timescale

For the fourth set of assumptions, a Gaussian prior on the log of the SFH timescale is adopted. Specifically, we adopt a wide Gaussian prior centered on $\log(\tau) = 9.0$ with a lower limit of $\log(\tau) = 8.3$, which was found to better model galaxies than a lower limit of $\log(\tau) = 7.5$ (S. Wuyts et al. 2011; C. Pacifici et al. 2016).

While Gaussian priors may draw the posterior toward the median (see, e.g., P. Li et al. 2018), we adopt a broad Gaussian prior with a standard deviation of 1 dex. In Section 8.2, we show that posteriors are not significantly influenced by their Gaussian priors.

For this set of assumptions, in Figure 5, the model colors trace the observed colors as well as those under the third set. For the lowest-, middle-, and highest-redshift bins, 90%, 77%, and 85% of the model colors in the fourth set lie in the same region as 90% of the observations, respectively. For galaxies with the reddest F435W − F775W colors, models in the fourth set trace them better than in the third as a result of the changes in the prior on the SFH timescale. Under the third set, SFHs peak quickly after the onset of star formation, which produces colors that are much redder than the observations. Under the fourth set, SFHs are also allowed to extend to longer timescales. Therefore, the model colors are bluer, and trace the observations better.

6.5. The Fifth Set: Flexible Dust Law, Exponential Prior on $\hat{\tau}_V$, Gaussian Prior on log SFH Timescale, Gaussian Prior on log Age, and Gaussian Prior on log Z

Finally, under the fifth set of assumptions, Gaussian priors on the log of the maximum age (i.e., the age of the oldest stars) and log of the metallicity are adopted instead of uniform priors. This is because the distributions of the logarithm of the ages of massive galaxies at low and intermediate redshift more closely resemble Gaussians than uniform distributions (A. Gallazzi et al. 2005, 2014). A broad Gaussian prior centered on log (Age) = 9.0 with a lower limit of log(Age) = 8.5 is adopted based on estimates of light- and mass-weighted ages of massive galaxies at $z \sim 1$ (e.g., N. P. Hathi et al. 2009; M. Onodera et al. 2015; P. F. Wu et al. 2018; V. Estrada-Carpenter et al. 2019; L. Costantin et al. 2022). This prior has a standard deviation of 1 dex, which is much larger than the relative change in the age of the Universe from $z = 1.5$ to $z = 0.4$, 0.32 dex. Therefore, this prior is broad enough to cover changes in the ages of galaxies with redshift. The prior on the log of the metallicity is assumed to be a broad Gaussian centered at $\log(Z_\star/Z_\odot) = -0.6$, which is the typical metallicity of low-mass ($\log M_\star \sim 8$) star-forming galaxies (e.g., R. Maiolino et al. 2008; A. Henry et al. 2013; A. Gallazzi et al. 2014; Y. Guo et al. 2016a).

Under the fifth set of assumptions, in the right column of Figure 5, the models trace the observations the best. The color–color region containing 90% of the observations (see Section 6.1) also contains 89%, 89%, and 93% of the models under the fifth set at $z \sim 0.5$, $z \sim 0.9$, and $z \sim 1.3$, respectively.

Strong emission lines in the models result in minor contamination of the colors at $z \sim 0.9$ and $z \sim 1.3$ for all sets of assumptions. This is due to Hα being redshifted into F125W at $z \sim 0.9$ and into F160W at $z \sim 1.3$. Additionally, [O III] is redshifted into F125W at $z \sim 1.3$. As a result, there are small offsets (~0.1 mag) between the innermost contours of the model and observed colors, as seen in the middle and bottom rows in Figure 5. However, these minor offsets do not bias the fits to the radial flux profiles, which are the focus of this work (see Section 8.2). This is because the outskirts of the radial color–color profiles of star-forming galaxies, where the S/N is the lowest, coincide with or lie at the edges of the regions in color–color space where the density of the models is the highest.

6.6. Considerations for the Priors

If one wants to use these priors, here are some considerations that should be made. We focus on the treatment of nebular emission and what may need to change when adapting the priors to other data sets.

Our priors on nebular emission are based on models by J. Gutkin et al. (2016), which explore large variations in metallicity, ionization parameter, and dust-to-metal mass ratio. For certain populations of galaxies, e.g., lower-mass galaxies (stellar masses $\lesssim 10^9 M_\odot$) or at higher redshifts (e.g., $z \gtrsim 2$), more specific variations would be ideal. Setting wide priors on the ionization parameter and nebular metallicity for these populations would be useful.

The priors of the fifth set should still hold under different SPS models, and the results should fall within the modeling uncertainties related to stellar models and stellar tracks because that set is informed by spectroscopic results.

Priors on dust attenuation and the maximum stellar age should still hold when changing the form of the SFH. We assume smooth, parametric star formation histories as our data set comprises several broadband bandpasses. Further, rising and falling SFHs are expected for this redshift and mass range even when using nonparametric SFHs and metallicity histories

(see C. Pacifici et al. 2016). Inevitably, when switching to these, priors on other parameters will not be applicable anymore (e.g., τ, the SFH timescale). However, the priors on dust attenuation and the prior on the maximum stellar age should still hold because these parameters are independent of the choice of SFH and are informed by spectroscopic results. For data sets that contain spectra, especially those with absorption features, adding bursts to SFHs would be beneficial, regardless of the form of the SFH.

We did not assume redshift-dependent priors as our sample is restricted to a small redshift range: $0.4 < z < 1.5$. However, for a data set that spans a larger range in redshift (e.g., $0 < z < 6$), redshift-dependent priors would be useful.

A parameter that could have been varied is the fraction of the NIR luminosity that is due to thermally pulsing asymptotic giant branch (TP-AGB) stars. This was not varied in this work, as our data set lacks rest-frame NIR and mid-infrared data, which are most sensitive to changes in the TP-AGB fraction (e.g., C. Maraston 2005; M. Kriek et al. 2010; S. Zibetti et al. 2013; A. Villaume et al. 2015; S. Lu et al. 2024).

Finally, we note that the fifth set of priors is based on having constraints from the rest-frame UV to NIR. In general, these will be applicable to similar samples with only a portion of the wavelength range available. If, for example, longer wavelengths were to be included and some galaxies showed unexpectedly strong IR fluxes, we might have to reconsider the restrictions we put on the dust and/or age priors and make them wider.

7. Defining Star-forming, Green Valley, and Quiescent Galaxies

We bin the observations (i.e., the full sample) in stellar mass and redshift. Then we break galaxies up into three types depending on their distance from the SFMS (i.e., the relation between stellar mass and SFR; e.g., E. Daddi et al. 2007; D. Elbaz et al. 2007; K. G. Noeske et al. 2007; G. Rodighiero et al. 2010; A. Karim et al. 2011; K. E. Whitaker et al. 2012, 2014; J. S. Speagle et al. 2014; N. Lee et al. 2015; C. Schreiber et al. 2015): star-forming, green valley, and quiescent. We measure integrated measurements of stellar mass and star formation rate by fitting the integrated fluxes under each set of assumptions. These quantities are shown in Figure 6 as gray dots. Each redshift bin is shown in a row, and each set of assumptions is shown in a column. The median SFMS in a given redshift bin and set is shown as a thick black line. Details on the measurement of the median SFMS are provided below. Star-forming galaxies are defined as those with SFRs higher than 0.5 dex below the median SFMS relation and are represented by the blue swaths in the figure. Green valley galaxies are defined to be those galaxies with SFRs from 0.5 to 1.5 dex below the SFMS (green swaths). Quiescent galaxies are defined to be those with SFRs lower than 1.5 dex below the SFMS and are denoted by red swaths.

We note that the definition of star-forming, green valley, and quiescent varies according to the set of assumptions used. Reassuringly, however, the median color–color tracks of star-forming, green valley, and quiescent galaxies defined under each set of assumptions are consistent with each other and discrepant by at most 0.3 mag. We discuss the color–color tracks in more detail in Appendix B.

For each set of assumptions and for each redshift bin, the median SFMS relation is measured by first excluding galaxies

with sSFRs (i.e., SFR/stellar mass) lower than half the inverse of the age of the Universe (e.g., S. Wuyts et al. 2012; C. Pacifici et al. 2016) at the median redshift of the redshift bin. This cut excludes quiescent galaxies such that the median SFMS relation is determined predominantly using star-forming galaxies. All quiescent galaxies have sSFRs lower than this cut. The remaining galaxies are binned in stellar mass in bins 0.25 dex wide such that each bin has at least 10 galaxies. When fitting the SFMS, we fit the median SFR in bins of stellar mass and account for the dispersion around the median, which we take to be half the difference between the 16th and 84th percentiles in SFR. The median SFR as a function of stellar mass is fit using Equation (2) from N. Lee et al. (2015). This function behaves like a power law at low stellar masses and asymptotically approaches a maximum SFR at masses higher than a transitional mass. The fit relation is taken to be the SFMS in a given redshift bin and is shown under each set of assumptions as thick black lines in Figure 6 for all mass and redshift bins we consider.

8. Creation of the Science Profiles

In this Section we describe how radial profiles of stellar mass surface density, SFR surface density, sSFR, A_V, and mass-weighted age are created. Collectively, we refer to these as "science profiles." We describe how these profiles are created for each of the five sets of SED-fitting assumptions in Section 8.1. We examine and explain the differences among them by studying how the models for the different SED-fitting assumptions behave in color–color space with respect to observations in Section 8.2. Additionally, in Section 8.2, we show that the science profiles are not dominated by the adopted priors. Finally, we compare the science profiles fit under the first set of assumptions with those from studies in the literature, which make similar assumptions, in Section 8.3.

8.1. Calculating the Median Science Profiles

First, radial science profiles are created for individual galaxies in the mass-selected sample (Section 3.2). Given the radial flux profiles of a galaxy, the observed SED at each radius is fit for each of the five sets of assumptions. This results in science profiles for the galaxy. Since the radial flux profiles are measured along the semimajor axes of galaxies, the science profiles are circularized by multiplying by the square root of the axis ratios of the galaxies.

Galaxies are then divided into three redshift bins, $0.4 < z < 0.7$, $0.7 < z < 1.1$, and $1.1 < z < 1.5$ (see Figure 2), which are each further divided into two mass bins, $10 \leqslant \log(M_\star/M_\odot) < 10.5$ and $10.5 \leqslant \log(M_\star/M_\odot) < 11.0$. Medians of the science profiles are then created in these bins in 1 kpc sized radial bins. These profiles are shown in Appendix C for all sets of assumptions. To ensure sufficient statistics, at least five galaxies are required to contribute to a median profile at all radii. To characterize the dispersion about the median, the 16th and 84th percentiles are measured.

Individual science profiles incorporated into the median are required have adequate S/N at a given radius in key wave bands. The rest-frame UV is important for accurate SED fitting because it is particularly sensitive to SFR, age, and dust (J. Pforr et al. 2012; V. Buat et al. 2014). Therefore, an S/N of at least 5 is required at a given radius in the wave band that spans the rest-NUV, namely F435W for $z \leqslant 0.8$ and F606W for
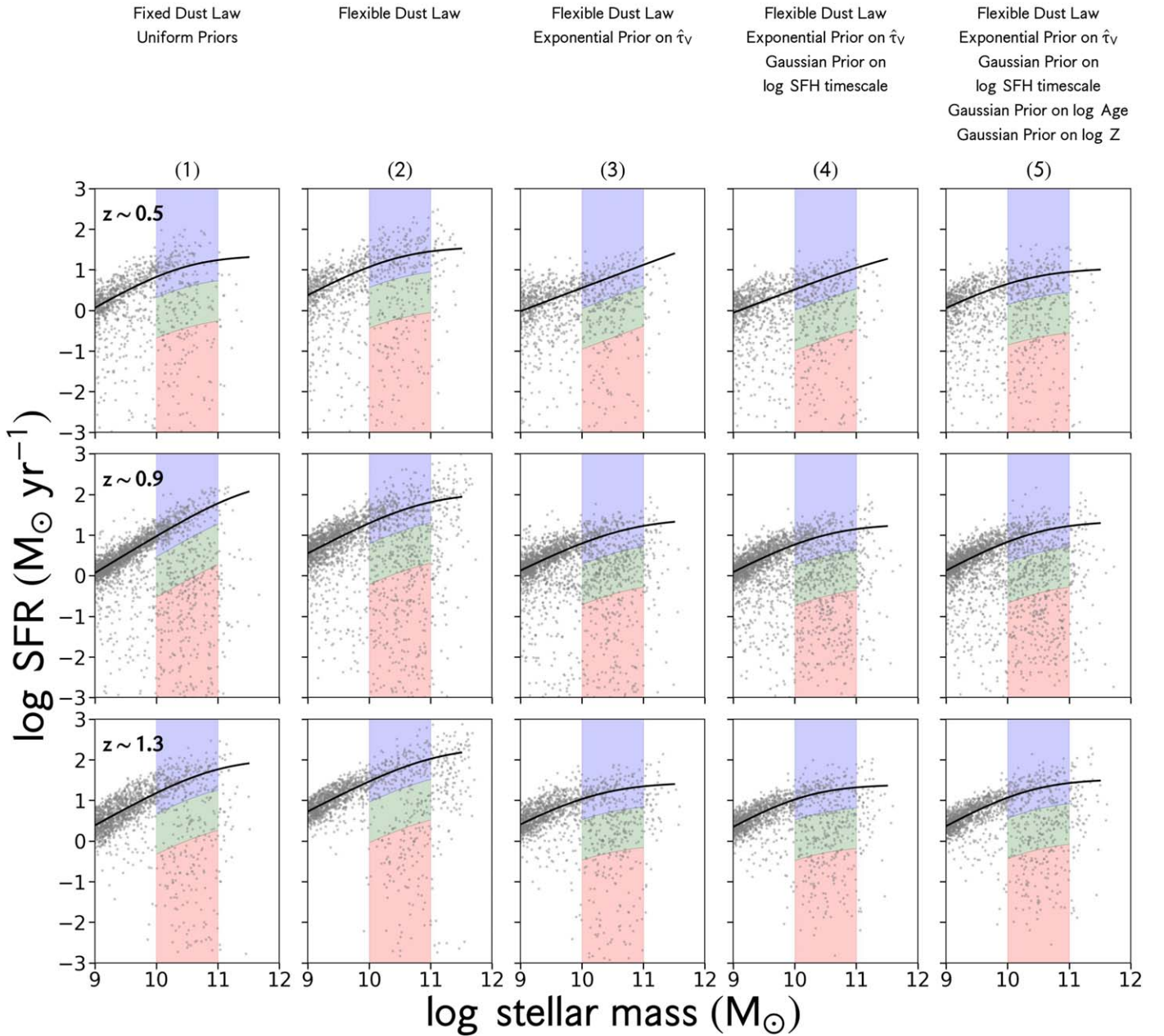
Figure 6. The stellar mass–SFR diagram for five sets of SED-fitting assumptions and all redshift bins. Galaxies are selected to be star-forming, green valley, or quiescent according to their location with respect to the median star formation main sequence (SFMS). The measurement of the SFMS and selection of galaxies is performed for each set independently. Therefore, the SFMS and selection of galaxies differ set by set. Galaxies are shown as gray points. A different set of assumptions is in each column. Three redshift bins are shown in each of the rows. Median SFMS relations are shown as thick black lines. Star-forming, green valley, and quiescent galaxies are denoted by the blue, green, and red swaths, respectively.

$z > 0.8$. Further, this requirement must be met in at least three radial bins. As a note to the reader, this cut is only for incorporation into the median, unlike the cuts described in Section 4.

8.2. Explaining the Behavior of the Science Profiles Using Color–Color Diagrams

To showcase the most important changes in the profiles among the five sets of assumptions, one example bin in mass and redshift is discussed: namely $10.0 < \log (M_\star/M_\odot) < 10.5$ and $z \sim 0.9$. The profiles for this bin are shown in Figure 7 for each of the sets of assumptions in the columns. The differences

are explained with the behavior of the models in color–color space in Figure 8.

The most important differences are listed below and indicated with annotations in Figures 7 and 8. Most of these arise when a flexible dust law and an exponential prior on the optical depth in the rest-frame V band are assumed.

1. In the first set, models with lower sSFRs have redder F435W − F775W colors, become older with redder F125W − F160W color, and dustier with redder F435W − F775W and F125W − F160W colors (left column in Figure 8). There is a sharp transition in the F435W − F775W color between models with high and
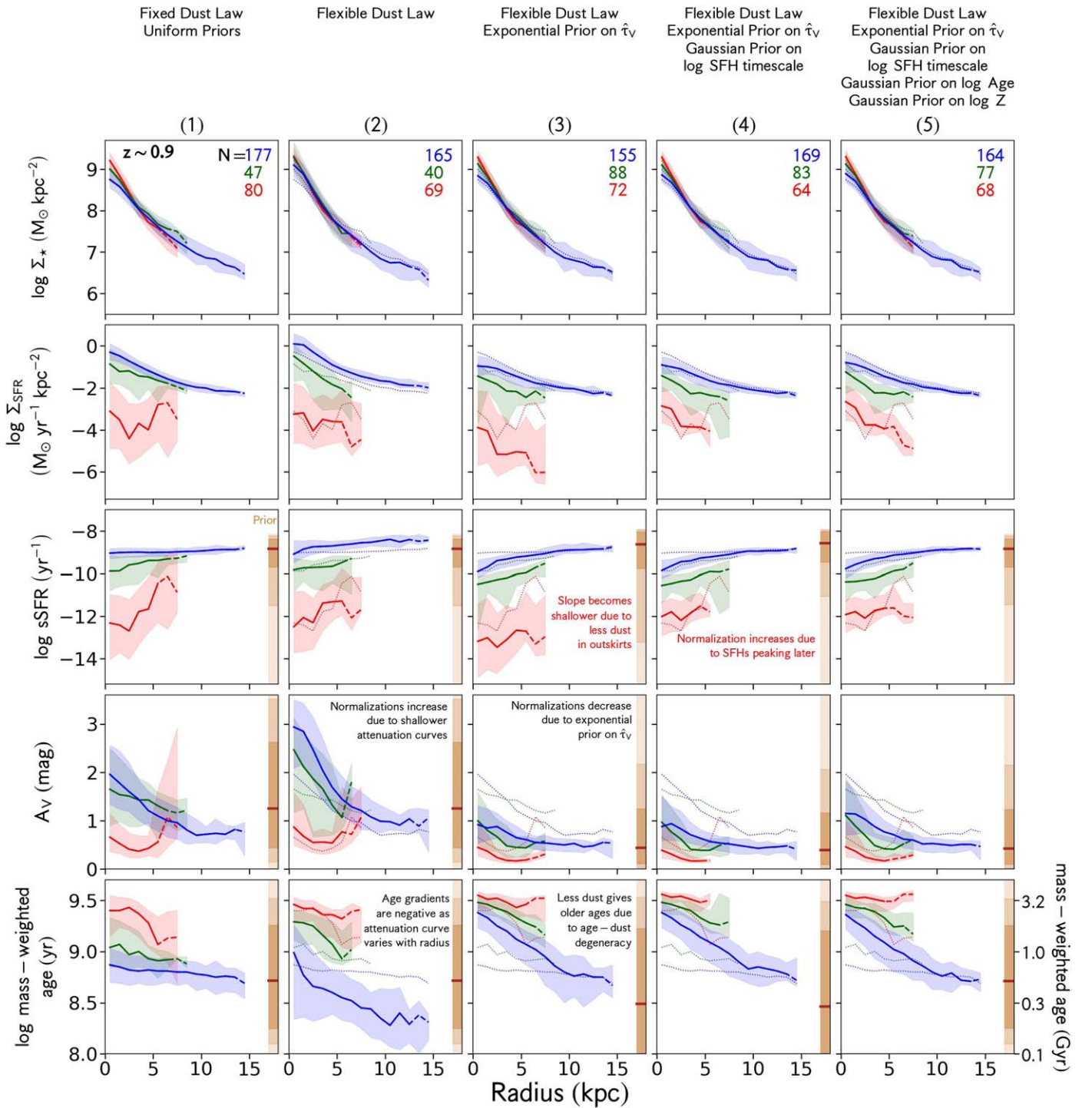
Figure 7. Science profiles for one stellar mass ($\log(M_\star/M_\odot) \sim 10.3$) and redshift bin ($z \sim 0.9$) created under five sets of SED-fitting assumptions from left to right. From top to bottom, we show profiles of the $\Sigma_\star$, $\Sigma_{\rm SFR}$, sSFR, $A_{\rm V}$, and mass-weighted age. Star-forming, green valley, and quiescent galaxies are shown in blue, green, and red, respectively. Median profiles are plotted as thick solid lines, where at least 10 galaxies contribute, and as dashed lines where at least five contribute. The 16th–84th percentile ranges are shown as shaded regions. The numbers of galaxies that contribute to the profiles are given in the top row. Profiles for the first set of assumptions are shown in the other panels as dotted lines. Priors for the five sets of assumptions are shown in brown. Their medians are shown as horizontal solid lines. The 16th–84th percentile ranges, the 5th–95th percentile ranges, and the full extents of the priors are shown as increasingly lighter brown shaded regions.

low sSFRs, a lot and a little dust, and young and old ages. The color–color tracks of quiescent galaxies cross this transition. These galaxies have steeply rising sSFR and $A_{\rm V}$ profiles and steeply declining age profiles (left column in Figure 7). Color–color tracks of star-forming galaxies have bluer colors than this transition. These galaxies have flat sSFR profiles and $A_{\rm V}$ and age profiles

that decline mildly with radius. Green valley galaxies lie between these extremes.

2. In the second set, when assuming a flexible dust law, models also have lower sSFRs with redder F435W − F775W colors, but the trends between age and dust in the models and F435W − F775W and F125W − F160W colors are more complex than those in the first set
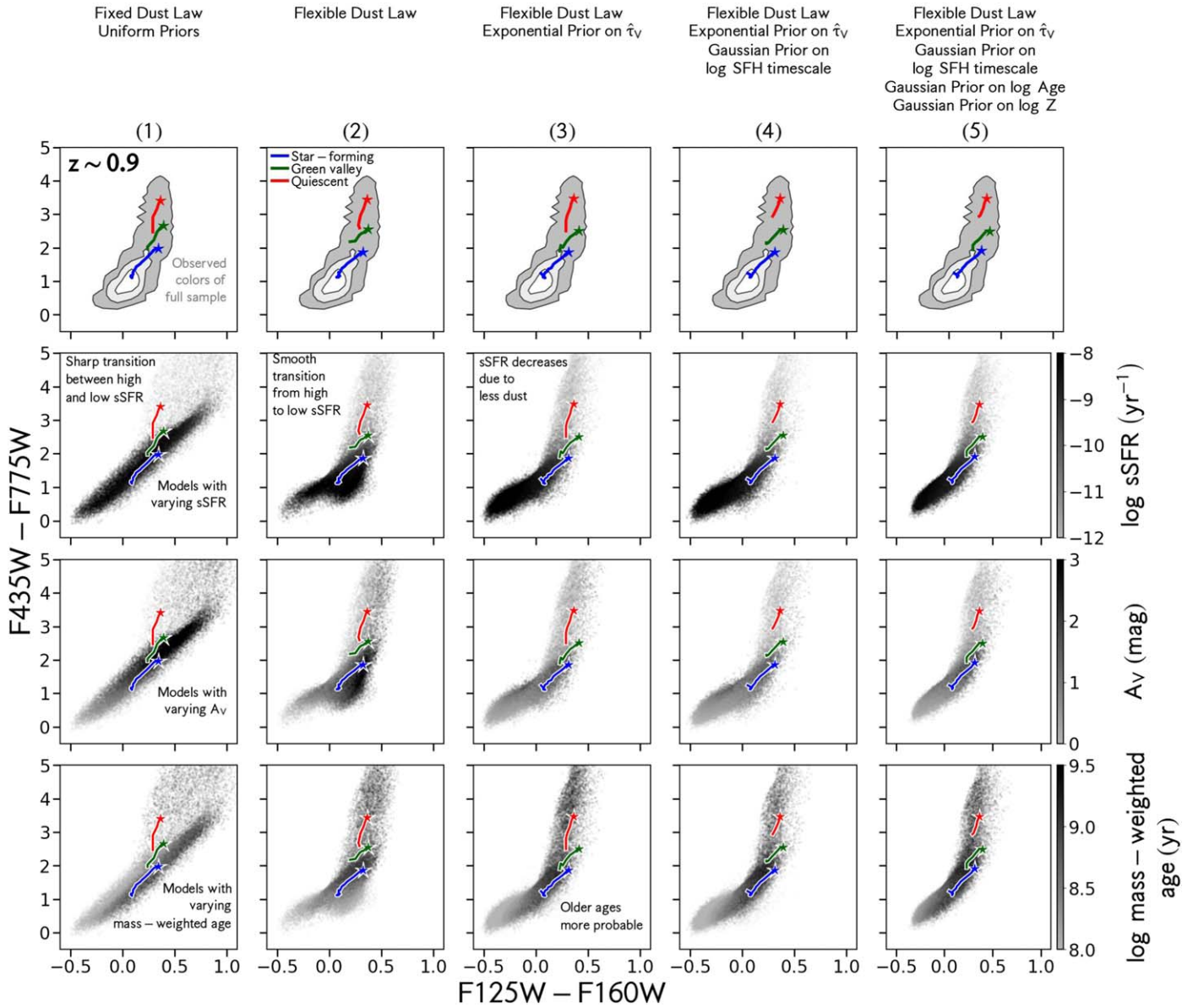
Figure 8. Color–color tracks for one stellar mass (log $(M_\star/M_\odot)$ ~ 10.3) and redshift (z ~ 0.9) bin for the five sets of SED-fitting assumptions are shown from left to right. For comparison, the middle row in Figure 5 is reproduced in the top row. Star-forming, green valley, and quiescent galaxies are shown in blue, green, and red, respectively. Median colors of the centers of galaxies are shown as stars and color–color tracks become bluer with increasing radius. Model colors for each set of assumptions are shown in different columns and are colored by log sSFR, A_V, and log mass-weighted age from the second to fourth rows. Under the first set of assumptions, there is a sharp transition in the F435W − F775W color between models with high and low sSFRs, a lot and little dust, and young and old ages. When a flexible dust law is assumed, there is a smooth transition in F435W − F775W color. When adopting an exponential prior on the dust, normalizations in the model sSFRs and ages change due to the age–dust degeneracy.

(second column in Figure 8). There is no longer a sharp transition, but a smooth one in F435W − F775W color. Consequently, quiescent galaxies have sSFR and A_V profiles that rise mildly with radius and age profiles that decline mildly with radius (second column in Figure 7). Age profiles of star-forming galaxies decline with radius because the attenuation curve varies with radius. The normalizations of the A_V profiles for all galaxies increase because attenuation curves are shallower than that assumed in the first set.

3. In the third set, assuming an exponential prior on optical depth affects the A_V, age, and sSFR profiles (third column in Figure 7). Normalizations of the A_V profiles decrease because models with little to no dust are more common

than those with a lot. Less dust at all radii also results in older ages at all radii due to the age–dust degeneracy. Quiescent galaxies have shallower sSFR profiles because there is less dust, and therefore lower sSFR, in the outskirts of these galaxies.

4. In the fourth set, the normalizations of the sSFR profiles of quiescent galaxies increase when assuming a Gaussian prior on the log of the SFH timescale (fourth column in Figure 7). This is because the SFHs of these galaxies peak later in time, which raises the SFR and sSFR at later times.

5. There are no significant changes between profiles in the fifth set and those in the fourth (right column in Figure 7).

There are several features of the median profiles that are the same among all of the sets of assumptions. It is reassuring to

see these qualitative similarities, as these trends have been found by multiple studies. Namely, star-forming galaxies have the lowest stellar mass surface densities, the highest SFR surface densities and sSFRs, the most dust, and the youngest ages. Quiescent galaxies have the highest stellar mass surface densities, the lowest SFR surface densities and sSFRs, the least dust, and the oldest ages. Green valley galaxies lie in between these extremes in all cases.

We also examine whether priors in each set dominate the posteriors. This happens when their medians and percentile ranges are similar. In this work, neither the medians nor the 16th–84th percentile ranges of the priors are similar to those of the profiles. This can be seen by comparing the brown shaded regions in Figure 7, which indicate the priors, with the profiles. This is true even in the outskirts of galaxies, where the S/N is the lowest. This is because we have a strict limit on the S/N. In the third set, we purposely down-weight the models with large A_V; hence, the posteriors become narrow and more similar to the shape of the prior. This is what we expect to see based on the studies that informed the priors adopted in the third set (see Section 6.3) and the validation against profiles measured from spectroscopic data sets (see Section 9.2).

8.3. Comparison of Profiles Created under the First Set with Studies that Adopt Similar Assumptions

We now compare science profiles created under the first set with those from the literature, which adopt similar assumptions and data sets. In summary, they are consistent wherever there is overlap in redshift and stellar mass. Below, we walk through each of the studies.

E. J. Nelson et al. (2016) measured stellar mass surface density profiles for galaxies on and below the SFMS at $0.7 < z < 1.5$. These are consistent with profiles for star-forming and green valley galaxies in this work.

W. Wang et al. (2017) measured sSFR and A_V profiles of star-forming galaxies at $0.4 < z < 1.5$. Their A_V profiles agree with those presented here. Their sSFR profiles agree with those for the first set over $10 \leqslant \log(M_\star/M_\odot) < 10.5$. At higher stellar masses, $10.5 \leqslant \log(M_\star/M_\odot) < 11$, sSFR profiles rise with radius, but W. Wang et al. (2017) found shallower profiles than those for the first set here. We note that this work cautions that their sSFR measurements might be significantly affected by oversimplified assumptions adopted in SED fitting.

Abdurro'uf & M. Akiyama (2018) measured sSFR profiles for star-forming, green valley, and quiescent galaxies at $0.8 < z < 1.8$. Their profiles are qualitatively consistent with those for the first set, although normalizations differ for two reasons. First, their sample is selected using spatially integrated SFRs that are measured by combining rest-UV and rest-IR luminosities. Our galaxies are selected using spatially integrated SED fits. Second, we define quiescent galaxies differently. Normalizations differ even if quiescent galaxies are defined in the same manner due to differences in the sample selection.

L. Morselli et al. (2019) measured sSFR profiles for galaxies above, on, and below the SFMS at $0.2 < z < 1.2$. While their profiles qualitatively agree with those for the first set, normalizations differ for the same two reasons listed in the comparison with Abdurro'uf & M. Akiyama (2018).

Lastly, E. J. Nelson et al. (2021) measured sSFR profiles of galaxies on and below the SFMS at $0.7 < z < 1.5$. These agree

with profiles of star-forming and green valley galaxies created under the first set.

9. Choosing a Set of Assumptions

In this Section, we determine which set of assumptions in Table 2 is most appropriate for our galaxy sample; we conclude that the fifth set is. To make this determination, we perform three tests for each of the five sets. First, in Section 9.1, we examine Bayesian evidences. Next, in Section 9.2, we compare the SFR surface density and dust profiles with those of nearby galaxies that have these profiles measured from spectroscopy, which are more accurate. Finally, in Section 9.3, we examine dust profiles as a function of galaxy inclination.

9.1. Comparison of Bayesian Evidences

Sets of SED-fitting assumptions may be compared by estimating the Bayesian evidence, which is the product of the likelihood and the prior that is integrated over the entire parameter space. The ratio of the Bayesian evidences of two models, also known as the Bayes factor, is often used to determine whether one model fits the data better than the other (e.g., Y. Han & Z. Han 2012, 2014, 2019; J. Chevallard & S. Charlot 2016; B. Salmon et al. 2016; A. J. Lawler & V. Acquaviva 2021; Y. Han et al. 2023). Here we compare the Bayesian evidence of the fifth set of assumptions with that of the other sets for SED fits to the *spatially integrated fluxes* for the full sample (Section 3.1).

Histograms of the Bayes factors for the fifth versus each of the other four sets are shown in Figure 9. In each panel of Figure 9, positive values indicate a preference for the fifth set, and negative values denote a preference for the set being compared. A value of zero indicates no preference for either. In order to interpret these distributions and determine the strength of the preference toward one set, the qualitative criteria by R. E. Kass & A. E. Raftery (1995) are adopted. The strength of the preference in favor of one model is categorized as "weak," "positive," "strong," or "very strong," depending on the value of the Bayes factor. These categories are indicated with the shaded regions in Figure 9. In the leftmost panel, the histogram is centered at a Bayes factor of about 3. This means that the fifth set is preferred to the first at a "positive" confidence level. In the second through fourth panels, the histograms gradually move toward a value of zero. The fifth set is preferred to the second at a "weak" confidence level. There is no preference between the third and fifth or fourth and fifth sets.

9.2. Comparison of SFR Surface Density and A_V Profiles with Results from Spectroscopy

We now compare profiles created under each set of assumptions at $z \sim 0.5$ with those from the literature that are based on spatially resolved spectroscopic surveys of galaxies at $z \sim 0$. These comparisons are meant as first-order sanity checks on the profiles. While we expect the profiles evolve with redshift over $0 < z < 0.5$, we do not expect this to be significant (by $\lesssim 0.4$ dex in SFR surface density and by $\lesssim 0.3$ mag in A_V). Further justifications for this are provided in Section 9.2.3.

Comparisons with SFR surface density (Σ_{SFR}) profiles of quiescent galaxies from SAMI (J. J. Bryant et al. 2015; A. M. Medling et al. 2018; A. M. Medling 2025, private communication) are shown in Figure 10 and examined in
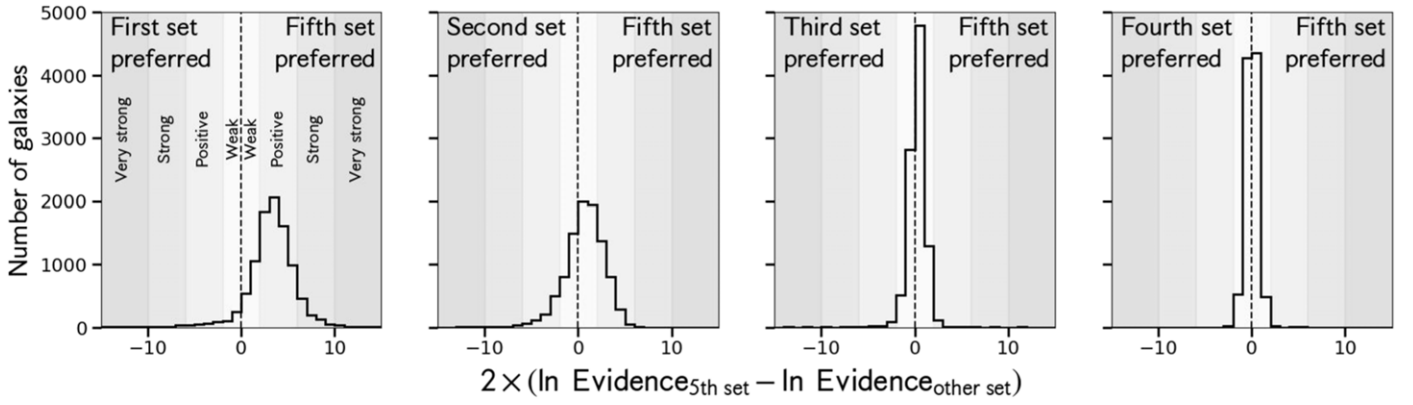
Figure 9. The Bayes factor is used to evaluate whether one model fits the data better than another. In each panel, from left to right, the distribution of the Bayes factor of the fifth set vs. that for the other four sets is shown. In each panel, the distribution of two times the natural log of the Bayes factor, $2 \ln K$ (see Section 9.1), is shown. We adopt the significance criteria developed by R. E. Kass & A. E. Raftery (1995) in order to interpret these distributions. These are indicated with the shaded regions in the leftmost panel and labeled accordingly. In the leftmost panel, the bulk of the distribution is positive, indicating that the fifth set is favored when comparing it with the first. In the next panel, the fifth set is preferred to the second at a "weak" confidence level. In the following panels, there is no preference between the third and fourth sets and the fifth set.
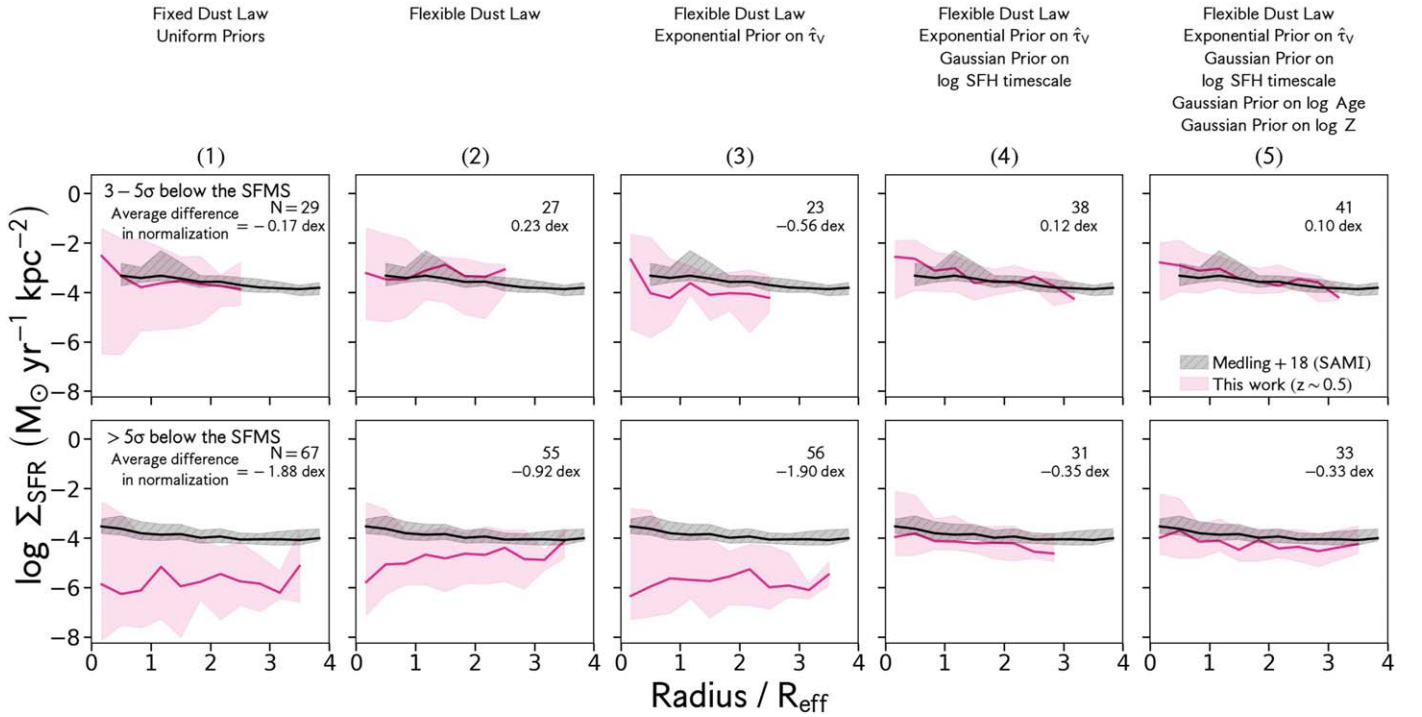
Figure 10. SFR surface density profiles of quiescent galaxies at $z \sim 0.5$ (magenta) are compared with those measured from spectroscopy by A. M. Medling et al. (2018) at $z \sim 0$ (black). The 16th–84th percentile ranges are shown as shading. The average differences in normalization between profiles for each set and those at $z \sim 0$ are given. Profiles for the fifth set have the smallest difference. This is because the fifth set assumes Gaussian priors on the log SFH timescale, log age, and log metallicity, with the former having the largest effect. We compare with galaxies in A. M. Medling et al. (2018) that overlap ours in stellar mass and SFR. The top row shows galaxies with $10.0 < \log (M_\star/M_\odot) < 11.0$ and which are 3σ–5σ below the SFM, where σ is the scatter in the SFMS. The bottom row shows the same mass range but for galaxies that are $>5\sigma$ below the SFMS.

Section 9.2.1. Comparisons with dust profiles of star-forming galaxies from MaNGA (K. Bundy et al. 2015; M. J. Greener et al. 2020; M. J. Greener 2025, private communication) are shown in Figure 11 and examined in Section 9.2.2. In both figures, profiles for each set are plotted as magenta lines, and those from the literature are shown as black lines. We measure the average differences in normalization between them. Profiles for the fifth set have the smallest difference and therefore agree the best with those from spectroscopy.

Profiles from the literature are normalized by the effective radius. Therefore, we do the same. We adopt PSF-corrected

effective radii and axis ratios measured in the F160W bandpass from A. van der Wel et al. (2012).

9.2.1. Comparison with SFR Surface Density Profiles of Quiescent Galaxies

To compare with SFR surface density profiles of quiescent galaxies from A. M. Medling et al. (2018), we choose a subset of their sample that overlaps ours in stellar mass and SFR (Figure 10). We compare with their profiles over stellar masses $10 < \log (M_\star/M_\odot) < 11$. Their profiles are compared with ours

18
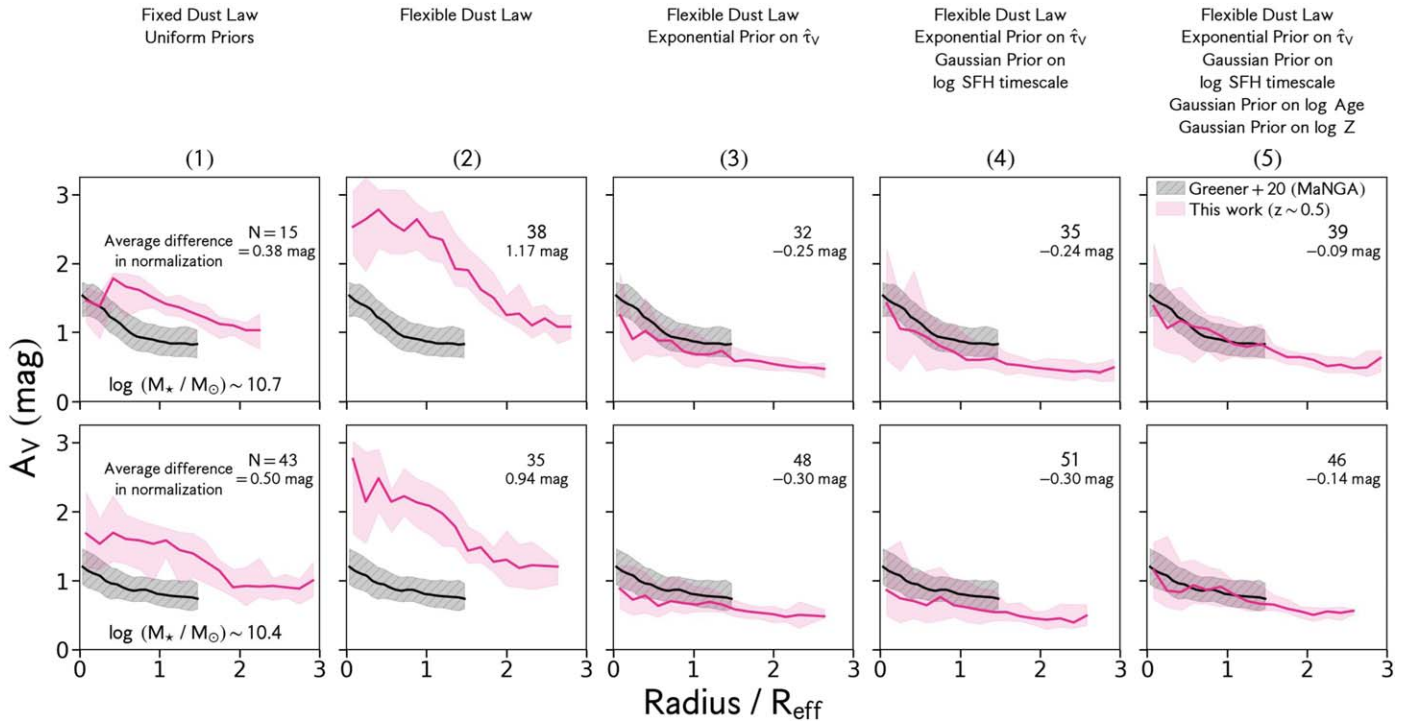
Figure 11. A_V profiles of star-forming galaxies at $z \sim 0.5$ (magenta) are compared with those at $z \sim 0$ measured from spectroscopy by M. J. Greener et al. (2020; black). Interquartile ranges are indicated by shading. We choose galaxies that overlap two of their bins in stellar mass ($10.58 < \log(M_\star/M_\odot) < 10.86$ and $10.26 < \log(M_\star/M_\odot) < 10.58$) and also apply their cut in axis ratio (>0.35). Average differences in normalization are given, and those for the fifth set are the smallest. This is primarily because the fifth set adopts an exponential prior on the amount of dust.

at high and low SFRs: 3σ–5σ below the SFMS and 5σ and greater, where σ is the scatter in the SFMS. We assume $\sigma = 0.5$ dex, and our results are not affected by choosing a smaller or larger value. At high and low SFRs, profiles created under the fifth set have the smallest average difference in normalization (0.1 and -0.33 dex, respectively). Therefore, they agree the best. This is because the fifth set assumes Gaussian priors on the log SFH timescale, log age, and log metallicity, with the former having the largest effect. Profiles for the fourth set, which also assume the same prior on log SFH timescale, perform marginally worse. This is because this set assumes uniform priors on log age and log metallicity. For the first three sets, differences in normalization are much larger. This is because they assume a uniform prior on the log SFH timescale.

9.2.2. Comparison with A_V Profiles of Star-forming Galaxies

To compare with A_V profiles of star-forming galaxies from M. J. Greener et al. (2020), we choose a subset of their sample that overlaps ours in stellar mass, SFR, and axis ratio (Figure 11). Their profiles are measured for galaxies with SFRs that are >0.71 dex below the SFMS. We choose galaxies that overlap two of their bins in stellar mass ($10.58 < \log(M_\star/M_\odot) < 10.86$ and $10.26 < \log(M_\star/M_\odot) < 10.58$) and also apply their cut in axis ratio (i.e., greater than 0.35). At high and low stellar masses, profiles for the fifth set have the smallest average difference in normalization (-0.09 and -0.14 mag, respectively). Therefore, they agree the best. This is mainly because the fifth set assumes an exponential prior on the amount of dust, and, to a lesser extent, Gaussian priors on log age and log metallicity. Profiles for the third and fourth sets, which assume the same prior on the amount of dust, perform slightly worse. This is because they assume uniform priors on log age and log metallicity. For the first two sets,

differences in normalization are the largest. This is because they assume a uniform prior on the amount of dust.

9.2.3. Justifications for Comparing Profiles at $z \sim 0$ and $z \sim 0.5$

SFR surface density profiles of quiescent galaxies at $z \sim 0.5$ are compared with those from spectroscopy at $z \sim 0$ as a sanity check. We do not expect perfect agreement, as mild evolution with redshift has been found. Profiles are expected to decrease in normalization by ~ 0.4 dex with time over $0 < z < 0.5$ at fixed mass. This is because integrated sSFRs decrease by this amount at fixed mass (M. Fumagalli et al. 2014; R. M. McDermid et al. 2015; N. Salvador-Rusiñol et al. 2020).

A_V profiles of star-forming galaxies at $z \sim 0.5$ are also compared with those from spectroscopy at $z \sim 0$ as a sanity check. We do not expect perfect agreement as mild evolution with redshift has been found. Profiles are expected to increase by ~ 0.3 mag at most with time over $0 < z < 0.5$ at fixed mass. This is because integrated dust attenuation measured from spectroscopy increases at most by this amount at fixed mass (A. Domìnguez et al. 2013; R. Ramraj et al. 2017; A. E. Shapley et al. 2022).

SFR surface density profiles of quiescent galaxies at $z \sim 0$ are measured differently from those in this work. However, they are compatible. The former are measured by averaging over regions that are selected to be ionized by young, massive stars. This selection is based on emission-line diagrams. Profiles in this work are measured by averaging over annuli containing rest-UV light, which predominantly arises from young, massive stars, but could arise from other sources, namely X-ray AGNs and old stars. We have removed the first from our sample (Section 2.4) and the second are not observed to be predominant at the stellar masses and redshifts examined
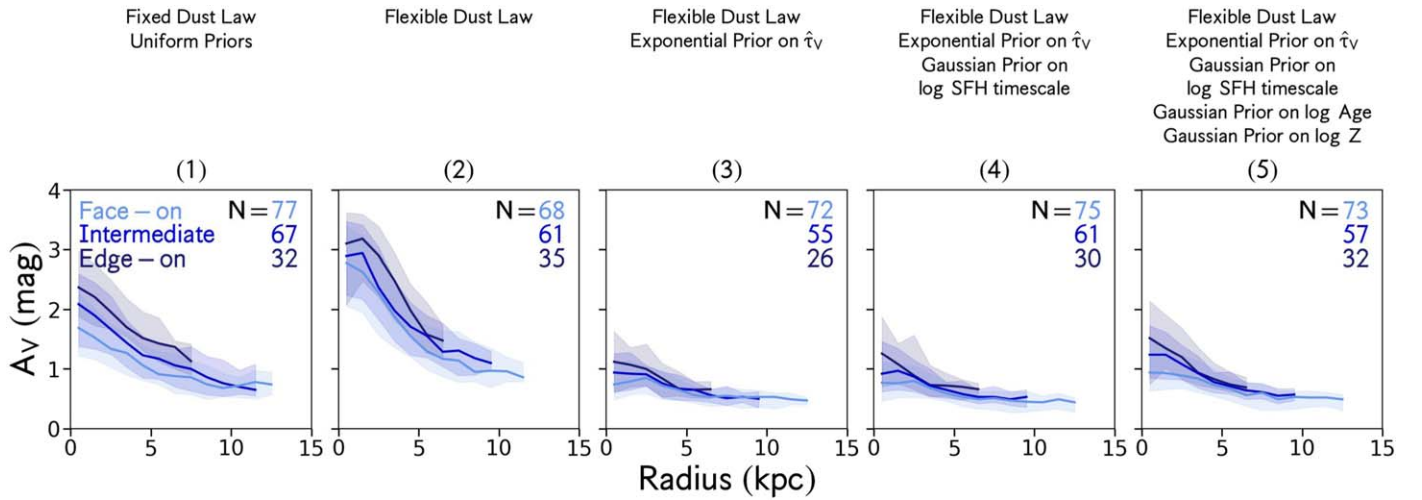
Figure 12. A_V profiles of star-forming galaxies as a function of axis ratio/inclination are qualitatively compared with expectations based on observations of disk galaxies at $z \sim 0$. This is because star-forming galaxies at the stellar masses and redshifts considered in this work are generally disk galaxies. As disk galaxies become more inclined, it is expected that the largest increases in the amount of dust are in their centers and the smallest are in their outskirts. Therefore, as inclination increases, A_V profiles should steepen. Profiles for the first and second sets do not display the expected behavior. This is due to the uniform prior on the dust. However, profiles for the third, fourth, and fifth sets do demonstrate the expected behavior. This is due to the exponential prior on the dust. Profiles for each set in one stellar mass ($\log (M_\star/M_\odot) \sim 10.3$) and redshift ($z \sim 0.9$) bin are shown. Galaxies are divided by axis ratio. Face-on ($b/a > 0.64$), intermediate inclination ($0.34 < b/a < 0.64$), and edge-on galaxies ($b/a < 0.34$) are shown as light, medium, and dark-blue lines, respectively.

in this work (C. Le Cras et al. 2016; M. L. L. Dantas et al. 2020).

While different SFR tracers are used to measure SFR surface density profiles of quiescent galaxies at $z \sim 0$ and those in this work, we find that this does not significantly affect our comparison. The former are measured using Hα luminosities corrected for dust. The latter come from dust-corrected rest-UV luminosities. These trace the SFR on different timescales (~ 10 Myr for emission lines and ~ 100 Myr for UV continuum; see, e.g., R. C. Kennicutt 1998; R. C. Kennicutt & N. J. Evans 2012) and the calibration from rest-frame luminosity to SFR depends on the burstiness of the SFH (e.g., N. Emami et al. 2019; J. A. Flores Velázquez et al. 2021). However, these measurements of the SFR can be reconciled because massive galaxies at both $z \sim 0$ and $z \sim 0.5$ are not observed to have bursty SFHs (see, e.g., Y. Guo et al. 2016b; C. Hahn et al. 2017; J. Trussler et al. 2020; M. Bravo et al. 2023; A. Weibel et al. 2023). This suggests that the SFRs measured from emission lines and UV continuum should be similar for massive galaxies at both $z \sim 0$ and $z \sim 0.5$.

A_V profiles of star-forming galaxies at $z \sim 0$ and those in this work are measured differently. However, they are compatible. The former are measured by averaging over regions that are selected to be ionized by young, massive stars. The latter are measured differently, and we address this above. A_V is measured from spectroscopy at $z \sim 0$ and from photometry in this work. These measurements are comparable. This is because both quantify the total amount of attenuation suffered by young stellar populations, which is due to birth clouds and diffuse dust in the ISM. A caveat is that A_V from spectroscopy is measured over regions with dust from birth clouds and the ISM, whereas A_V from photometry is measured over regions with both types of dust and with dust only from the ISM.

9.3. Comparing Dust Profiles of Star-forming Galaxies as a Function of Inclination

We examine dust profiles for each set as a function of galaxy inclination and qualitatively compare with expectations based

on observations of disk galaxies at $z \sim 0$ (Figure 12). Star-forming galaxies at the stellar masses and redshifts examined in this work are disk galaxies in general (e.g., S. A. Kassin et al. 2012; A. van der Wel et al. 2014; R. C. Simons et al. 2017). Since disk galaxies often have more dust in their centers than in their outskirts, it is expected that when they are viewed from face-on to edge-on, the largest increases in the amount of dust are seen in their centers and the smallest are seen in the outskirts (Y. I. Byun et al. 1994; R. Giovanelli et al. 1994; R. F. Peletier et al. 1995; L. E. Kuchinski et al. 1998; R. J. Tuffs et al. 2004; M. Riello & F. Patat 2005). Therefore, as disk galaxies become more inclined, dust profiles should steepen.

Profiles are examined at $z \sim 0.9$ because there are enough galaxies at this redshift to divide the sample into three bins of inclination with at least 25 galaxies each. For these three bins in inclination (i.e., axis ratio), we measure A_V profiles for the five sets of assumptions (Figure 12). The profiles for the first and second sets do not follow the expected behavior. Instead, as inclination increases, the profiles increase in normalization at all radii. This is due to the uniform prior on the dust. However, the profiles for the third, fourth, and fifth sets demonstrate the expected behavior—as galaxies become more inclined, they steepen. This behavior is due to the exponential prior on the dust.

10. sSFR Profiles under the Fifth Set of Assumptions and Comparisons with the First Set

10.1. Descriptions of the sSFR Profiles under the Fifth Set and Fits to Them

In this Section, we examine median SSFR profiles created under the fifth set of assumptions, our chosen set. They are shown in the top two rows of Figure 13. The dispersion around these median profiles can be large, indicating that individual profiles can have a variety of shapes. In the bottom two rows of Figure 13, linear fits to these profiles are shown. They are fit out to radii where at least 10 galaxies contribute. Errors on the median profiles are used in the fits and are shown as shaded
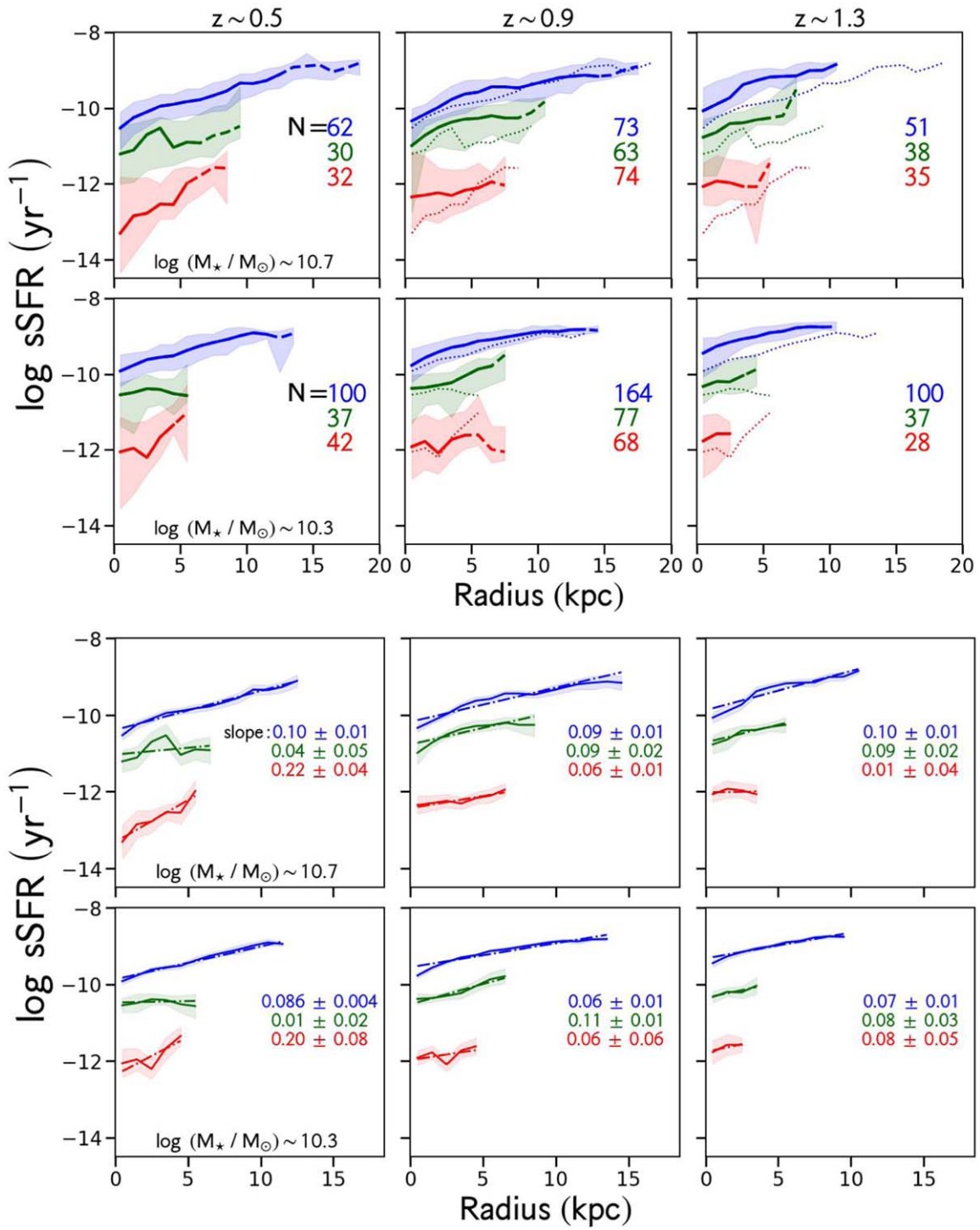
Figure 13. Median specific star formation rate profiles created under the fifth set of assumptions are shown. In the bottom two rows, fits to the median profiles are shown as dashed–dotted lines. The profiles of green valley galaxies at $z \sim 1.3$ have similar slopes to those of quiescent galaxies at $z \sim 0.9$, which we expect them to evolve into. This suggests that they quench at all radii at the same time. Profiles of green valley galaxies at $z \sim 0.9$ are shallower than those of quiescent galaxies at $z \sim 0.5$, which we expect them to evolve into. This suggests inside-out quenching. Median profiles in each mass and redshift bin indicated are shown as thick solid lines and dashed lines wherever at least 10 and at least five galaxies contribute to the profile, respectively. Median profiles are fit at radii where at least 10 galaxies contribute. Median profiles in the lowest-redshift bin are shown as thin dotted lines in other panels. The 16th–84th percentiles as a function of radius are indicated by the shading.

areas in Figure 13. The errors are the dispersions about the median profiles divided by the square root of the number of galaxies that contribute at each radius. Now we examine SSFR profiles for star-forming, green valley, and quiescent galaxies.

Star-forming galaxies have median sSFR profiles with similar slopes at all redshifts (0.06 ± 0.01–0.1 ± 0.01 dex kpc^{-1}). Green valley galaxies have similar slopes to the star-forming galaxies at $z \sim 0.9$ and $z \sim 1.3$ (0.08 ± 0.03–0.11 ± 0.01). However, at

$z \sim 0.5$, they have flatter slopes than the star-forming galaxies (0.01 ± 0.02 and 0.04 ± 0.05 versus 0.086 ± 0.004 and 0.10 ± 0.01). Quiescent galaxies also have similar slopes to those of star-forming and green valley galaxies (0.01 ± 0.04–0.08 ± 0.05) at $z \sim 0.9$ and $z \sim 1.3$. However, at $z \sim 0.5$, they are much steeper, $\approx 0.2 \pm 0.06$.

The measurements of these slopes are robust. This is because we only consider radii of individual profiles where the S/N is >5 and only calculate a median profile if at least 10 galaxies contribute to it (Section 8.1). Furthermore, although the slopes we measure at higher redshift are shallow, as demonstrated in Section 8.2, we have the ability to measure steep slopes if present.

10.2. Differences between the First and Fifth Sets of Assumptions

Since there are significant differences between the sSFR profiles for the first and fifth sets of assumptions, they are compared here. A review and explanations of the differences between these sets is given. Since many studies make assumptions similar to those in the first set, findings from these works are also reproduced. In Figure 14, the sSFR profiles created under the first set are shown, and they are compared with those from the fifth, which are shown in Figure 13. Star-forming galaxies in the first set have significantly flatter profiles than those in the fifth (slopes of approximately 0.010 ± 0.003 versus 0.1 ± 0.01). Green valley galaxies for the two sets have similar profiles. Profiles of quiescent galaxies have significantly different slopes between the first and fifth sets. At $z \sim 0.5$, those in the first set are much steeper: approximately 0.5 ± 0.01 versus 0.2 ± 0.06. The case is similar at $z \sim 0.9$: about 0.2 ± 0.01 versus 0.06 ± 0.03. The difference goes away at $z \sim 1.3$, where the slopes are similar among both sets (0.04 ± 0.07 and 0.05 versus 0.01 ± 0.04–0.08 ± 0.05).

These differences arise from the way observed colors and physical properties relate to each other for the first and fifth sets of assumptions. Under the first set, sSFR does not change much along the color–color profiles of star-forming galaxies (second row in Figure 8). Therefore, star-forming galaxies have flat sSFR gradients. The sharp transition in the F435W − F775W color between low- and high-sSFR models causes quiescent galaxies to have sSFR profiles that rise quickly with radius. Profiles of green valley galaxies lie between these extremes. For the fifth set, sSFR varies along the color–color profiles of star-forming galaxies such that sSFR is lower in the centers and is higher in the outskirts. The F435W − F775W colors transition more smoothly between low- and high-sSFR models. As a result, quiescent galaxies have shallower profiles. Profiles of green valley galaxies are between these extremes.

Studies that adopt assumptions similar to those in the first set find shallow and steep slopes for the sSFR profiles of quiescent galaxies at stellar masses and redshifts similar to those examined in this paper. At $0.5 < z < 1.0$, F. S. Liu et al. (2018) found that quiescent galaxies have nearly flat sSFR profiles. In contrast, at $0.2 < z < 0.7$, L. Morselli et al. (2019) found steeply rising sSFR profiles for quiescent galaxies (slopes of ∼0.3–0.5). At intermediate redshifts of $0.7 < z < 1.5$, E. J. Nelson et al. (2021) found shallow slopes of ∼0.1 for the sSFR profiles galaxies below the SFMS. Similar slopes for the profiles of quiescent galaxies are obtained by Abdurro'uf & M. Akiyama (2018), who examined galaxies at $\log(M_\star/M_\odot) \geqslant 10.5$ and at $0.8 < z < 1.8$. However, steep slopes of ∼0.3–0.5 are found for the profiles of quiescent galaxies at $0.7 < z < 1.2$ by L. Morselli et al. (2019).

11. Galaxy Evolution under the Fifth Set of Assumptions

11.1. Evolution at Fixed Mass

We now do science with the sSFR profiles created under the fifth set of assumptions (Figure 13). We do so at a fixed mass, or under the simple assumption that galaxies do not gain enough mass with time to leave their respective mass ranges. We assume that with time, star-forming galaxies become green valley galaxies, and green valley galaxies become quiescent. Specifically, we assume that the star-forming galaxies at $z \sim 1.3$ and ~0.9 become green valley galaxies at $z \sim 0.9$ and $z \sim 0.5$, respectively. We assume that green valley galaxies at $z \sim 1.3$ and $z \sim 0.9$ become quiescent galaxies at $z \sim 0.9$ and $z \sim 0.5$, respectively. Finally, we assume that quiescent galaxies remain quiescent.

While the assumptions above are oversimplified, we validated some of them. We compared the SFHs of the green valley galaxies with those of quiescent galaxies at $z \sim 1.3$ and $z \sim 0.9$ and at $z \sim 0.9$ and $z \sim 0.5$ and find that they are consistent. We also find that the SFHs of quiescent galaxies at $z \sim 0.9$ and $z \sim 0.5$ overlap with those of quiescent galaxies at $z \sim 1.3$ and $z \sim 0.9$, respectively. Therefore, our assumptions that these populations are connected at fixed mass are valid. In Appendix D, we consider bins in mass that evolve with redshift and find quantitatively similar results to those presented here.

The median sSFR profiles of star-forming galaxies at $z \sim 1.3$ and those of green valley galaxies at $z \sim 0.9$ that we expect them to evolve into differ most significantly in normalization (by about 0.8 dex) but have similar slopes (approximately 0.08 ± 0.01 and 0.1 ± 0.02 dex kpc^{-1}, respectively). At $z \sim 0.5$, the median profiles differ in normalization and slope. The normalization decreases from the star-forming to green valley by about 0.8 dex, and the slopes become shallower by about 0.05.

At all redshifts, profiles of green valley galaxies have higher normalizations than those for quiescent galaxies by around 1 dex. Green valley galaxy profiles at $z \sim 1.3$ have slopes that are similar to those of quiescent galaxies at $z \sim 0.9$ (approximately 0.09 ± 0.02 and 0.07 ± 0.03, respectively). Because their slopes are similar and the most significant difference is in their normalizations, this suggests that, as green valley galaxies quench, they decline in sSFR at all radii at the same time. Therefore, if green valley galaxies at $z \sim 1.3$ evolve into quiescent galaxies at $z \sim 0.9$, they must quench at all radii at the same time.

Interestingly, at lower redshifts, the sSFR profiles of the quiescent galaxies are considerably steeper than all of the other profiles, with slopes of about 0.2 ± 0.06. Green valley galaxies at $z \sim 0.9$ have slopes of about 0.1 ± 0.01. Therefore, if green valley galaxies at $z \sim 0.9$ evolve into quiescent galaxies at $z \sim 0.5$, they must reduce star formation in their inner parts first. This is confirmed by examining the median SFHs of quiescent galaxies at $z \sim 0.5$. We find that the median SFH in the centers of these galaxies peaks and declines earlier than that in the outskirts. This is consistent with reducing SFR in their inner parts first.

11.2. Interpreting Our Findings

In this Section we compare our results under the fifth sets of assumptions to those from the literature to ours and discuss potential physical mechanisms for quenching galaxies in our sample. In the previous subsection, we find that in the median,
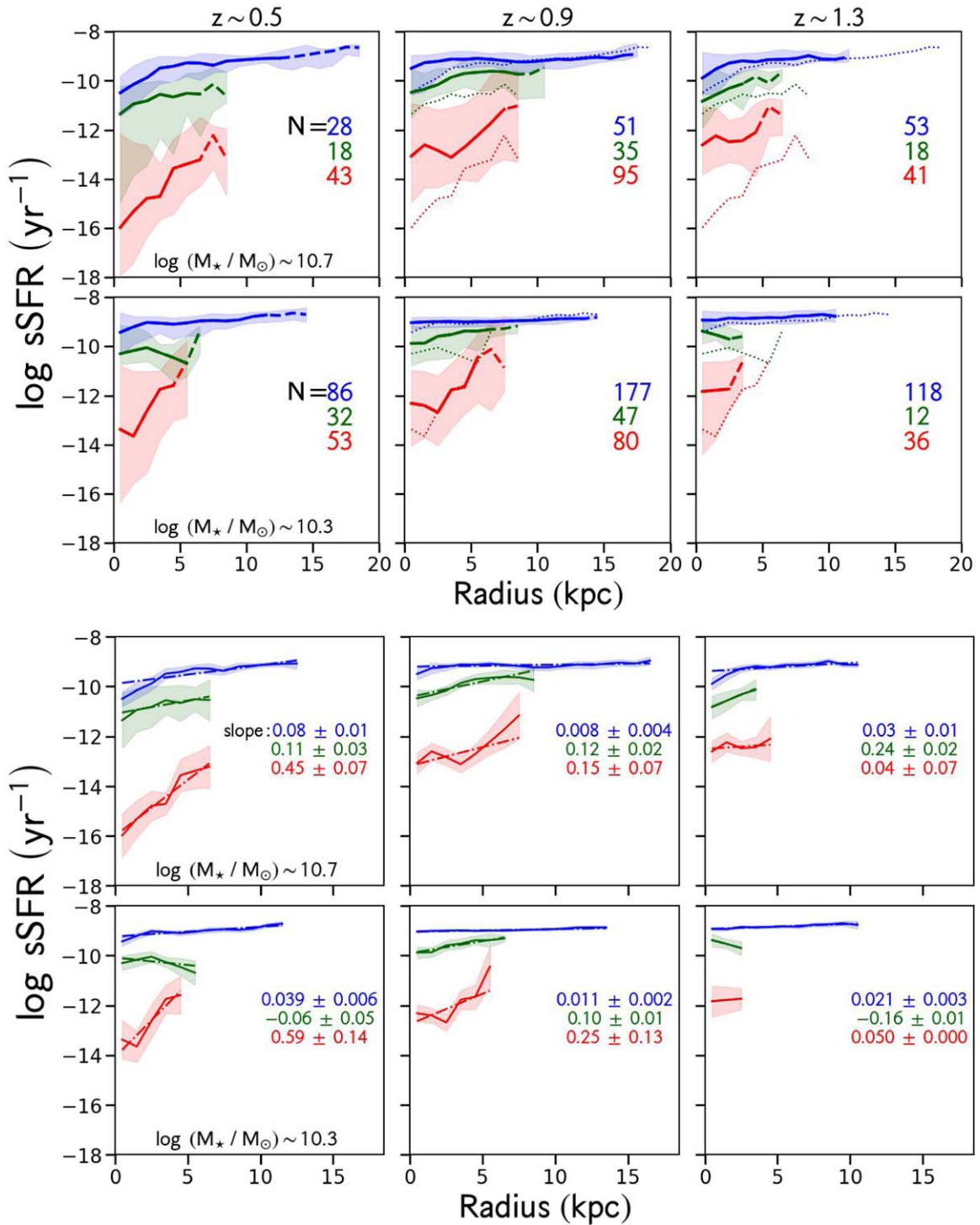
Figure 14. Median specific star formation rate profiles created under the first set of assumptions are shown. We expect green valley galaxies at $z \sim 1.3$ to evolve into quiescent galaxies at $z \sim 0.9$. Comparing these profiles, those of the quiescent galaxies are steeper. This is also the case for green valley galaxies at $z \sim 0.9$ and $z \sim 0.5$. This suggests inside-out quenching. Lines and shading have the same meaning as in Figure 13.

quenching occurs at all radii at the same time at $0.7 < z < 1.5$ and from the inside-out at $0.4 < z < 0.7$.

Quenching mechanisms that are consistent with inside-out quenching include compaction (A. Zolotov et al. 2015; S. Tacchella et al. 2016), quenching due to AGNs (S. F. Sánchez et al. 2018, and references therein; D. Nelson et al. 2019; S. Appleby et al. 2020; E. J. Nelson et al. 2021), and morphological quenching (M. Martig et al. 2009;

R. Genzel et al. 2014). A decline in the gas accretion at all radii would be consistent with quenching at all radii at the same time.

Physical processes that quench galaxies from the outside-in are not consistent with our observations in the median. Such processes include ram pressure stripping (e.g., M. Fossati et al. 2018; W. J. Cramer et al. 2019), though this process is expected to occur in dense environments, e.g., galaxy clusters.

Gas-rich mergers, which are believed to enhance star formation in the center and suppress star formation in the outskirts (J. C. Mihos & L. Hernquist 1996; G. F. Snyder et al. 2011; J. K. Barrera-Ballesteros et al. 2015; J. Moreno et al. 2015; M. D. Thorp et al. 2019; J. L. Steffen et al. 2021), would also be inconsistent with our findings in the median.

Gas-poor mergers could explain some of the evolution observed under the fifth set of assumptions. Mass-weighted age profiles are observed to progressively flatten as galaxies transition from star-forming to green valley to quiescent, as seen in Figure 7 and Appendix C. Gas-poor mergers are known to flatten age gradients (e.g., S. D. M. White 1979, 1980; K. Bekki & Y. Shioya 1998, 1999; R. L. C. Ogando et al. 2005; P. F. Hopkins et al. 2009; C. Tortora et al. 2010; M. Hirschmann et al. 2015). Studies that have measured merger rates find that the number density evolution of high-mass ($M_\star \geqslant 10^{10.5} M_\odot$) quiescent galaxies at $z < 1$ can be accounted for by major mergers of star-forming galaxies (e.g., E. F. Bell et al. 2006; A. R. Robaina et al. 2010; G. B. Brammer et al. 2011; A. W. S. Man et al. 2012; A. W. S. Man et al. 2016; though see J. Moustakas et al. 2013). However, it is unclear whether there are enough major mergers at low redshift to build up the quiescent galaxy population observed at $z = 0$ at lower masses (e.g., T. Weinzirl et al. 2009; A. K. Weigel et al. 2017; F. Rodrìguez Montero et al. 2019).

Another mechanism that can flatten age gradients is one where the orbits of stars in galaxies change in radius with time, regardless of the merger history. In disk galaxies, this process occurs due to perturbations to their galactic potentials and is known as radial migration (e.g., D. Lynden-Bell & A. J. Kalnajs 1972; J. A. Sellwood & J. J. Binney 2002). While some studies find that radial migration significantly influences the radial gradients of stellar populations (e.g., R. Roškar et al. 2008; R. Schönrich & J. Binney 2009; T. Buck 2020), others do not (e.g., I. Minchev et al. 2014; R. J. J. Grand et al. 2015; R. J. J. Grand & D. Kawata 2016; V. Avila-Reese et al. 2018). Integral field unit observations of $z \sim 0$ spiral galaxies show that radial migration appears to have had minor effects on their growth in size and mass over the last 10 Gyr (T. Peterken et al. 2020). We conclude that radial migration does not contribute significantly to our results.

12. Summary and Conclusions

We use multiband HST images from the optical through NIR to measure radial flux profiles of 1440 galaxies with stellar masses $10 \leqslant \log (M_\star/M_\odot) \leqslant 11.5$ over redshifts $0.4 < z < 1.5$. We fit the resulting broadband SEDs at each radius in these profiles using the BEAGLE tool. We then examine the resulting profiles of sSFR, SFR surface density, stellar mass surface density, attenuation in the rest-frame V band, A_V, and mass-weighted age. We do so as function of galaxy stellar mass and redshift. This has been done by other studies (e.g., E. J. Nelson et al. 2016, 2021; W. Wang et al. 2017; Abdurro'uf & M. Akiyama 2018; F. S. Liu et al. 2018; L. Morselli et al. 2019), and we revisit it to examine the effects of adopting more physically motivated assumptions in the fitting of the SEDs.

In an ideal world, priors used in SED fits are uninformative, and data are highly constraining. However, this is rarely the reality. When this is the case, we suggest an iterative approach. We start with priors that are minimally informative and compare the models created with these priors with data in color–color space. Then, to optimize the overlap of models with data, priors are edited in a physically meaningful way. We use this technique to develop five sets of SED-fitting assumptions that build upon each other.

We first consider assumptions that are commonly used in the literature, namely, a dust law with a fixed slope and uniform priors on all free parameters in the SED fits (e.g., S. Wuyts et al. 2012; S. Hemmati et al. 2014, 2020; A. Cibinel et al. 2015; T. Morishita et al. 2015; M. Mosleh et al. 2017, 2020; Abdurro'uf & M. Akiyama 2018; Y. Guo et al. 2018; R. Sorba & M. Sawicki 2018; L. Morselli et al. 2019; K. A. Suess et al. 2019). Then, we examine the cumulative effects of a number of changes that are based on studies that examine individual components of the SED fits. These changes are described below. To do so, we gradually incorporate them into the SED fits by defining five sets of SED-fitting assumptions (Section 6 and Table 2).

12.1. The Five Sets of SED-fitting Assumptions

The first set of assumptions, which is commonly used in the literature, consists of a single dust law and uniform priors on all parameters, including optical depth, log of the star formation history timescale, log age, and log metallicity.

For the second set of assumptions, we make a significant change and adopt the flexible dust law developed by J. Chevallard et al. (2013). A flexible dust law encapsulates the variety of dust laws found for galaxies in the nearby Universe (V. Wild et al. 2011; A. J. Battisti et al. 2017; S. Salim et al. 2018) and at intermediate redshift (M. Kriek & C. Conroy 2013; B. Salmon et al. 2016; I. Barišić et al. 2020).

For the third set of assumptions, we add to the second set an exponential prior on the effective optical depth in the rest-frame V band, $\hat{\tau}_V$. This is also a significant change. It ensures that models with little to no dust ($A_V \sim 0$ mag) are more probable than models with a lot of dust ($A_V \gtrsim 2$ mag). We make this change because the distribution of dust attenuation values of galaxies in the nearby Universe is approximately exponential (J. Brinchmann et al. 2004). We expect it to be similar at the redshifts studied in this paper because the correlation between mass and dust and the shape of the mass function do not change significantly over $0 < z < 1.5$ (see T. Garn & P. N. Best 2010; A. Domìnguez et al. 2013; I. G. Momcheva et al. 2013; R. Ramraj et al. 2017 and A. Muzzin et al. 2013; I. Davidzon et al. 2017, respectively).

For the fourth set, we incorporate a Gaussian prior on the log of the SFH timescale, which allows for extended star formation histories. This change is made because studies that adopt nonparametric SFHs find that massive quiescent galaxies at $z \sim 1$ peak approximately 1–2 Gyr after they begin forming stars (C. Pacifici et al. 2016). This change ensures that quiescent galaxies can have star formation histories that peak about 1 Gyr after they begin forming stars. When adopting a uniform prior, as done by other studies, star formation histories tend to peak much earlier, typically 200–300 Myr after stars begin to form. This change is significant for quiescent galaxies and relevant for our results on quenching.

For the fifth set of assumptions, broad Gaussian priors to log age and log metallicity are applied. This is done to be consistent with studies that have determined ages and metallicities of galaxies at $z \sim 1$ via spectroscopy (R. Maiolino et al. 2008; N. P. Hathi et al. 2009; A. Henry et al. 2013; A. Gallazzi et al. 2014; M. Onodera et al. 2015; Y. Guo et al. 2016a; V. Estrada-Carpenter et al. 2019; R. Maiolino & F. Mannucci 2019).

These changes cause minor differences in the results between the fourth and fifth sets of assumptions.

12.2. Choosing a Set of Assumptions

We perform five complementary tests to determine which set of assumptions is most appropriate for our sample. In three of the tests, the fifth set performs the best. In two of them, the third, fourth, and fifth sets perform equally well.

As a first test, model colors are compared with observed integrated colors (Figure 5). Appropriate priors result in model colors that overlap with the observed colors. This overlap is quantified by calculating the fraction of models that lie within a rectangular region that contains 90% of the observations (Section 6.1). For the first set, only about 50% of the models lie in this region. For the second set, the fraction rises to 83%. From the third to the fifth sets, the fraction continues to rise to 93%. Therefore, the fifth set is the most appropriate for this test.

Second, we compare the Bayesian evidence of the fifth set of assumptions with that of the other sets for SED fits to the spatially integrated fluxes (see Figure 9 and Section 9.1). The fifth set is preferred to the first and marginally preferred to the second. It is not preferred over the third or the fourth.

Third, SFR surface density profiles of quiescent galaxies at $z \sim 0.5$ are compared with those measured from spectroscopy at $z \sim 0$ (see Figure 10 and Section 9.2.1). Justifications for doing this are provided in Section 9.2.3. Profiles for the fifth set agree the best, and those for the fourth set perform marginally worse than the fifth.

Fourth, A_V profiles of star-forming galaxies at $z \sim 0.5$ are compared with those measured from spectroscopy at $z \sim 0$ (Figure 11 and Section 9.2.2). Profiles for the fifth set agree the best.

For the fifth test, the behavior of A_V profiles of star-forming galaxies is examined as a function of galaxy inclination (Figure 12 and Section 9.3). Profiles for the third through fifth sets demonstrate the expected behavior, namely, they steepen in their centers as inclination increases, and are therefore preferred for this test.

12.3. Evolution of the sSFR Profiles under the Fifth Set of Assumptions

The median sSFR profiles created under the fifth set are examined to determine their evolution with redshift. This is done by comparing profiles at a fixed mass. The green valley galaxies at $z \sim 1.3$ are assumed to evolve into quiescent galaxies at $z \sim 0.9$. The median profiles of these green valley and quiescent galaxies each have different normalizations but have similar slopes. Therefore, the sSFR profiles simply decline in normalization with time, quenching at all radii at the same time. The green valley galaxies at $z \sim 0.9$ are assumed to evolve into quiescent galaxies at $z \sim 0.5$. The median profiles of these green valley and quiescent galaxies each have different normalizations and slopes, with those of the latter being steeper. Therefore, as galaxies quench, sSFR decreases more in their centers than in their outskirts. They quench from the inside-out.

In summary, we conclude that galaxies quench at all radii at the same time over $z \sim 1.3$ to $z \sim 0.9$ and from the inside-out over $z \sim 0.9$ to $z \sim 0.5$.

Other studies generally find inside-out quenching at all redshifts considered in this paper. This is because assumptions similar to those in the first set, primarily a fixed dust law, are assumed. Under a fixed dust law, profiles of quiescent galaxies are steep due to a sharp transition in model colors, which results in profiles that change abruptly in the outskirts (Section 8.2 and Figure 8). Under the fifth set, the transition in color is generally smoother than under the first. However, at $z \sim 0.5$, colors transition more sharply than they do at $z \sim 0.9$ and at $z \sim 1.3$. This results in steeper sSFR profiles of quiescent galaxies in this set at $z \sim 0.5$ than at higher redshifts. Consequently, galaxies quench from the inside-out under both the first and fifth sets at $z \sim 0.5$.

Appendix A
The Effects of Changing the Priors on the Star formation Histories

Priors on the SFH are adjusted in the fourth and fifth sets following studies based on spectroscopy (Sections 6.4 and 6.5). As a result, extreme SFHs, i.e., those that rise or decline sharply with time, occur less often in these sets than in the first. Changing the range on log τ alone has the most significant effect: it reduces the frequency of extreme SFHs. Changing the range on log age alone has minor effects. Changing the prior distributions from uniform to Gaussian also has minor effects, as the Gaussian priors are broad.
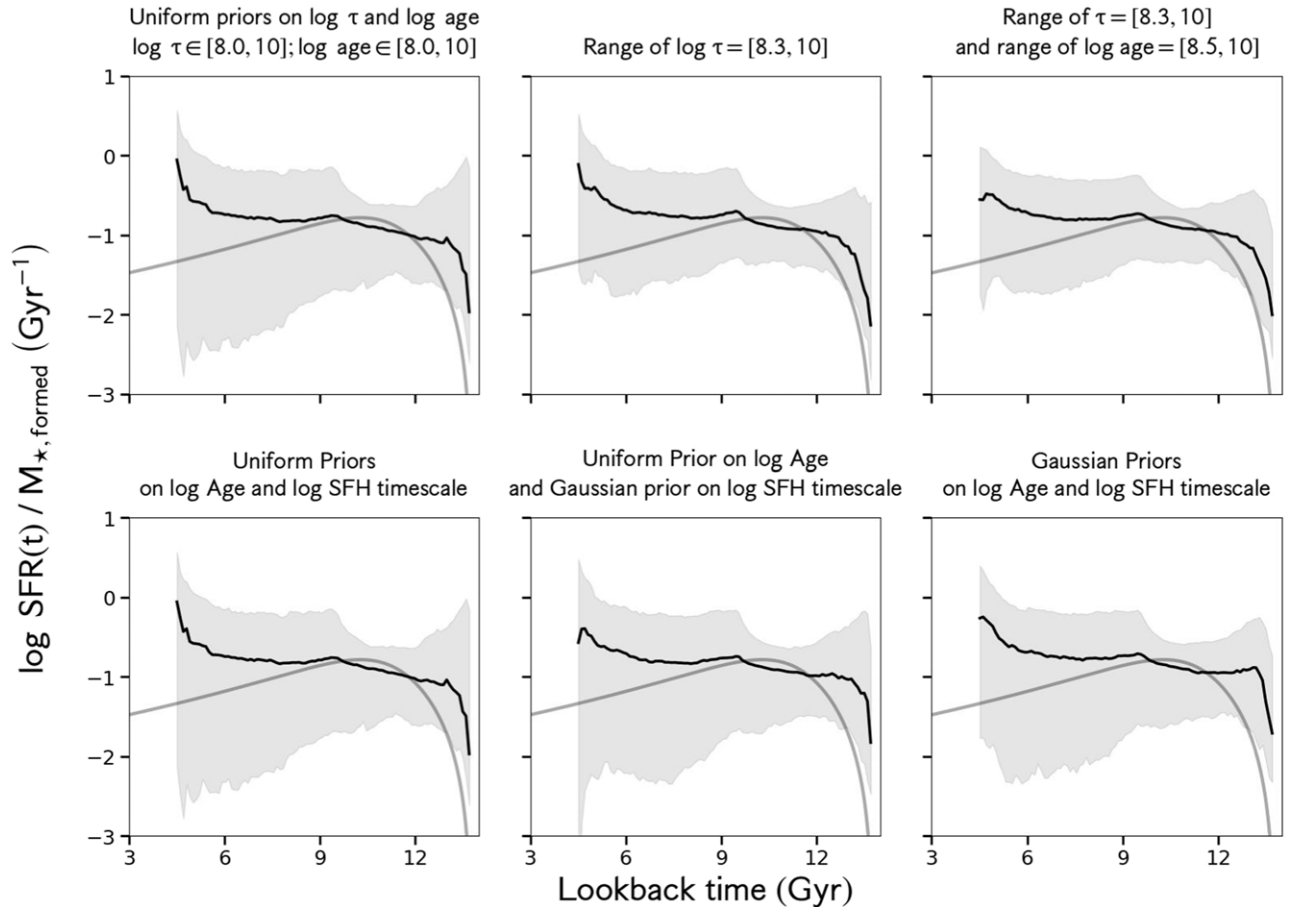
Figure 15. Comparison between the P. Madau & M. Dickinson (2014) cosmic star formation rate density (dark-gray line) and median SFHs of model galaxies for two cases: one where only the ranges on the log SFH timescale and log age change (top row) and another where only the priors distributions on these parameters change (bottom row). Median SFHs shown as black solid lines and the 16th–84th percentile ranges are plotted as gray shaded regions. Narrowing the range on log τ has the most significant effect (top-middle panel). Doing so down-weights the probability for models with extreme SFHs, i.e., those that sharply rise or decline with time. Adjusting the range on log age and changing prior distributions from uniform to Gaussian have minor effects. In all cases, model SFHs tend to rise at late times, in contrast with the SFRD. This is because the priors are constructed such that young, star-forming galaxies are abundant at all redshifts. This achieves the highest overlap between observed and model colors and results in model sSFRs that are high in the median at all redshifts.

In Figure 15, we show median SFHs and the 16th–84th percentile ranges of 10,000 model SFHs for two cases: one where only the range on log τ and log age is each adjusted, and another where only the prior on each parameter is changed. Each SFH is randomly drawn from the priors and must end at a redshift between $z = 0.4$ and $z = 1.5$. The shapes of the model SFHs are compared with that of the cosmic star formation rate density (SFRD), measured by P. Madau & M. Dickinson (2014), which is repeated in all panels in Figure 15. Following A. C. Carnall et al. (2019), we show the cosmic SFRD divided by the integral of the cosmic SFRD over time.

In all cases, the median SFH rises quickly in the first ~Gyr after the Big Bang and rises gradually as lookback time decreases. The median SFH rises at late times, in contrast with the SFRD, because the priors are set such that young, star-forming galaxies are abundant at all redshifts. This is done to achieve the highest overlap between observed and model colors. Therefore, the model SFHs have high sSFRs in the median at all redshifts, which contrasts with that of the SFRD. For the priors under the first set, shown in the top-left panel of Figure 15, the 16th–84th percentile range grows with time such that it spans ~3 dex by $z = 0.4$. This is because of the wide range ([8.0, 10.0]) on the log SFH timescale, τ. When narrowing the range to [8.3, 10.0] (top-middle panel), the percentile range is smaller (1.5 dex at $z = 0.4$).

Narrowing the range on log age from [8.0, 10] to [8.5, 10] (top-right panel) has minor effects. Modifying the priors from uniform to Gaussian (bottom row) also has minor effects. This is because the Gaussian priors are wide.

Appendix B
Color–Color Tracks for Each Set of Assumptions

We show median color–color tracks of star-forming, green valley, and quiescent galaxies defined under each set of assumptions in Figure 16 as blue, green, and red lines, respectively. Color–color tracks in each redshift bin are shown in different rows: $z \sim 0.5$ in the top row, $z \sim 0.9$ in the middle, and $z \sim 1.3$ in the bottom. All galaxies used to create these median profiles have stellar masses $10 < \log (M_\star/M_\odot) < 10.5$.

The median color–color tracks for all sets of assumptions are in good agreement. The greatest discrepancy between any set of color–color tracks is that seen for star-forming galaxies at $z \sim 0.5$ between the first and third sets, shown as the light-blue circle and dark-blue star, respectively, in the top row, middle column. The central median F435W − F775W colors disagree by 0.3 mag. However, the dispersion about each of these central colors is ~0.4 mag. Therefore, this discrepancy is not significant.
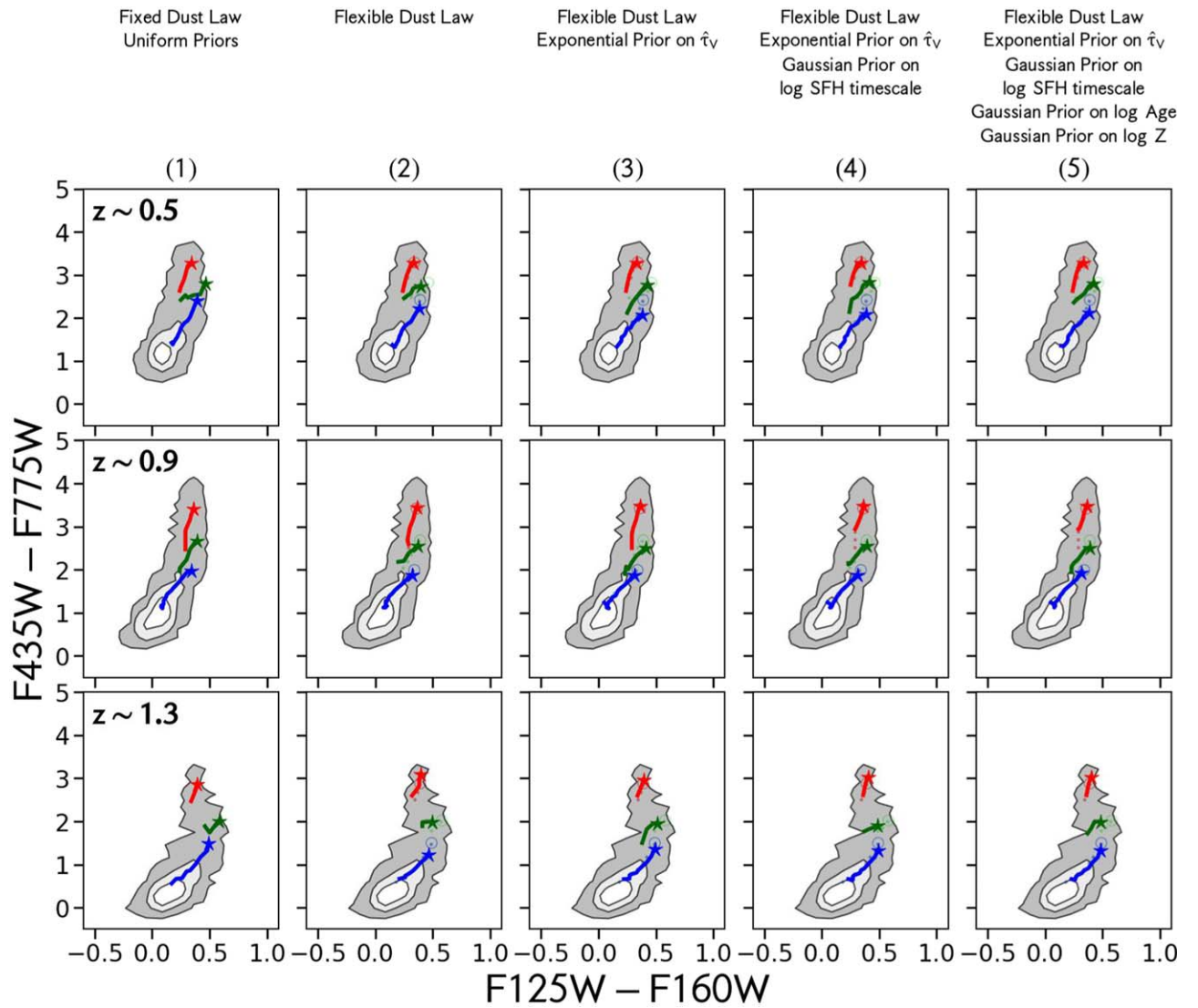
Figure 16. The median color–color tracks for galaxies that have stellar masses $10 < \log(M_\star/M_\odot) < 10.5$ are shown here for all sets of assumptions. The definition of star-forming, green valley, and quiescent varies according to the set of assumptions used. Reassuringly, the color–color tracks defined under each set are consistent with each other. The median central colors are shown as stars. Tracks for galaxies defined under the first set of assumptions are repeated in the second through fifth columns for comparison. They are shown as faint dotted lines, and their central colors are shown as empty circles.

Appendix C
Science Profiles under All Sets of Assumptions

In this Appendix, we show science profiles under all sets of assumptions for all mass and redshift bins. For the first set of assumptions, its mass-weighted age and sSFR profiles are shown in Figure 17, the SFR and stellar mass surface density profiles are shown in Figure 18, and A_V profiles are shown in Figure 19. The same format is repeated for the second, (Figures 20–22), third (Figures 23–25), fourth (Figures 26–28), and fifth (Figures 29–31) sets.
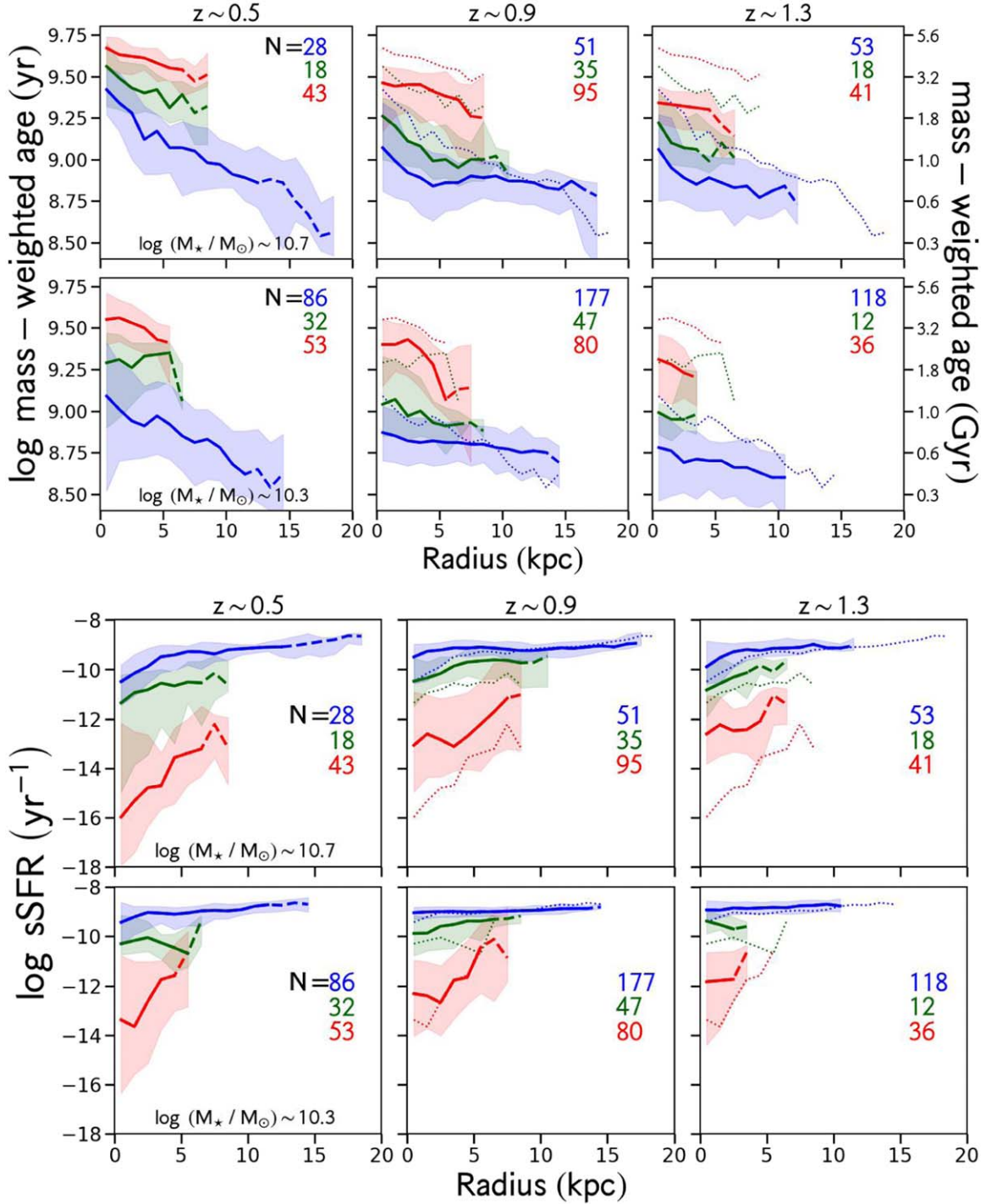
Figure 17. Median science profiles of mass-weighted age (top) and sSFR (bottom) created under the first set of assumptions for all mass and redshift bins are shown. In each panel, the meanings of the lines, shadings, and colors are the same as those in the top two rows in Figure 13.
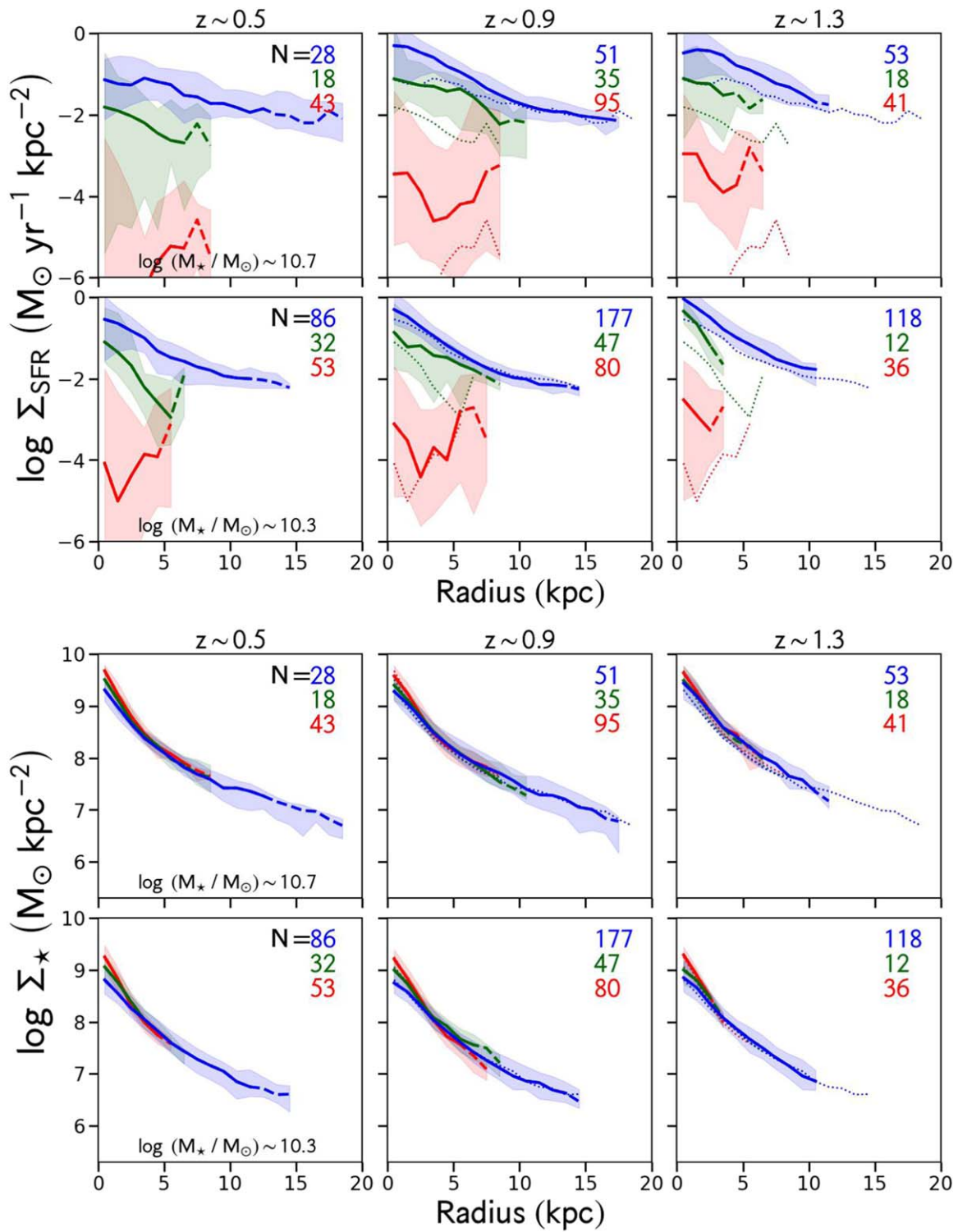
Figure 18. Median science profiles of SFR surface density (top) and stellar mass surface density (bottom) under the first set of assumptions for all mass and redshift bins are shown. In each panel, the meanings of the lines, shadings, and colors are the same as those in the top two rows in Figure 13.
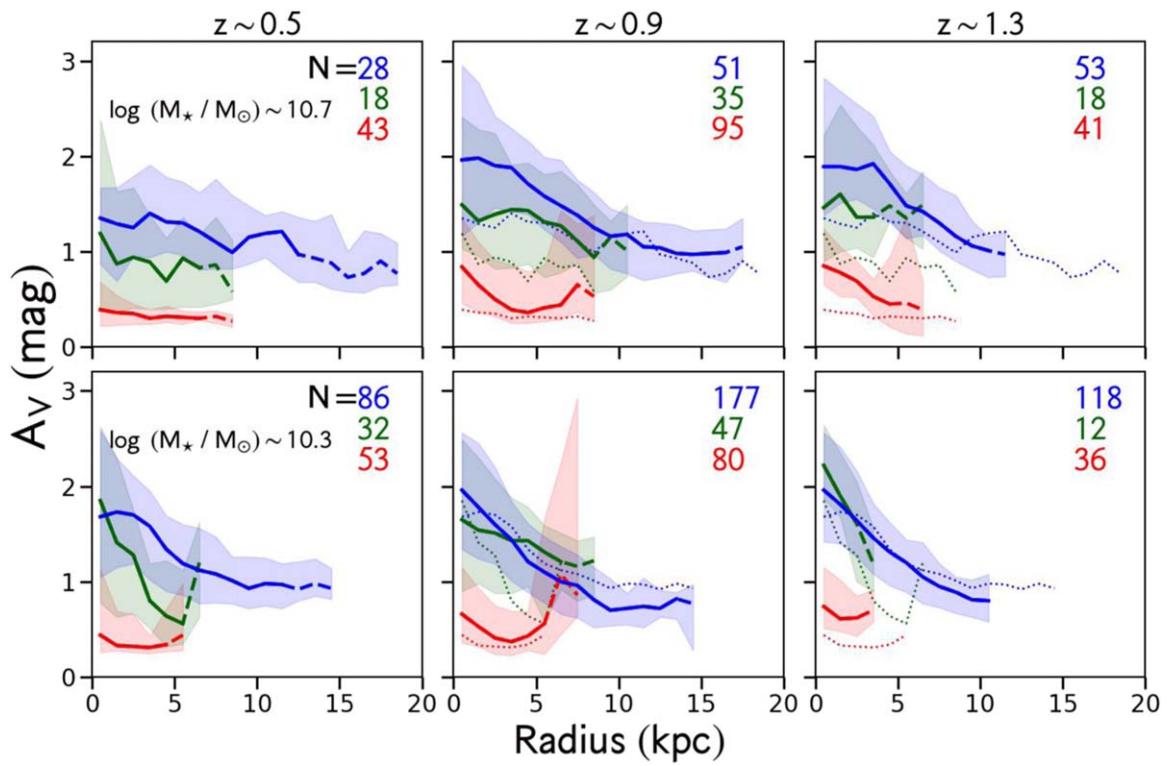
Figure 19. Median science profiles of A_V under the first set of assumptions for all mass and redshift bins are shown. In each panel, the meanings of the lines, shadings, and colors are the same as those in the top two rows in Figure 13.
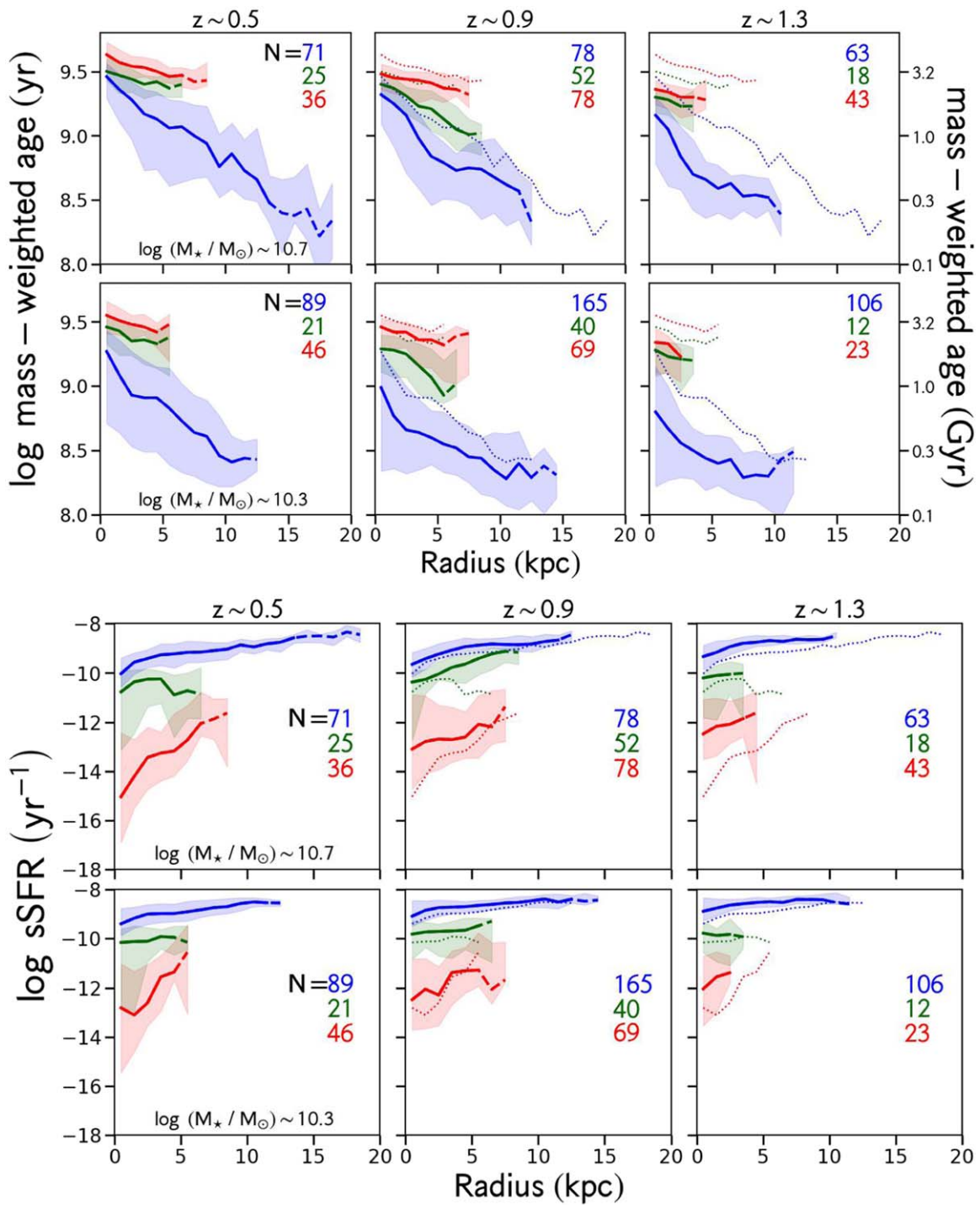
Figure 20. Median science profiles of mass-weighted age (top) and sSFR (bottom) under the second set of assumptions for all mass and redshift bins are shown. In each panel, the meanings of the lines, shadings, and colors are the same as those in the top two rows in Figure 13.
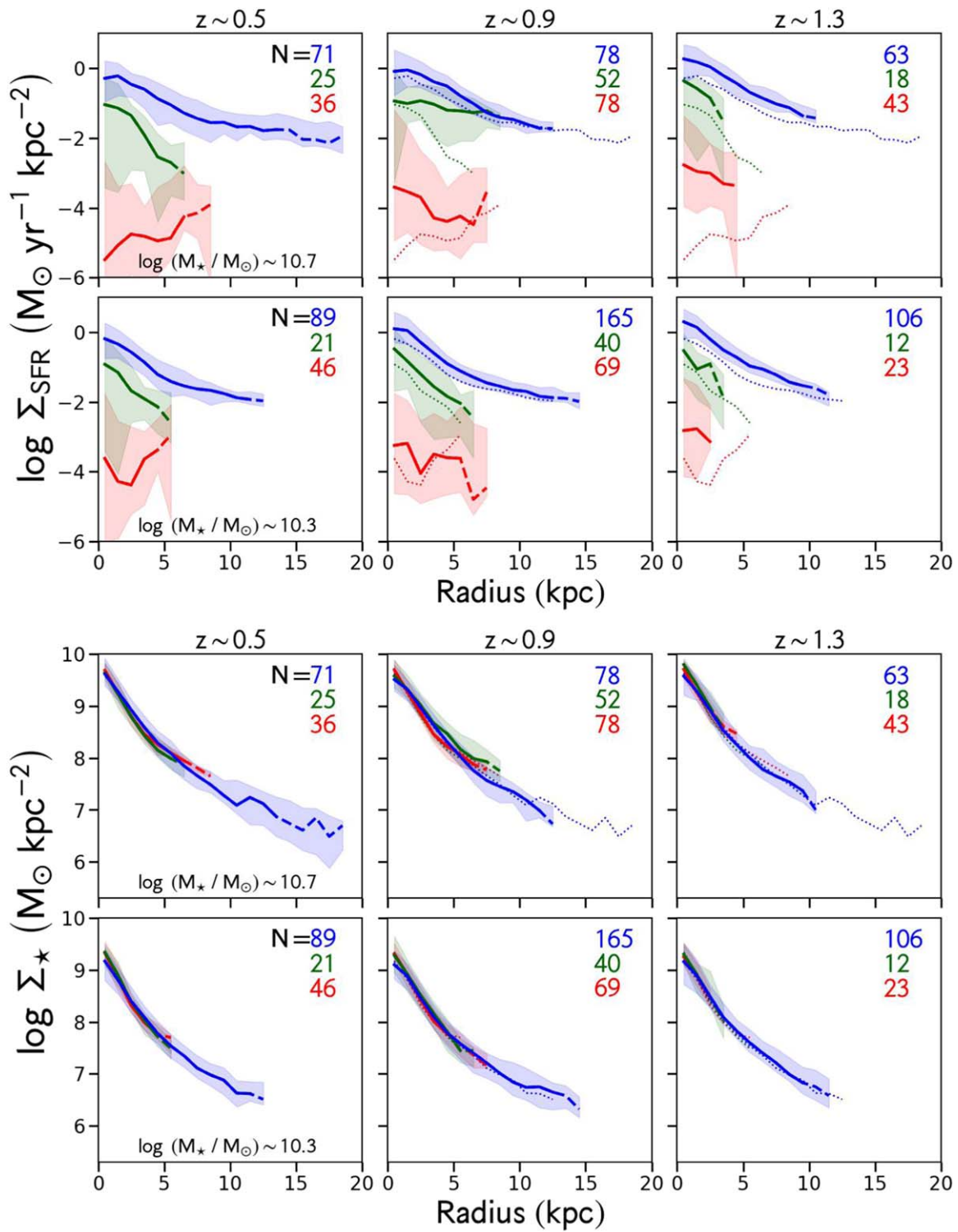
Figure 21. Median science profiles of SFR surface density (top) and stellar mass surface density (bottom) under the second set of assumptions for all mass and redshift bins are shown. In each panel, the meanings of the lines, shadings, and colors are the same as those in the top two rows in Figure 13.
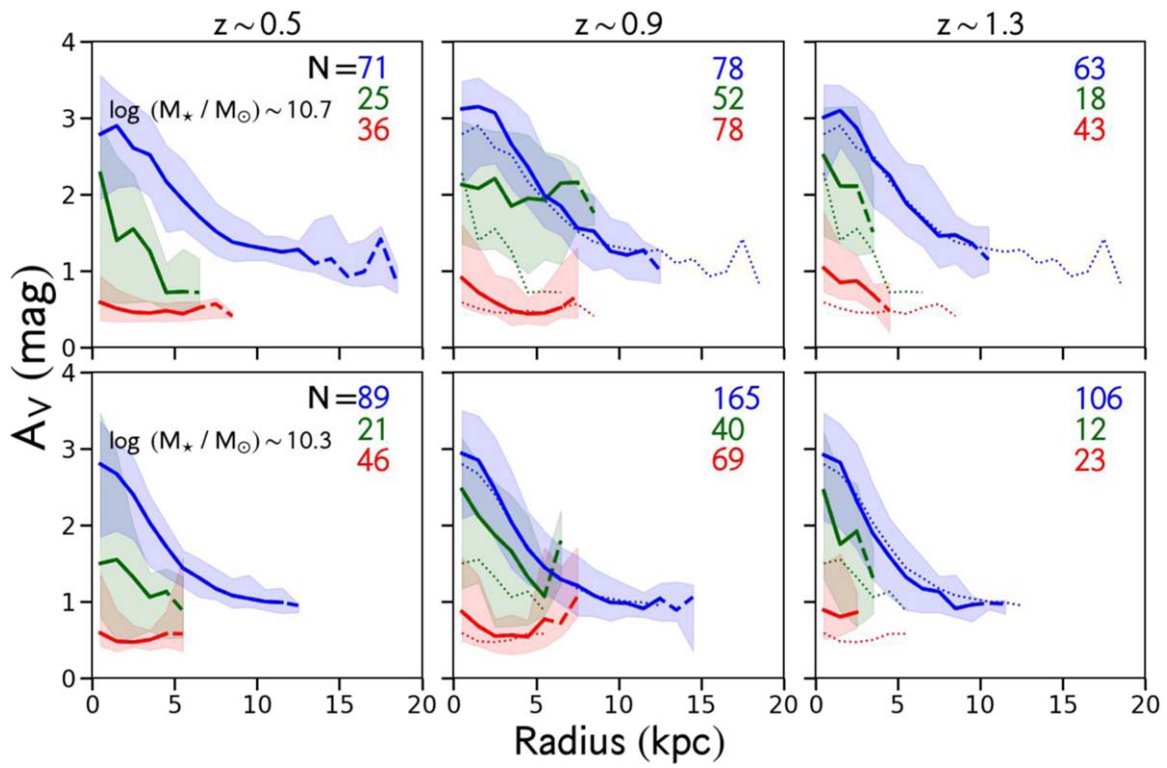
Figure 22. Median science profiles of A_V under the second set of assumptions for all mass and redshift bins are shown. In each panel, the meanings of the lines, shadings, and colors are the same as those in the top two rows in Figure 13.
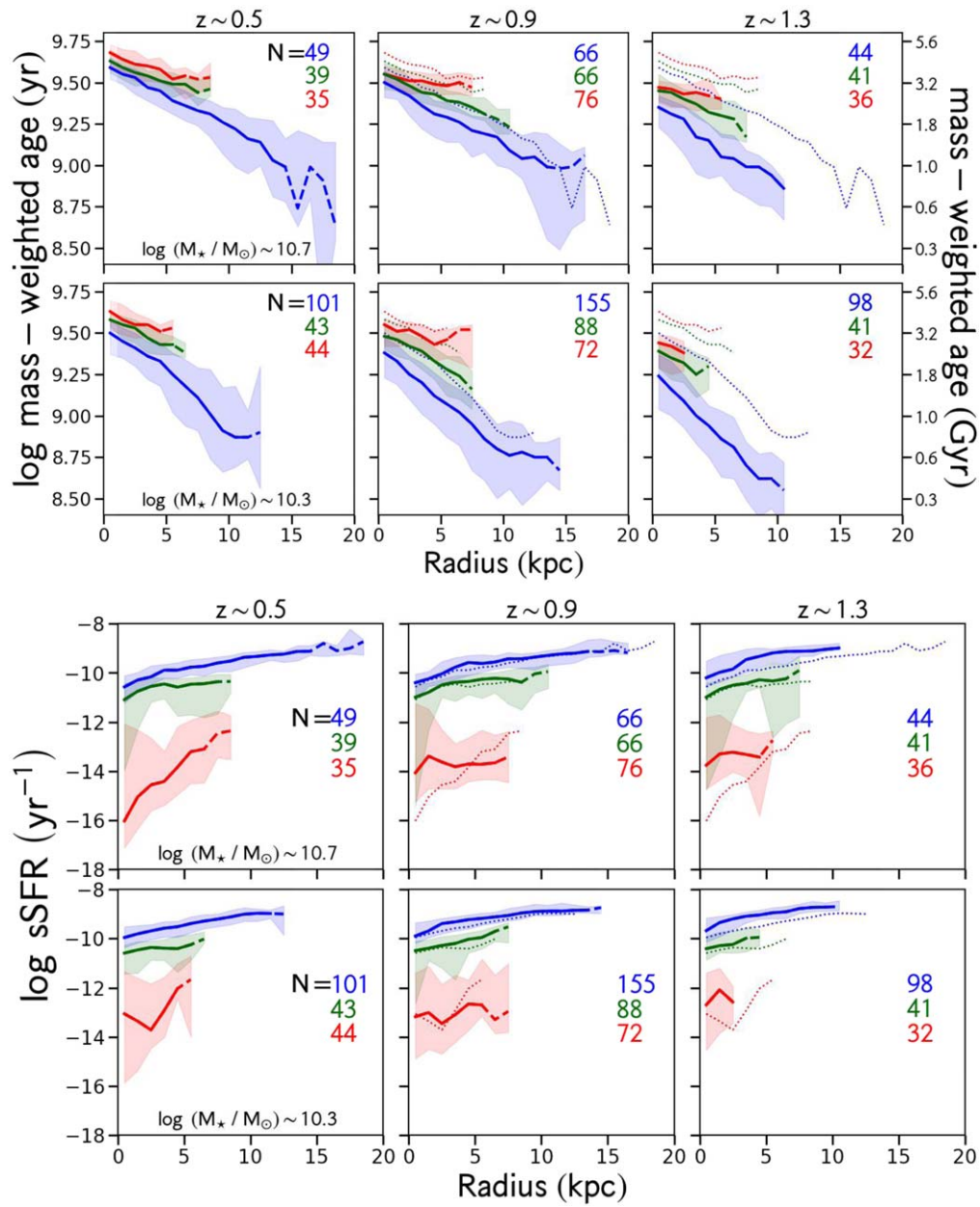
Figure 23. Median science profiles of mass-weighted age (top) and sSFR (bottom) under the third set of assumptions for all mass and redshift bins are shown. In each panel, the meanings of the lines, shadings, and colors are the same as those in the top two rows in Figure 13.
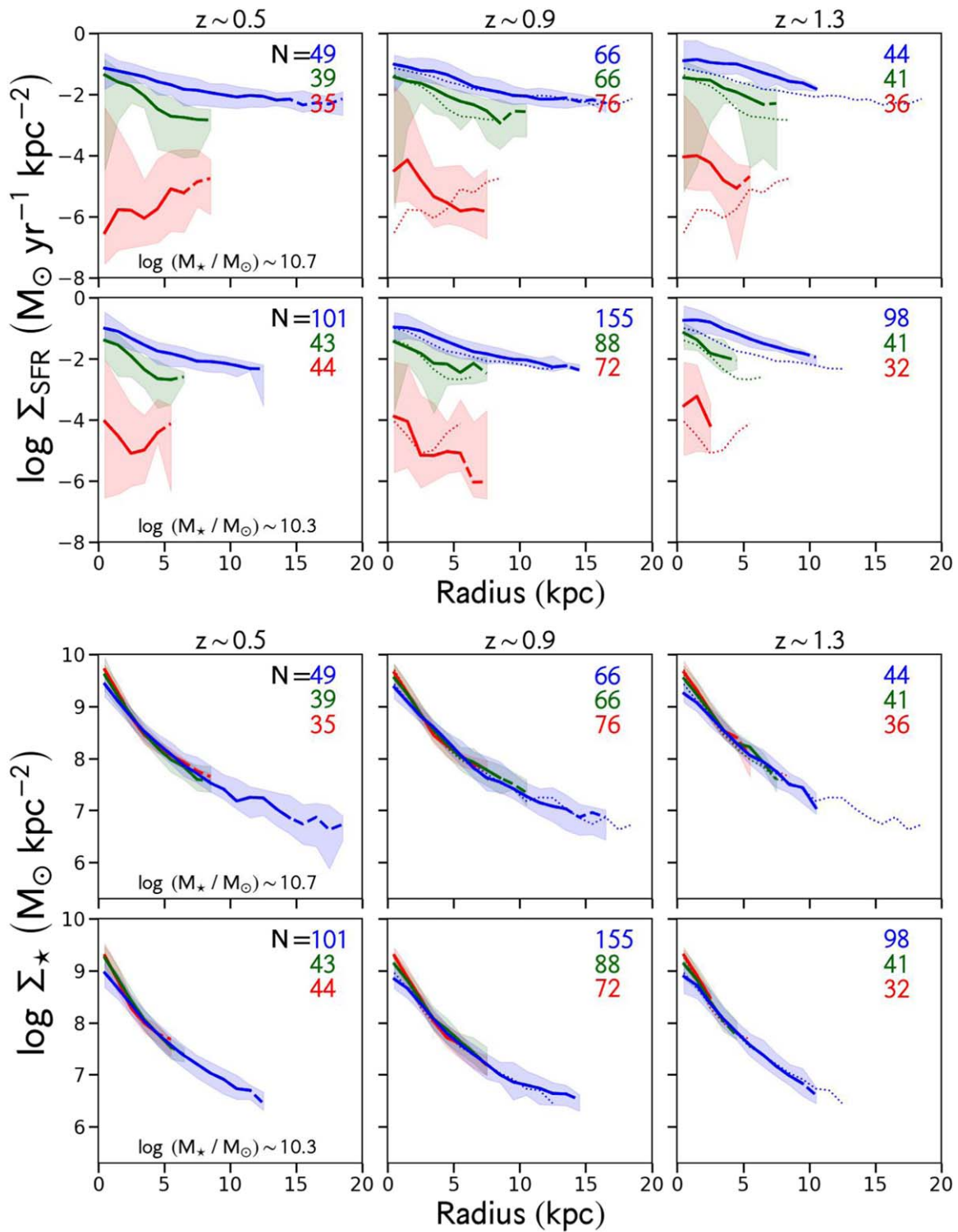
Figure 24. Median science profiles of SFR surface density (top) and stellar mass surface density (bottom) under the third set of assumptions for all mass and redshift bins are shown. In each panel, the meanings of the lines, shadings, and colors are the same as those in the top two rows in Figure 13.
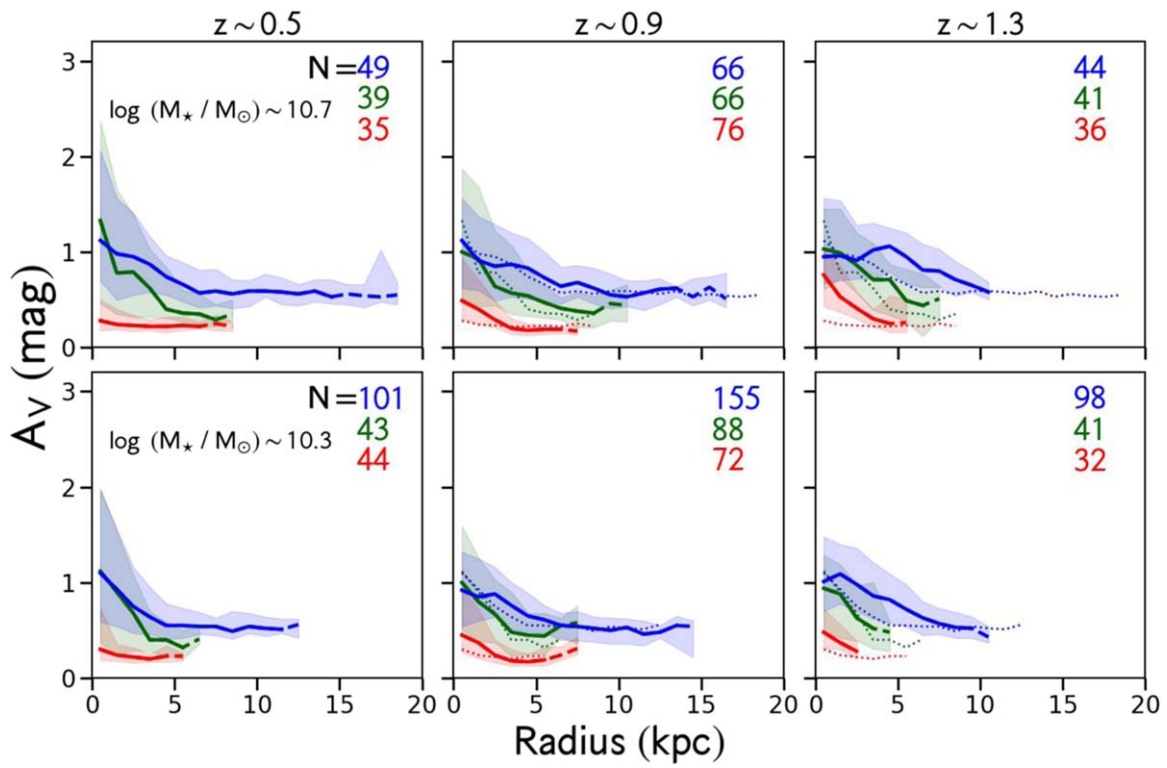
Figure 25. Median science profiles of A_V under the third set of assumptions for all mass and redshift bins are shown. In each panel, the meanings of the lines, shadings, and colors are the same as those in the top two rows in Figure 13.
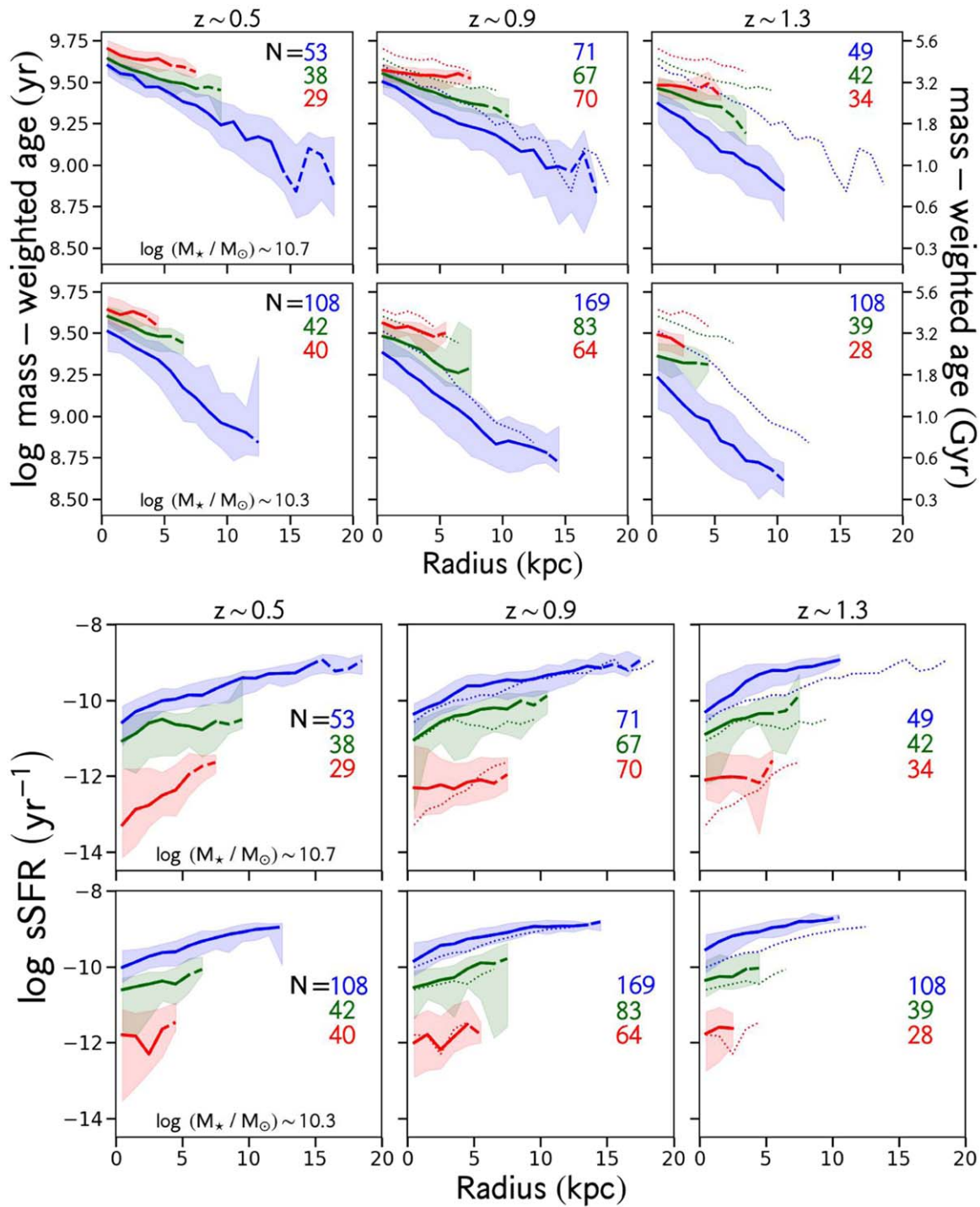
Figure 26. Median science profiles of mass-weighted age (top) and sSFR (bottom) under the fourth set of assumptions for all mass and redshift bins are shown. In each panel, the meanings of the lines, shadings, and colors are the same as those in the top two rows in Figure 13.
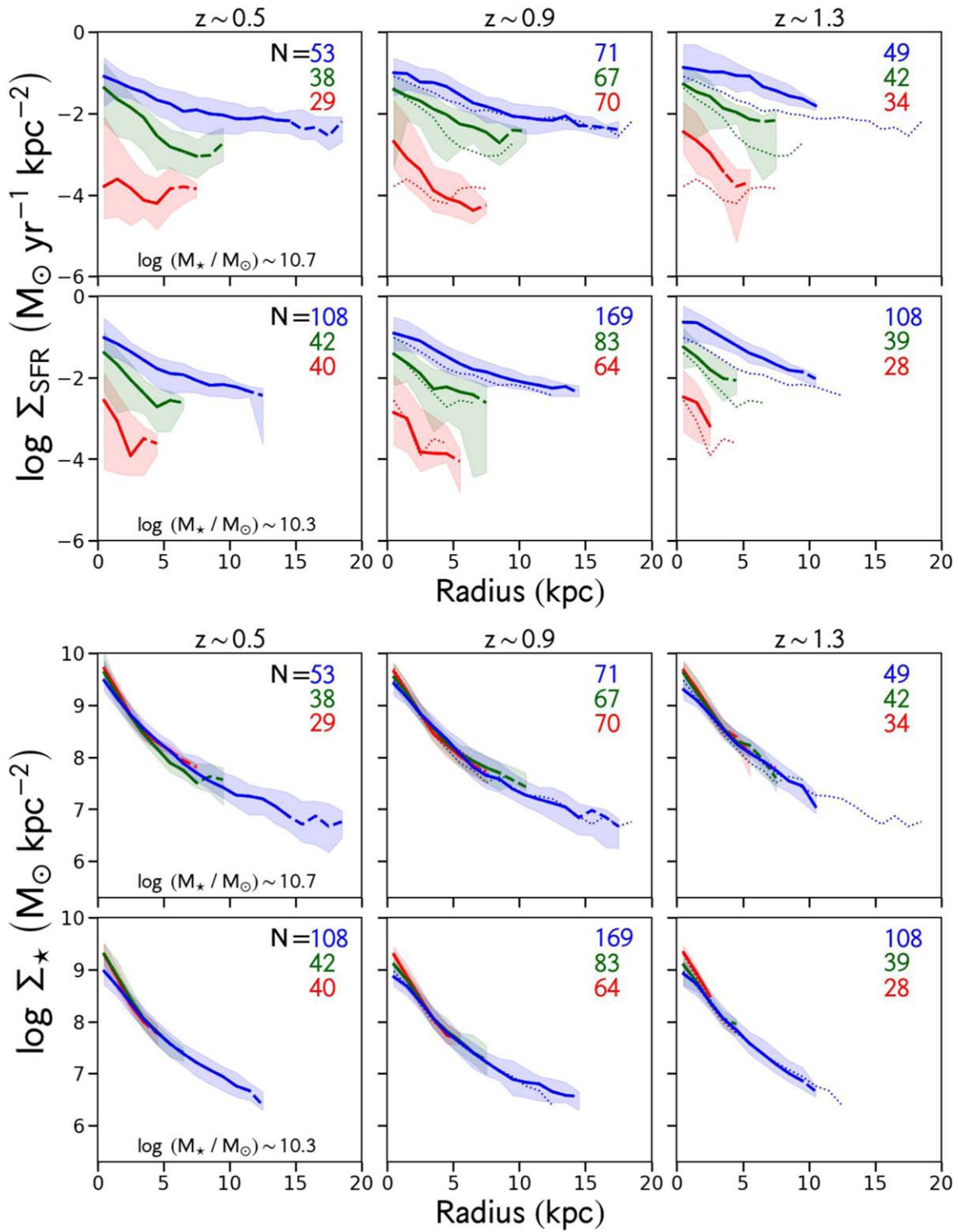
Figure 27. Median science profiles of SFR surface density (top) and stellar mass surface density (bottom) under the fourth set of assumptions for all mass and redshift bins are shown. In each panel, the meanings of the lines, shadings, and colors are the same as those in the top two rows in Figure 13.
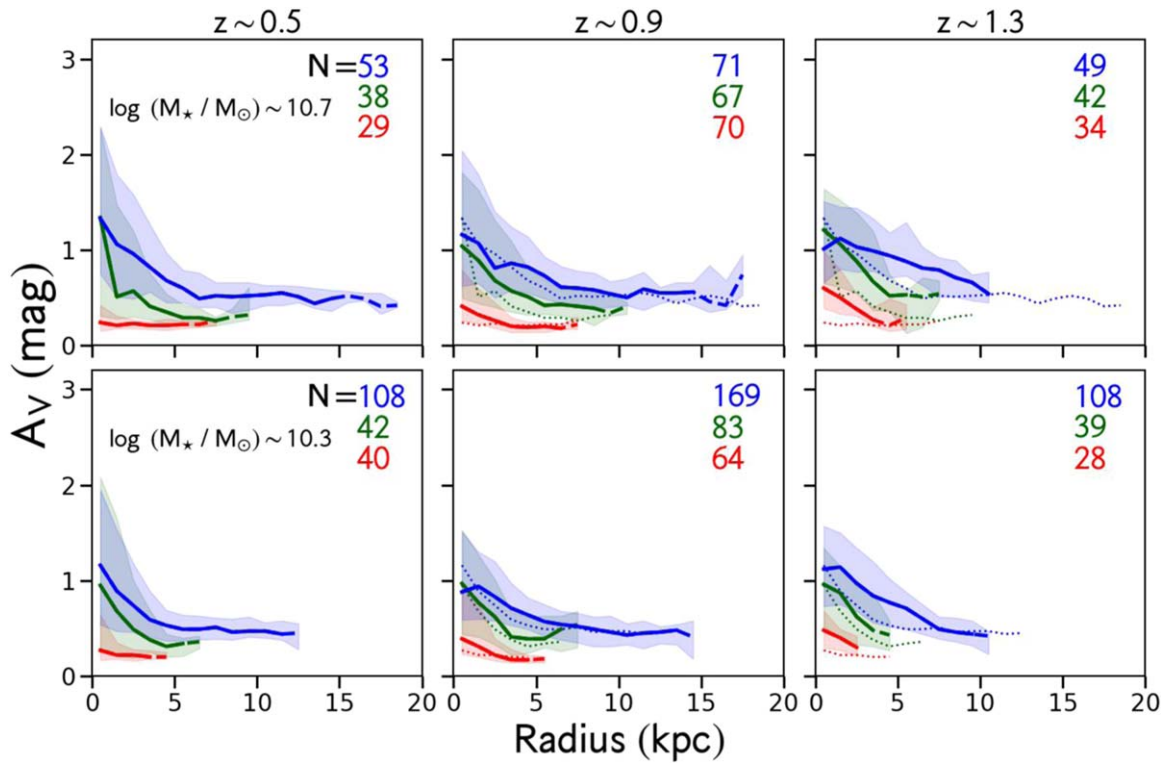
Figure 28. Median science profiles of A_V under the fourth set of assumptions for all mass and redshift bins are shown. In each panel, the meanings of the lines, shadings, and colors are the same as those in the top two rows in Figure 13.
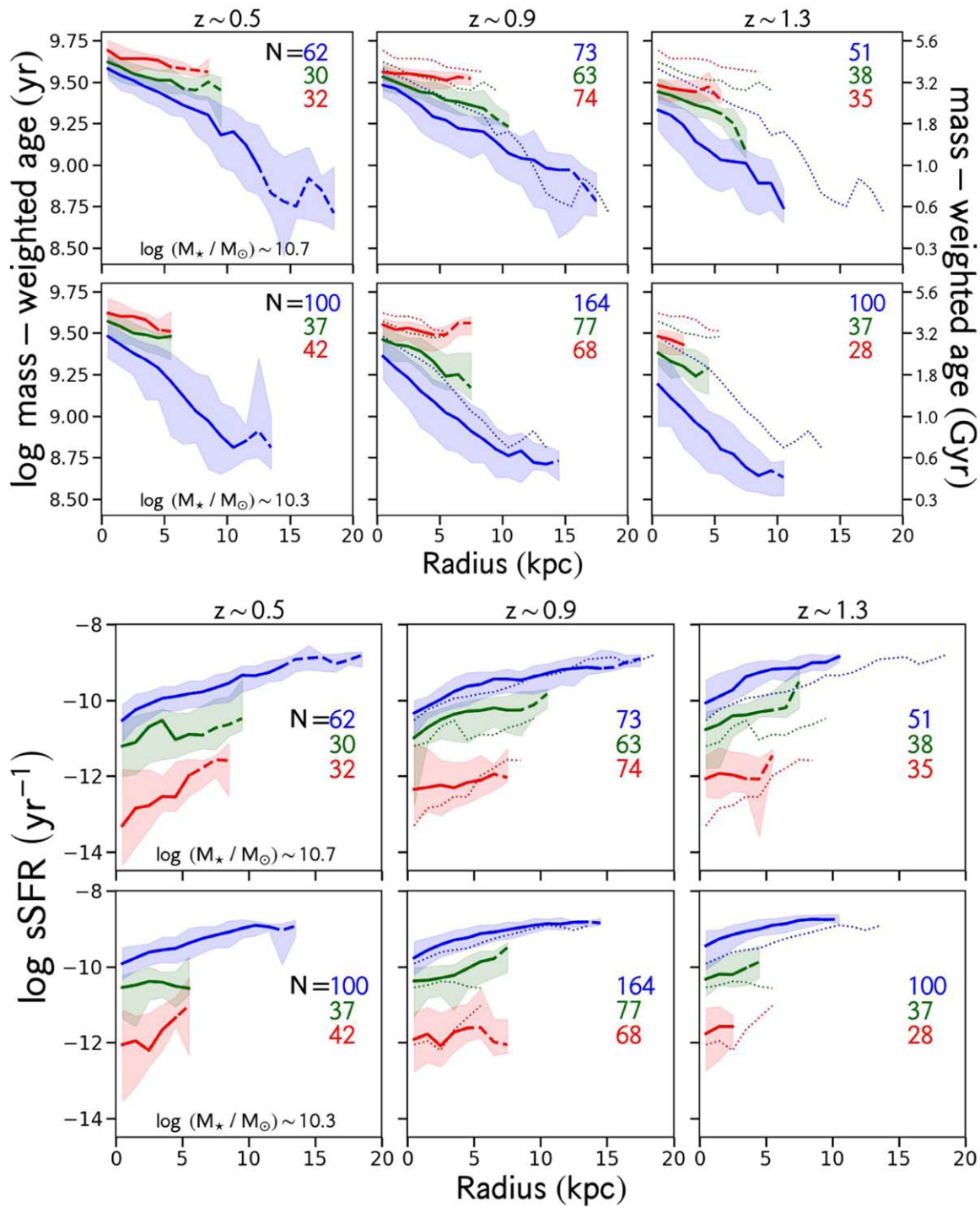
Figure 29. Median science profiles of mass-weighted age (top) and sSFR (bottom) under the fifth set of assumptions for all mass and redshift bins are shown. In each panel, the meanings of the lines, shadings, and colors are the same as those in the top two rows in Figure 13.
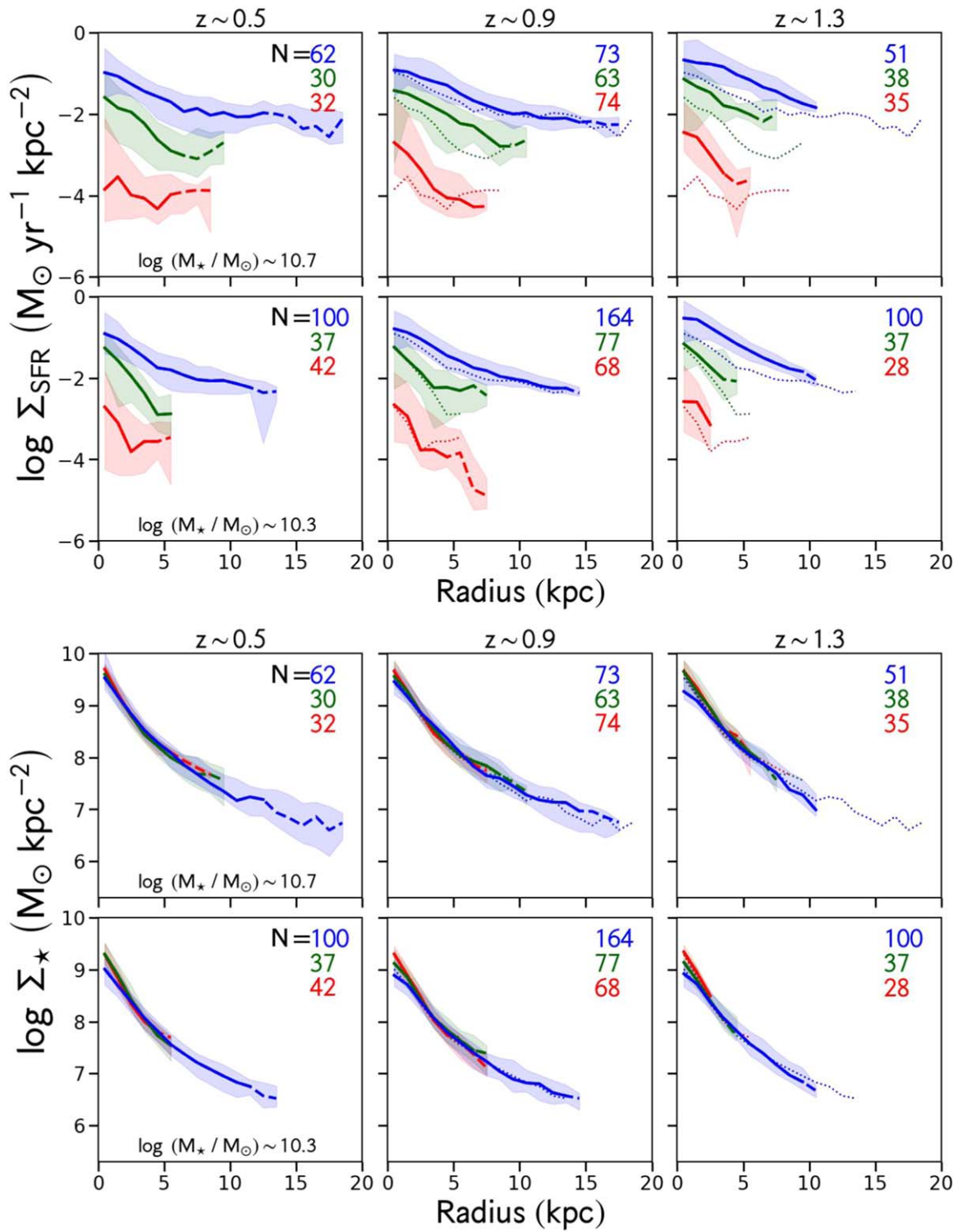
Figure 30. Median science profiles of SFR surface density (top) and stellar mass surface density (bottom) under the fifth set of assumptions for all mass and redshift bins are shown. In each panel, the meanings of the lines, shadings, and colors are the same as those in the top two rows in Figure 13.
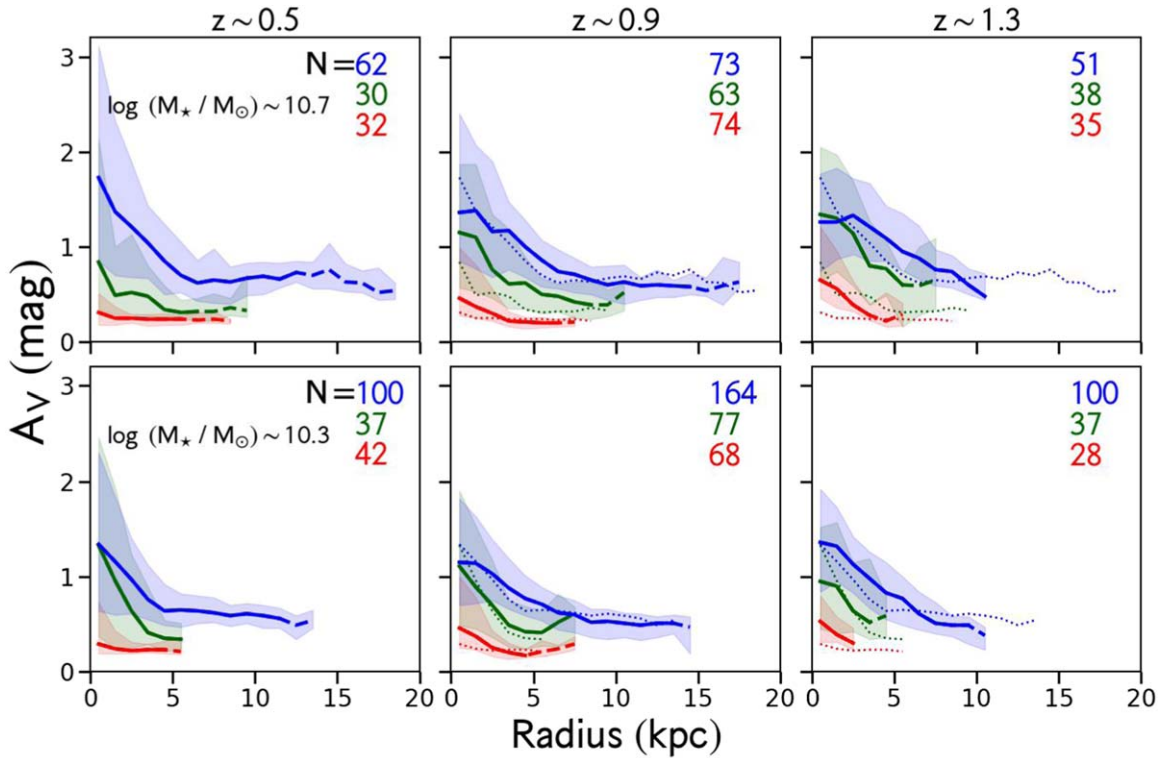
Figure 31. Median science profiles of A_V under the fifth set of assumptions for all mass and redshift bins are shown. In each panel, the meanings of the lines, shadings, and colors are the same as those in the top two rows in Figure 13.

Appendix D
Galaxy Evolution under the Fifth Set of Assumptions Considering Evolution in Mass with Redshift

In this Appendix, the evolution of sSFR profiles with redshift is examined in bins in mass that also evolve with redshift. The results presented here are quantitatively similar to those in the case of fixed mass bins (see Section 11).

To connect galaxies throughout time, we adopt the abundance-matching results by B. P. Moster et al. (2013). Instead of two bins of fixed mass, we assume two bins in halo mass at $z = 0$ ($M_{h,z=0}$): $12.3 < \log(M_{h,z=0}/M_\odot) < 12.8$ and $12.8 < \log(M_{h,z=0}/M_\odot) < 13.6$. These are shown in Figure 32. We compute curves of the expected evolution in stellar mass with redshift by integrating the fitting functions for the star formation and mass accretion histories of galaxies provided by B. P. Moster et al. (2013). These also take into account mass loss due to stellar evolution. In the lower bin in halo mass, galaxies increase in stellar mass by ~0.5 dex from $z = 1.5$ to $z = 0.4$, whereas this growth is about 0.2 dex over the same redshift interval in the higher halo mass bin.

We find similar quantitative results when considering evolution in mass with redshift to what we found in fixed bins in mass (see Section 11). Median sSFR profiles of galaxies in both bins in halo mass and three redshift bins are shown in the top two rows in Figure 33. Linear fits to the median profiles are shown in the bottom two rows in Figure 33. Star-forming, green
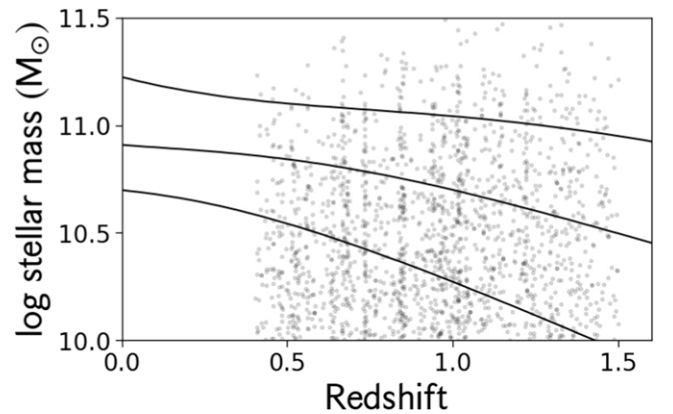

Figure 32. sSFR profiles in mass bins that evolve with redshift are shown here; the bins are indicated by solid lines. They are computed by choosing halo masses at $z = 0$ and integrating the fitting functions provided by B. P. Moster et al. (2013). Individual galaxies are shown as light-gray dots.

valley, and quiescent galaxies in all mass and redshift bins have slopes that are consistent with the slopes measured at fixed mass (Figure 13) to within 2σ, with only one exception. Star-forming galaxies in the lower halo mass bin at $z \sim 0.5$ have a median profile with a slightly steeper slope than that of star-forming galaxies of stellar mass $\log(M_\star/M_\odot) \sim 10.3$ at the same redshifts (0.112 ± 0.007 versus 0.086 ± 0.004 dex kpc^{-1}).
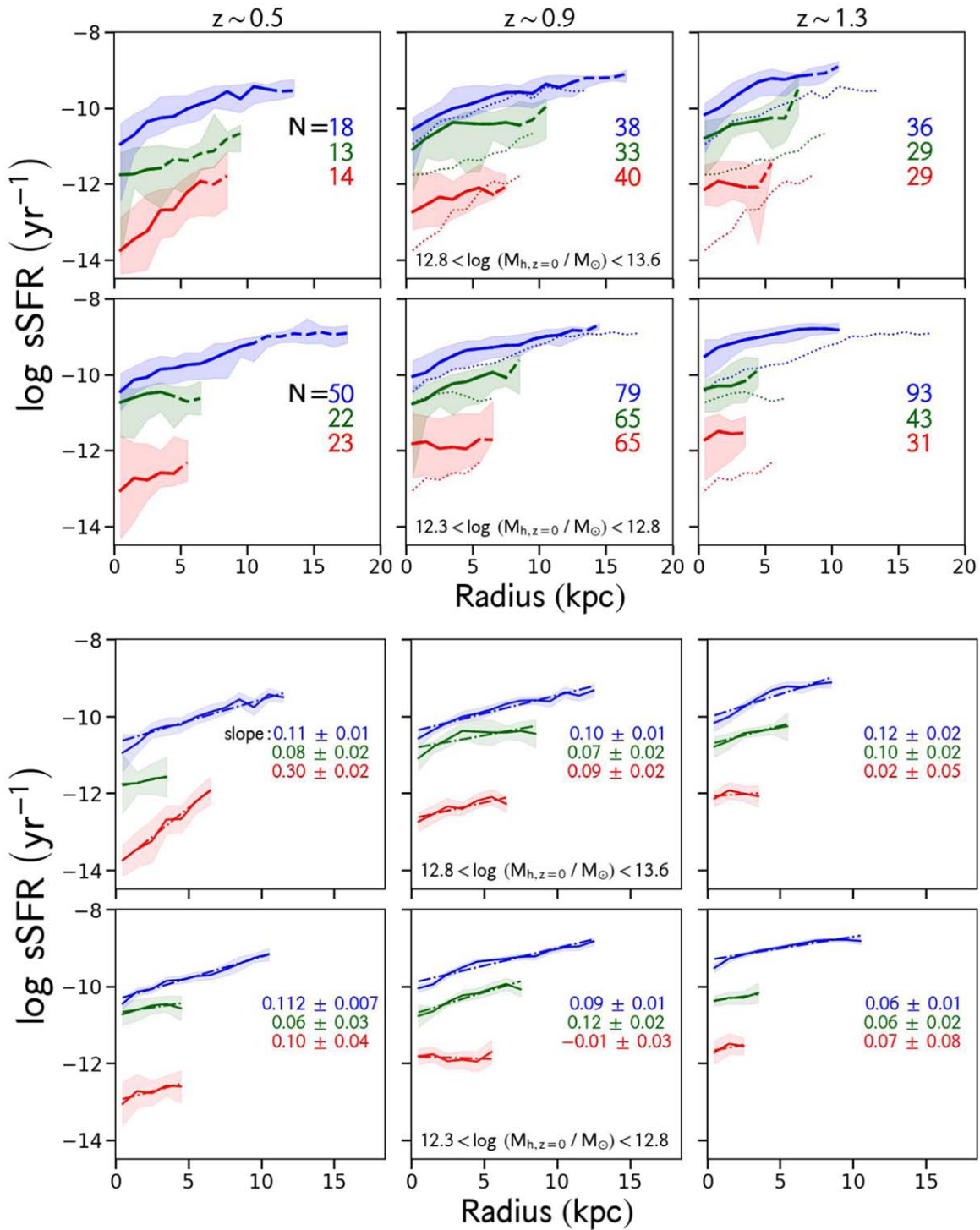
Figure 33. Median science profiles of sSFR under the fifth set of assumptions are measured in mass bins that evolve with redshift and depicted are here. Results from this analysis are similar to those done at fixed mass (see Section 11). In the top two rows, median profiles are shown, and in the bottom two rows, fits to the median profiles are shown as dashed–dotted lines. In each panel, the meanings of the lines, shadings, and colors are the same as those in the top two rows in Figure 13.

ORCID iDs

Alexander de la Vega ⬤ https://orcid.org/0000-0002-6219-5558
Susan A. Kassin ⬤ https://orcid.org/0000-0002-3838-8093
Camilla Pacifici ⬤ https://orcid.org/0000-0003-4196-0617
Stéphane Charlot ⬤ https://orcid.org/0000-0003-3458-2275
Emma Curtis-Lake ⬤ https://orcid.org/0000-0002-9551-0534
Jacopo Chevallard ⬤ https://orcid.org/0000-0002-7636-0534
Timothy M. Heckman ⬤ https://orcid.org/0000-0001-6670-6370

Anton M. Koekemoer ⬤ https://orcid.org/0000-0002-6610-2048
Weichen Wang ⬤ https://orcid.org/0000-0002-9593-8274

References

Abdurro'uf, & Akiyama, M. 2018, MNRAS, 479, 5083
Appleby, S., Davé, R., Kraljic, K., Anglés-Alcázar, D., & Narayanan, D. 2020, MNRAS, 494, 6053

Astropy Collaboration, Price-Whelan, A. M., Lim, P. L., et al. 2022, ApJ, 935, 167

Astropy Collaboration, Price-Whelan, A. M., Sipőcz, B. M., et al. 2018, AJ, 156, 123

Astropy Collaboration, Robitaille, T. P., Tollerud, E. J., et al. 2013, A&A, 558, A33

Avila-Reese, V., González-Samaniego, A., Colìn, P., Ibarra-Medel, H., & Rodrìguez-Puebla, A. 2018, ApJ, 854, 152

Barišić, I., Pacifici, C., van der Wel, A., et al. 2020, ApJ, 903, 146

Barrera-Ballesteros, J. K., Sánchez, S. F., Garcìa-Lorenzo, B., et al. 2015, A&A, 579, A45

Barro, G., Pérez-González, P. G., Cava, A., et al. 2019, ApJS, 243, 22

Battisti, A. J., Calzetti, D., & Chary, R. R. 2017, ApJ, 851, 90

Bekki, K., & Shioya, Y. 1998, ApJ, 497, 108

Bekki, K., & Shioya, Y. 1999, ApJ, 513, 108

Belfiore, F., Maiolino, R., Bundy, K., et al. 2018, MNRAS, 477, 3014

Bell, E. F., & de Jong, R. S. 2001, ApJ, 550, 212

Bell, E. F., Phleps, S., Somerville, R. S., et al. 2006, ApJ, 652, 270

Bell, E. F., Wolf, C., Meisenheimer, K., et al. 2004, ApJ, 608, 752

Bertin, E., & Arnouts, S. 1996, A&AS, 117, 393

Boada, S., Tilvi, V., Papovich, C., et al. 2015, ApJ, 803, 104

Bradley, L., Sipocz, B., Robitaille, T., et al. 2020, astropy/photutils: v1.0.0, Zenodo, doi:10.5281/zenodo.4044744

Bradley, L., Sipocz, B., Robitaille, T., et al. 2022, astropy/photutils: v1.5.0, Zenodo, doi:10.5281/zenodo.6825092

Brammer, G. B., Whitaker, K. E., van Dokkum, P. G., et al. 2011, ApJ, 739, 24

Bravo, M., Robotham, A. S. G., Lagos, C. d. P., et al. 2023, MNRAS, 522, 4481

Bressan, A., Marigo, P., Girardi, L., et al. 2012, MNRAS, 427, 127

Brinchmann, J., Charlot, S., Kauffmann, G., et al. 2013, MNRAS, 432, 2112

Brinchmann, J., Charlot, S., White, S. D. M., et al. 2004, MNRAS, 351, 1151

Bruzual, G., & Charlot, S. 2003, MNRAS, 344, 1000

Bryant, J. J., Owers, M. S., Robotham, A. S. G., et al. 2015, MNRAS, 447, 2857

Buat, V., Heinis, S., Boquien, M., et al. 2014, A&A, 561, A39

Buck, T. 2020, MNRAS, 491, 5435

Bundy, K., Bershady, M. A., Law, D. R., et al. 2015, ApJ, 798, 7

Byun, Y. I., Freeman, K. C., & Kylafis, N. D. 1994, ApJ, 432, 114

Caffau, E., Ludwig, H. G., Steffen, M., Freytag, B., & Bonifacio, P. 2011, SoPh, 268, 255

Calzetti, D., Kinney, A. L., & Storchi-Bergmann, T. 1994, ApJ, 429, 582

Carnall, A. C., Leja, J., Johnson, B. D., et al. 2019, ApJ, 873, 44

Carnall, A. C., McLure, R. J., Dunlop, J. S., & Davé, R. 2018, MNRAS, 480, 4379

Casertano, S., de Mello, D., Dickinson, M., et al. 2000, AJ, 120, 2747

Chabrier, G. 2003, PASP, 115, 763

Charlot, S., & Fall, S. M. 2000, ApJ, 539, 718

Chevallard, J., & Charlot, S. 2016, MNRAS, 462, 1415

Chevallard, J., Charlot, S., Wandelt, B., & Wild, V. 2013, MNRAS, 432, 2061

Cibinel, A., Le Floc'h, E., Perret, V., et al. 2015, ApJ, 805, 181

Costantin, L., Pérez-González, P. G., Méndez-Abreu, J., et al. 2022, ApJ, 929, 121

Cramer, W. J., Kenney, J. D. P., Sun, M., et al. 2019, ApJ, 870, 63

Curtis-Lake, E., Chevallard, J., Charlot, S., & Sandles, L. 2021, MNRAS, 503, 4855

Curtis-Lake, E., McLure, R. J., Dunlop, J. S., et al. 2013, MNRAS, 429, 302

da Cunha, E., Charlot, S., & Elbaz, D. 2008, MNRAS, 388, 1595

Daddi, E., Dickinson, M., Morrison, G., et al. 2007, ApJ, 670, 156

Dahlen, T., Mobasher, B., Faber, S. M., et al. 2013, ApJ, 775, 93

Dantas, M. L. L., Coelho, P. R. T., de Souza, R. S., & Gonçalves, T. S. 2020, MNRAS, 492, 2996

Davidzon, I., Ilbert, O., Laigle, C., et al. 2017, A&A, 605, A70

Domìnguez, A., Siana, B., Henry, A. L., et al. 2013, ApJ, 763, 145

Elbaz, D., Daddi, E., Le Borgne, D., et al. 2007, A&A, 468, 33

Ellison, S. L., Sánchez, S. F., Ibarra-Medel, H., et al. 2018, MNRAS, 474, 2039

Emami, N., Siana, B., Weisz, D. R., et al. 2019, ApJ, 881, 71

Estrada-Carpenter, V., Papovich, C., Momcheva, I., et al. 2019, ApJ, 870, 133

Faber, S. 2011, The Cosmic Assembly Near-IR Deep Extragalactic Legacy Survey ("CANDELS"), MAST, doi:10.17909/T94S3X

Faber, S. M., Willmer, C. N. A., Wolf, C., et al. 2007, ApJ, 665, 265

Ferland, G. J., Porter, R. L., van Hoof, P. A. M., et al. 2013, RMxAA, 49, 137

Feroz, F., Hobson, M. P., & Bridges, M. 2009, MNRAS, 398, 1601

Fitzpatrick, E. L. 1999, PASP, 111, 63

Flores Velázquez, J. A., Gurvich, A. B., Faucher-Giguère, C.-A., et al. 2021, MNRAS, 501, 4812

Fossati, M., Mendel, J. T., Boselli, A., et al. 2018, A&A, 614, A57

Fumagalli, M., Labbé, I., Patel, S. G., et al. 2014, ApJ, 796, 35

Gallazzi, A., Bell, E. F., Zibetti, S., Brinchmann, J., & Kelson, D. D. 2014, ApJ, 788, 72

Gallazzi, A., Charlot, S., Brinchmann, J., White, S. D. M., & Tremonti, C. A. 2005, MNRAS, 362, 41

Garn, T., & Best, P. N. 2010, MNRAS, 409, 421

Ge, J., Mao, S., Lu, Y., et al. 2021, MNRAS, 507, 2488

Genzel, R., Förster Schreiber, N. M., Lang, P., et al. 2014, ApJ, 785, 75

Giavalisco, M., Ferguson, H. C., Koekemoer, A. M., et al. 2004, ApJL, 600, L93

Giovanelli, R., Haynes, M. P., Salzer, J. J., et al. 1994, AJ, 107, 2036

Grand, R. J. J., & Kawata, D. 2016, AN, 337, 957

Grand, R. J. J., Kawata, D., & Cropper, M. 2015, MNRAS, 447, 4018

Greener, M. J., Aragón-Salamanca, A., Merrifield, M. R., et al. 2020, MNRAS, 495, 2305

Grogin, N. A., Kocevski, D. D., Faber, S. M., et al. 2011, ApJS, 197, 35

Guo, Y., Ferguson, H. C., Giavalisco, M., et al. 2013, ApJS, 207, 24

Guo, Y., Koo, D. C., Lu, Y., et al. 2016a, ApJ, 822, 103

Guo, Y., Rafelski, M., Bell, E. F., et al. 2018, ApJ, 853, 108

Guo, Y., Rafelski, M., Faber, S. M., et al. 2016b, ApJ, 833, 37

Gutkin, J., Charlot, S., & Bruzual, G. 2016, MNRAS, 462, 1757

Hahn, C., Tinker, J. L., & Wetzel, A. 2017, ApJ, 841, 6

Han, Y., Fan, L., Zheng, X. Z., Bai, J.-M., & Han, Z. 2023, ApJS, 269, 39

Han, Y., & Han, Z. 2012, ApJ, 749, 123

Han, Y., & Han, Z. 2014, ApJS, 215, 2

Han, Y., & Han, Z. 2019, ApJS, 240, 3

Harris, C. R., Millman, K. J., van der Walt, S. J., et al. 2020, Natur, 585, 357

Harvey, T., Conselice, C., Adams, N. J., et al. 2025, ApJ, 978, 89

Hathi, N. P., Ferreras, I., Pasquali, A., et al. 2009, ApJ, 690, 1866

Hemmati, S., Miller, S. H., Mobasher, B., et al. 2014, ApJ, 797, 108

Hemmati, S., Mobasher, B., Nayyeri, H., et al. 2020, ApJL, 896, L17

Henry, A., Scarlata, C., Domìnguez, A., et al. 2013, ApJL, 776, L27

Hirschmann, M., Naab, T., Ostriker, J. P., et al. 2015, MNRAS, 449, 528

Hopkins, P. F., Cox, T. J., Younger, J. D., & Hernquist, L. 2009, ApJ, 691, 1168

Hunter, J. D. 2007, CSE, 9, 90

Iyer, K., & Gawiser, E. 2017, ApJ, 838, 127

Jonsson, P., Groves, B. A., & Cox, T. J. 2010, MNRAS, 403, 17

Karim, A., Schinnerer, E., Martìnez-Sansigre, A., et al. 2011, ApJ, 730, 61

Kashino, D., Silverman, J. D., Rodighiero, G., et al. 2013, ApJL, 777, L8

Kass, R. E., & Raftery, A. E. 1995, JASA, 90, 773

Kassin, S. A., Weiner, B. J., Faber, S. M., et al. 2012, ApJ, 758, 106

Kennicutt, R. C., Jr. 1998, ARA&A, 36, 189

Kennicutt, R. C., & Evans, N. J. 2012, ARA&A, 50, 531

Kodra, D., Andrews, B. H., Newman, J. A., et al. 2023, ApJ, 942, 36

Koekemoer, A. M., Faber, S. M., Ferguson, H. C., et al. 2011, ApJS, 197, 36

Kriek, M., & Conroy, C. 2013, ApJL, 775, L16

Kriek, M., Labbé, I., Conroy, C., et al. 2010, ApJL, 722, L64

Kuchinski, L. E., Terndrup, D. M., Gordon, K. D., & Witt, A. N. 1998, AJ, 115, 1438

Labbé, I., Franx, M., Rudnick, G., et al. 2003, AJ, 125, 1107

Lawler, A. J., & Acquaviva, V. 2021, MNRAS, 502, 3993

Le Cras, C., Maraston, C., Thomas, D., & York, D. G. 2016, MNRAS, 461, 766

Lee, N., Sanders, D. B., Casey, C. M., et al. 2015, ApJ, 801, 80

Leja, J., Johnson, B. D., Conroy, C., van Dokkum, P. G., & Byler, N. 2017, ApJ, 837, 170

Leja, J., Johnson, B. D., Conroy, C., et al. 2019, ApJ, 877, 140

Leja, J., Speagle, J. S., Johnson, B. D., et al. 2020, ApJ, 893, 111

Li, P., Lelli, F., McGaugh, S., & Schombert, J. 2018, A&A, 615, A3

Li, P., Lelli, F., McGaugh, S., Schombert, J., & Chae, K.-H. 2021, A&A, 646, L13

Lin, L., Hsieh, B.-C., Pan, H.-A., et al. 2019, ApJ, 872, 50

Liu, F. S., Jia, M., Yesuf, H. M., et al. 2018, ApJ, 860, 60

Lo Faro, B., Buat, V., Roehlly, Y., et al. 2017, MNRAS, 472, 1372

Lower, S., Narayanan, D., Leja, J., et al. 2020, ApJ, 904, 33

Lu, S., Daddi, E., Maraston, C., et al. 2024, arXiv:2403.07414

Luo, B., Brandt, W. N., Xue, Y. Q., et al. 2017, ApJS, 228, 2

Ly, C., Malkan, M. A., Kashikawa, N., et al. 2012, ApJL, 747, L16

Lynden-Bell, D., & Kalnajs, A. J. 1972, MNRAS, 157, 1

Madau, P., & Dickinson, M. 2014, ARA&A, 52, 415

Maiolino, R., & Mannucci, F. 2019, A&ARv, 27, 3

Maiolino, R., Nagao, T., Grazian, A., et al. 2008, A&A, 488, 463

Man, A., & Belli, S. 2018, NatAs, 2, 695

Man, A. W. S., Toft, S., Zirm, A. W., Wuyts, S., & van der Wel, A. 2012, ApJ, 744, 85

Man, A. W. S., Zirm, A. W., & Toft, S. 2016, ApJ, 830, 89

Maraston, C. 2005, MNRAS, 362, 799

Martig, M., Bournaud, F., Teyssier, R., & Dekel, A. 2009, ApJ, 707, 250

McDermid, R. M., Alatalo, K., Blitz, L., et al. 2015, MNRAS, 448, 3484

Medling, A. M., Cortese, L., Croom, S. M., et al. 2018, MNRAS, 475, 5194

Mihos, J. C., & Hernquist, L. 1996, ApJ, 464, 641

Minchev, I., Chiappini, C., & Martig, M. 2014, A&A, 572, A92

Momcheva, I. G., Brammer, G. B., van Dokkum, P. G., et al. 2016, ApJS, 225, 27

Momcheva, I. G., Lee, J. C., Ly, C., et al. 2013, AJ, 145, 47

Moreno, J., Torrey, P., Ellison, S. L., et al. 2015, MNRAS, 448, 1107

Morishita, T., Ichikawa, T., Noguchi, M., et al. 2015, ApJ, 805, 34

Morselli, L., Popesso, P., Cibinel, A., et al. 2019, A&A, 626, A61

Mosleh, M., Hosseinnejad, S., Hosseini-ShahiSavandi, S. Z., & Tacchella, S. 2020, ApJ, 905, 170

Mosleh, M., Tacchella, S., Renzini, A., et al. 2017, ApJ, 837, 2

Moster, B. P., Naab, T., & White, S. D. M. 2013, MNRAS, 428, 3121

Moustakas, J., Coil, A. L., Aird, J., et al. 2013, ApJ, 767, 50

Muzzin, A., Marchesini, D., Stefanon, M., et al. 2013, ApJ, 777, 18

Nagaraj, G., Forbes, J. C., Leja, J., Foreman-Mackey, D., & Hayward, C. C. 2022, ApJ, 932, 54

Nelson, D., Pillepich, A., Springel, V., et al. 2018, MNRAS, 475, 624

Nelson, D., Springel, V., Pillepich, A., et al. 2019, ComAC, 6, 2

Nelson, E. J., Tacchella, S., Diemer, B., et al. 2021, MNRAS, 508, 219

Nelson, E. J., van Dokkum, P. G., Förster Schreiber, N. M., et al. 2016, ApJ, 828, 27

Newville, M., Stensitzki, T., Allen, D. B., & Ingargiola, A. 2014, LMFIT: Non-linear Least-Square Minimization and Curve-Fitting for Python v0.8.0, Zenodo, doi:10.5281/zenodo.11813

Noeske, K. G., Weiner, B. J., Faber, S. M., et al. 2007, ApJL, 660, L43

Ogando, R. L. C., Maia, M. A. G., Chiappini, C., et al. 2005, ApJL, 632, L61

Oke, J. B., & Gunn, J. E. 1983, ApJ, 266, 713

Onodera, M., Carollo, C. M., Renzini, A., et al. 2015, ApJ, 808, 161

Pacifici, C., Charlot, S., Blaizot, J., & Brinchmann, J. 2012, MNRAS, 421, 2002

Pacifici, C., da Cunha, E., Charlot, S., et al. 2015, MNRAS, 447, 786

Pacifici, C., Kassin, S. A., Weiner, B. J., et al. 2016, ApJ, 832, 79

Peletier, R. F., Valentijn, E. A., Moorwood, A. F. M., et al. 1995, A&A, 300, L1

Peng, C. Y., Ho, L. C., Impey, C. D., & Rix, H.-W. 2010, AJ, 139, 2097

Peng, Y.-j., Lilly, S. J., KovaÄ, K., et al. 2010, ApJ, 721, 193

Pérez, F., & Granger, B. E. 2007, CSE, 9, 21

Peterken, T., Merrifield, M., Aragón-Salamanca, A., et al. 2020, MNRAS, 495, 3387

Pforr, J., Maraston, C., & Tonini, C. 2012, MNRAS, 422, 3285

Pierini, D., Gordon, K. D., Witt, A. N., & Madsen, G. J. 2004, ApJ, 617, 1022

Pillepich, A., Nelson, D., Hernquist, L., et al. 2018, MNRAS, 475, 648

Planck Collaboration, Ade, P. A. R., Aghanim, N., et al. 2016, A&A, 594, A13

Price, S. H., Kriek, M., Brammer, G. B., et al. 2014, ApJ, 788, 86

Puglisi, A., Rodighiero, G., Franceschini, A., et al. 2016, A&A, 586, A83

Qin, J., Zheng, X. Z., Fang, M., et al. 2022, MNRAS, 511, 765

Ramraj, R., Gilbank, D. G., Blyth, S.-L., et al. 2017, MNRAS, 466, 3143

Riello, M., & Patat, F. 2005, MNRAS, 362, 671

Robaina, A. R., Bell, E. F., van der Wel, A., et al. 2010, ApJ, 719, 844

Rodighiero, G., Cimatti, A., Gruppioni, C., et al. 2010, A&A, 518, L25

Rodrìguez Montero, F., Davé, R., Wild, V., Anglés-Alcázar, D., & Narayanan, D. 2019, MNRAS, 490, 2139

Roškar, R., Debattista, V. P., Quinn, T. R., Stinson, G. S., & Wadsley, J. 2008, ApJL, 684, L79

Salim, S., Boquien, M., & Lee, J. C. 2018, ApJ, 859, 11

Salim, S., & Narayanan, D. 2020, ARA&A, 58, 529

Salmon, B., Papovich, C., Long, J., et al. 2016, ApJ, 827, 20

Salvador-Rusiñol, N., Vazdekis, A., La Barbera, F., et al. 2020, NatAs, 4, 252

Sánchez, S. F., Avila-Reese, V., Hernandez-Toledo, H., et al. 2018, RMxAA, 54, 217

Santini, P., Ferguson, H. C., Fontana, A., et al. 2015, ApJ, 801, 97

Schlafly, E. F., & Finkbeiner, D. P. 2011, ApJ, 737, 103

Schlegel, D. J., Finkbeiner, D. P., & Davis, M. 1998, ApJ, 500, 525

Schönrich, R., & Binney, J. 2009, MNRAS, 396, 203

Schreiber, C., Pannella, M., Elbaz, D., et al. 2015, A&A, 575, A74

Sellwood, J. A., & Binney, J. J. 2002, MNRAS, 336, 785

Shanks, T., Ansarinejad, B., Bielby, R. M., et al. 2021, MNRAS, 505, 1509

Shapley, A. E., Sanders, R. L., Reddy, N. A., Topping, M. W., & Brammer, G. B. 2023, ApJ, 954, 157

Shapley, A. E., Sanders, R. L., Salim, S., et al. 2022, ApJ, 926, 145

Silva, L., Granato, G. L., Bressan, A., & Danese, L. 1998, ApJ, 509, 103

Simons, R. C., Kassin, S. A., Weiner, B. J., et al. 2017, ApJ, 843, 46

Skelton, R. E., Whitaker, K. E., Momcheva, I. G., et al. 2014, ApJS, 214, 24

Snyder, G. F., Cox, T. J., Hayward, C. C., Hernquist, L., & Jonsson, P. 2011, ApJ, 741, 77

Sorba, R., & Sawicki, M. 2018, MNRAS, 476, 1532

Speagle, J. S., Steinhardt, C. L., Capak, P. L., & Silverman, J. D. 2014, ApJS, 214, 15

Steffen, J. L., Fu, H., Comerford, J. M., et al. 2021, ApJ, 909, 120

Suess, K. A., Kriek, M., Price, S. H., & Barro, G. 2019, ApJ, 877, 103

Tacchella, S., Carollo, C. M., Förster Schreiber, N. M., et al. 2018, ApJ, 859, 56

Tacchella, S., Dekel, A., Carollo, C. M., et al. 2016, MNRAS, 458, 242

Taylor, E. N., Hopkins, A. M., Baldry, I. K., et al. 2011, MNRAS, 418, 1587

Thorp, M. D., Ellison, S. L., Simard, L., Sánchez, S. F., & Antonio, B. 2019, MNRAS, 482, L55

Tomczak, A. R., Quadri, R. F., Tran, K. V. H., et al. 2016, ApJ, 817, 118

Tortora, C., Napolitano, N. R., Cardone, V. F., et al. 2010, MNRAS, 407, 144

Tress, M., Ferreras, I., Pérez-González, P. G., et al. 2019, MNRAS, 488, 2301

Tress, M., Mármol-Queraltó, E., Ferreras, I., et al. 2018, MNRAS, 475, 2363

Trussler, J., Maiolino, R., Maraston, C., et al. 2020, MNRAS, 491, 5406

Tuffs, R. J., Popescu, C. C., Völk, H. J., Kylafis, N. D., & Dopita, M. A. 2004, A&A, 419, 821

van der Wel, A., Bell, E. F., Häussler, B., et al. 2012, ApJS, 203, 24

van der Wel, A., Franx, M., van Dokkum, P. G., et al. 2014, ApJ, 788, 28

Vidal-Garcìa, A., Charlot, S., Bruzual, G., & Hubeny, I. 2017, MNRAS, 470, 3532

Villaume, A., Conroy, C., & Johnson, B. D. 2015, ApJ, 806, 82

Virtanen, P., Gommers, R., Oliphant, T. E., et al. 2020, NatMe, 17, 261

Walcher, C. J., Lamareille, F., Vergani, D., et al. 2008, A&A, 491, 713

Wang, B., Leja, J., Bezanson, R., et al. 2023, ApJL, 944, L58

Wang, W., Faber, S. M., Liu, F. S., et al. 2017, MNRAS, 469, 4063

Weibel, A., Wang, E., & Lilly, S. J. 2023, ApJ, 950, 102

Weigel, A. K., Schawinski, K., Caplar, N., et al. 2017, ApJ, 845, 145

Weinzirl, T., Jogee, S., Khochfar, S., Burkert, A., & Kormendy, J. 2009, ApJ, 696, 411

Whitaker, K. E., Franx, M., Leja, J., et al. 2014, ApJ, 795, 104

Whitaker, K. E., Labbé, I., van Dokkum, P. G., et al. 2011, ApJ, 735, 86

Whitaker, K. E., van Dokkum, P. G., Brammer, G., & Franx, M. 2012, ApJL, 754, L29

White, S. D. M. 1979, MNRAS, 189, 831

White, S. D. M. 1980, MNRAS, 191, 1P

Wild, V., Charlot, S., Brinchmann, J., et al. 2011, MNRAS, 417, 1760

Wu, P.-F., van der Wel, A., Gallazzi, A., et al. 2018, ApJ, 855, 85

Wuyts, S., Förster Schreiber, N. M., Genzel, R., et al. 2012, ApJ, 753, 114

Wuyts, S., Förster Schreiber, N. M., Lutz, D., et al. 2011, ApJ, 738, 106

Wuyts, S., Labbé, I., Förster Schreiber, N. M., et al. 2008, ApJ, 682, 985

Xue, Y. Q., Luo, B., Brandt, W. N., et al. 2016, ApJS, 224, 15

Zibetti, S., Gallazzi, A., Charlot, S., Pierini, D., & Pasquali, A. 2013, MNRAS, 428, 1479

Zolotov, A., Dekel, A., Mandelker, N., et al. 2015, MNRAS, 450, 2327